Local Nuclear Magnetic Resonance Spectroscopy with Giant Magnetoresistive Sensors

Pierre-André Guitard

NNT : 2015SACLS175

THESE DE DOCTORAT
DE
L'UNIVERSITE PARIS-SACLAY
PREPAREE A

UNIVERSITE PARIS-SUD
LABORATOIRE NANO-MAGNETISME ET OXYDE
SERVICE DE PHYSIQUE DE L'ETAT CONDENSE
SPEC – UMR 3680 CEA-CNRS

ECOLE DOCTORALE N° 564
PHYSIQUE EN ILE-DE-FRANCE

Spécialité de doctorat : PHYSIQUE

Par

M. Pierre-André GUITARD

Local Nuclear Magnetic Resonance Spectroscopy with Giant Magnetoresistive Sensors

Thèse présentée et soutenue à CEA Saclay, le 04 décembre 2015 :

Composition du Jury :

M. ALLOUL Henri	Directeur de recherche Université Paris Sud	Président
M. GREGG John	Professeur Magdalen College Oxford	Rapporteur
M. MONTAIGNE François	Professeur Université de Lorraine	Rapporteur
M^{me} POIRIER-QUINOT Marie	Enseignant-Chercheur Université Paris Sud	Examinatrice
M. JAQUINOT Jacques-François	Conseiller scientifique CEA Saclay	Examinateur
M. FERMON Claude	Directeur de recherche CEA Saclay	Directeur de thèse

Remerciements

Tout d'abord je tiens à remercier Monsieur François Daviaud, responsable du Service de Physique de l'Etat Condensé du Commissariat à l'Energie Atomique et aux Energies Alternatives de Saclay, de m'avoir accueilli et de m'avoir permis d'effectuer cette thèse au sein d'un environnement chaleureux et dynamique.

Je tiens ensuite à remercier les membres du jury Marie Poirier-Quinot, John Gregg, François Montaigne, Henri Alloul et Jacques-François Jaquinot pour avoir évalué cette thèse et également grâce à leurs remarques de m'avoir permis d'affiner la compréhension de ce manuscrit.

Je souhaite remercier tout particulièrement mon directeur de thèse Claude Fermon de m'avoir proposé ce sujet novateur qui permet de combiner la physique inhérent à la spintronique et la physique propre à la Résonnance Magnétique Nucléaire. Je lui suis également reconnaissant pour le temps qu'il m'a consacré, sa franchise et l'autonomie qu'il m'a laissé. J'ai appris énormément à ses cotés et je lui adresse donc toute ma gratitude.

Je voudrais également remercier l'équipe du Laboratoire de Nanomagnétisme et Oxyde qui à toujours été présent lors des différents problèmes rencontrés : Myriam Pannetier-Lecoeur et Claude Fermon pour leur encadrement; Gwenaëlle Lebras-Jasmin pour m'avoir soutenu lors des périodes difficiles; Aurélie Solignac Jean-Yves Chaulean Gregoire de Loubens d'avoir été présents pour apporter leurs avis et leurs corrections lors de la rédaction de thèse et également lors de la préparation de la soutenance.

Je remercie également Patrick Berthault du laboratoire Nanosciences et Innovation pour les Matériaux, la Biomédecine et l'Énergie pour m'avoir permis d'effectuer des mesures haut champs grâce à leur aimant 500MHz mais également d'avoir effectué des simulations de spectre de l'éthanol en régime de couplage fort.

Un grand merci à mes collègues et amis du laboratoire qui m'ont accompagné tout au long de cette thèse : Gérald Le Goff et Grégory Cannies les techniciens du groupe

qui m'ont aidé pour la conception du boitier RMN et pour la remise en route de l'electro-aimant; Elodie Paul l'ingénieur capteur avec qui j'ai beaucoup échangé pour la réalisation des capteurs GMR; Reyna Ayde pour son aide qu'elle m'a apporté en fin de thèse; Amala Demonti ingénieur en éléctronique avec qui j'ai travaillé sur le spectromètre; Vincent Trauchessec, Laure Caruso et Camille Blouzon pour les diverses discussions formelles et informelles; et enfin Paolo Campiglio pour les réponses à toutes mes questions sur la spintronique.

J'adresse également un remerciement particulier à mes parents et frangins qui m'ont supporté et toujours motivé au cours de ces trois années de travail.

Enfin je remercie toutes les personnes qui ont participé de près ou de loin au bon déroulement de ce travail.
is années de travail.

Enfin je remercie toutes les personnes qui ont participé de près ou de loin au bon déroulement de ce travail.

Résumé

Je vais vous présenter le travail que j'ai effectué au cours de ces trois années de thèse au Service de Physique de l'Etat Condensé du CEA Saclay, dans le groupe du Laboratoire de Nanomagnétisme et Oxyde sous la direction de Claude Fermon. Mon travail à porté sur la Spectroscopie Locale par Résonance Magnétique Nucléaire à l'aide capteur à MagnétoRésistance Géante.

La Résonance Magnétique Nucléaire (RMN) est un outil puissant car il permet de faire de la spectroscopie et donc d'avoir accès à la présence de molécules au sein d'un échantillon mais également d'avoir accès à la structure tridimensionnel des molécules. Ainsi la RMN utilisée dans de très nombreux domaines tels que la chimie, la biologie, la pharmaceutique, pour connaitre la pureté d'un médicament et également son efficacité, en industrie agroalimentaire et en médecine, car c'est une méthode non invasive et cela permet de faire des images de zones difficiles d'accès comme le cerveau par exemple.

Cependant, de nos jours, on va vers une réduction de taille des échantillons et du système de mesure. En effet, on veut être capable de mesurer de petits échantillons car il y a des difficultés à produire certains échantillons en quantité importante. C'est typiquement le cas pour les brins d'ADN synthétique. Mais actuellement, on est dans l'incapacité de mesurer des échantillons avec des volumes inférieurs au nanolitre. D'autre part, on veut être capable de faire une mesure locale, pour pouvoir étudier localement une réaction chimique mais également mesurer la concentration locale d'un produit. De nos jours, on est dans l'incapacité de mesurer localement une espèce chimique.

- Principe de la Résonance Magnétique Nucléaire

Un noyau est observable en RMN seulement s'il possède un spin nucléaire non nul. Il existe plusieurs types de RMN basé sur différents noyaux suivant le type d'information que l'on souhaite obtenir, tel que le carbone et l'azote pour l'étude de composé organique, le fluor, qui est un biomarqueur et qui est très utile pour l'IRM et le sodium. En ce qui me concerne, j'ai travaillé sur le proton d'hydrogène car c'est le plus utilisé et que l'hydrogène est présent en grande quantité dans de nombreuses molécules.

En absence de champ magnétique, lorsque l'on considère un échantillon, il existe un certain désordre dans l'orientation des spins. On peut dire qu'en moyenne il n'y a pas d'aimantation. En revanche, lorsque l'on applique un champ magnétique B0 à l'échantillon, les spins vont s'orienté parallèlement ou anti parallèlement à la direction du champ magnétique B0 suivant une distribution de Boltzmann. Il se créé donc une aimantation moyenne que l'on note : $M_0 = \frac{N\gamma^2\hbar^2 B_0}{4kT}$, Avec N : le nombre de proton; γ : le facteur gyromagnétique ; h : la constante de Planck; k : la constante de Boltzmann; T : la température; B_0 : le champ magnétique extérieur. Cependant, mesurer cet

aimantation de quelques pT comparé aux quelques T du champ magnétique B0 est quelque chose d'assez compliqué, c'est pourquoi une impulsion radiofréquence B1 est appliquée pour basculer l'aimantation hors équilibre. Les spins vont dont précesser à une certaine fréquence : la fréquence de Larmor que l'on note : $\omega=\gamma B_0$. On remarquera que cette fréquence est proportionnelle à B_0 via le facteur gyromagnétique γ. Une fois que l'impulsion radiofréquence est coupée, les spins vont retourner vers leur état d'équilibre toujours avec le mouvement de précession à la fréquence de Larmor avec un temps caractéristique T_1 qui est le temps de retour vers le niveau de plus basse énergie des spins excités. On mesure la composante transverse de l'aimantation en fonction du temps. Ainsi on peut mesure une courbe qui est une exponentielle décroissante en fonction du temps avec un temps caractéristique T_2 qui est le temps de cohérence transversale. Pour avoir accès la fréquence de résonance, la transformé de Fourier de cette courbe est tracée.

Ce qui est intéressant en RMN c'est que l'on peut faire de la spectroscopie. Comme on à vu précédemment, la fréquence de résonance dépend du champ magnétique B_0 que l'on applique. Or lorsque l'on considère une molécule, il y a un écrantage de B0 au voisinage de chaque proton. C'est ce que l'on appel le déplacement chimique que l'on note : $\delta = \frac{(\nu-\nu_{ref})}{\nu_0}.10^6$ et que l'on exprime en ppm. En effet, on exprime en ppm car cela permet de comparer des différents graphiques qui auraient été obtenu avec des champs B_0 différents. Sur le spectre de l'éthanol, échantillon que j'ai utilisé au court de ma thèse, le déplacement chimique est représenté par l'ensemble les trois gros déplacements de fréquence. Cependant, on peut remarquer que pour chaque déplacement, on à un ensemble de pics de résonance. C'est ce que l'on appelle le couplage scalaire qui est une interaction entre les liaisons et qui permet d'avoir une information sur la structure de la molécule et qui donne lieu à une séparation des raies. Pour obtenir ce couplage scalaire, on considère les atomes d'hydrogène voisin de l'atome considéré. Ainsi pour les H du CH3 il y a deux H voisins, les H du CH2, et donc pour les H du CH3 on aura l'apparition deux fréquences de résonnance en plus d'où le triplet. En ce qui concerne les H du CH2, les atomes voisins sont les trois H du CH3 et le H de la fonction alcool. Mais on ne considère pas le H du OH car l'oxygène agissant comme un tampon, on ne voit pas l'apparition d'une fréquence de résonance en plus. Ainsi on ne considère uniquement que les H du CH3 d'où l'apparition de trois fréquences de résonance en plus : quadruplet. Et donc une seule fréquence pour la fonction alcool.

Classiquement, la détection se fait à l'aide de bobines accordées. Une bobine accordée est une bobine qui est accordée à une seule fréquence de résonance : la fréquence de Larmor. Pour cela, comme on a un circuit RC, l'accord en fréquence se fait à l'aide d'une capacité d'accord suivant la formule suivante : $\nu = \frac{1}{2\pi\sqrt{LC}}$. De plus, comme le travail est effectué à relativement haute fréquence, l'accord en impédance est également nécessaire. En effet, sans cet accord en impédance, tout le signal détecté serait perdu tout au long de la chaine d'acquisition. L'accord en impédance avec une capacité d'accord, placé en

série, du précédent circuit RC.

Mais on va vers une réduction de tailles d'échantillons et des systèmes de mesures. Ainsi pour différents applications, différents systèmes de mesures sont développé. Pour des applications micro fluidique, il y a l'apparition de micro bobines de type solénoïdes. Grâce à cela, Sillerud and al. J. mag. res.(2006), on été capable d'obtenir un SNR/nL/acq de 4.1.10-1 à 1.04T sur des biomolécules fonctionnalisées avec des microbilles magnétiques. Pour des applications in-vivo, Renaud and al. Sens. Act. A-Phys (2002), on été capable d'obtenir un SNR/nL/acq de 1.4.10-4 à 2T sur de l'eau deionisé. Le problème avec ce type de capteur, c'est que ce sont des capteurs de flux. Et donc, intrinsèquement, lorsque la taille de l'échantillon est réduite, le signal qui peut être détecté est également réduit. De plus avec les microbobines, il y a une diminution du facteur de qualité : $Q = \frac{L\omega}{R}$. Sur des microbobines, la section de fil utilisée est réduite ce qui va vers une augmentation de la résistance de la bobine et la diminution de la longueur de fil et du nombre de tour fait qu'il y a une diminution de l'inductance de la bobine. Ces trois éléments combiné font que globalement il y une diminution du facteur de qualité. D'autre part, il existe une taille limite pour les microbobines, dû à une barrière technologique, qui donne lieu à une diminution du facteur de remplissage et donc à un signal détectable plus faible.

C'est pourquoi au cours de ma thèse, j'ai décidé d'utiliser des capteurs de type magnétorésistif qui présentent l'avantage d'avoir une sensibilité indépendante de la taille du capteur. D'autre part ce sont des capteurs large bande et donc on peut avoir la possibilité de travailler à plusieurs fréquences de résonnance. Ce sont des capteurs de champs magnétiques qui font que la taille de l'échantillon n'influe par le signal que l'on peut détecter. Et enfin, ce sont des capteurs compatibles avec des mesures in-vivo.

- Principe de la Magnétorésistance Géante

Lorsque l'on considère un matériau ferromagnétique, les bandes d'énergie des électrons de conduction présentent un décalage. Ce décalage fait que les électrons de spin up et down sont diffusés en parallèle avec des résistivités différentes. Ainsi lorsque l'on considère deux couches ferromagnétiques séparées par une couche non magnétique, dans le cas où les aimantations des couches magnétiques sont dans l'état parallèles, la résistance est faible résistance. A contrario, lorsque les couches magnétiques sont dans l'état antiparallèle, la résistance est importante.

Pour les applications capteurs, il faut travailler avec une alternance de couche de type vanne de spin. La vanne de spin standard est composée d'une couche dite dure, dont l'aimantation ne varie pas avec le champ magnétique extérieur, un espaceur : la couche non magnétique et la couche libre, la couche qui varie avec le champ

magnétique extérieur. La couche dure est donc composée d'une couche antiferromagnétique (PtMn) et d'une tricouche que l'on appelle une couche antiferromagnétique synthétique (CoFe/Ru/CoFe) et qui va permettre de bien stabiliser la couche dure. Ensuite il y a la présence de l'espaceur (Cu) et la couche libre composé d'une bicouche CoFe/NiFe. En effet une bicouche est utilisé car la couche de CoFe possède une forte polarisation et va permettre d'avoir une grande magnétorésistance géante et la couche de NiFe qui est un ferromagnétique doux qui permet de suivre relativement bien le champ magnétique extérieur.

D'autre part, pour des applications capteurs, il faut que l'aimantation de la couche libre bouge de façon cohérente et réversible avec le champ magnétique extérieur. Pour cela la forme de yoke est préférée. En effet, cette forme permet d'avoir une configuration monodomaine dans la partie active du capteur. Néanmoins avec ce type de capteur, on est uniquement capable de travailler sur de très petit volume. Pour pouvoir travailler sur de plus gros volumes, la forme de méandre est choisie.

Pour caractériser le capteur, ce dernier est placé dans une bobine d'Helmholtz qui va avoir un champ variable. Le capteur est alimenté à l'aire d'un Keitley, et le signal est amplifié et filtré avec un stanford, et détecté avec une carte d'acquisition. Avec cette mesure, il est capable de déduire la magnétorésistance qui est noté : $MR = \frac{\triangle R}{R_0} x100$ et la sensibilité : $S_{GMR} = \frac{1}{R_0}\frac{dR}{dH}$. Il est à noter ici que la sensibilité se trouve dans le plan de la GMR. Or pour l'application RMN, le capteur va être placé de telle sorte que le champ magnétique B_0 soit perpendiculaire au capteur. Or pour que le capteur reste dans un état sensible, il faut que la composante transverse de B_0 soit inférieure à 0,05° pour 1T. Mais il est également important de connaitre l'intensité du champ magnétique. En effet, initialement dans le plan, l'aimantation du capteur va avoir tendance à sortir du plan au fur et à mesure que le champ magnétique augmente.

Une autre chose importante à caractériser est le bruit du capteur. Pour cela, le capteur est placé dans une chambre blindé et alimenté avec des piles. Le signal est ensuite amplifié avec un amplificateur bas bruit de type INA 103, puis encore filtré et amplifié avec un stanford lui-même fonctionnant sur batterie et l'acquisition est faite avec une carte d'acquisition et la FFT est faite avec l'ordinateur. Ainsi sur les graphique de bruit, on eut discerné deux type de bruit : le bruit thermique, que l'on note : $4k_bTR$ avec T la température et R la résistance du capteur et le bruit en 1/f, que l'on note :$\frac{\gamma I^2 R^2}{N_c f}$.

Une fois que les bases de la RMN et de la GMR sont bien établies, des simulations ont été faites pour les deux applications microfluidique et in-vivo. Pour la simulation microfluidique, on a considéré un microcapillaire de diamètre 10µm placé devant le capteur. Pour la configuration in-vivo, on a considéré le capteur placé dans le liquide.

Ainsi pour 300mT, un signal de 12pT est attendu pour la configuration microfluidique et un signal de 150pT pour la configuration in-vivo. Pour connaitre le volume sur lequel le signal est détecté, une autre simulation a été effectuée. Pour cela, le signal détecté au niveau du capteur est simulé pour différentes sphères de rayon r variant de 0 à 100µm simulant du liquide. Donc dans une première approximation, on peut considérer que 80% du signal provient d'un volume de 20µm autour du capteur. Avec ces simulations, une figure de mérite a pu être tracée. Cette figure de mérite est en fait une compétition entre le signal RMN qui est détecté, qui augmente avec l'augmentation du champ magnétique B_0 et l'aimantation qui sort du plan de la couche libre qui a tendance à diminuer la sensibilité du capteur avec l'augmentation du champ B_0. La figure de mérite présente donc un maximum aux alentours de 0,4 – 0,5 T.

- Système de mesure

Le champ magnétique B_0 provient de deux systèmes que j'ai étudiés au cours de la thèse. Le premier système se compose d'un aimant permanent. L'aimant permanent avait l'avantage d'être portable, peu coûteux et d'avoir un champ stable au cours du temps. Les inconvénients étaient que le champ était relativement inhomogène, malgré l'ajout de bobines de compensations, et que l'on avait uniquement une seule valeur de champ B_0. Or on a vu précédemment que le signal détecté était proportionnel au champ magnétique et donc pour avoir un signal important il faut que le champ magnétique soit important. Or avec cet aimant permanent, le champ magnétique est de 86,2T. C'est la raison pour laquelle, par la suite, j'ai travaillé avec un électroaimant. L'électroaimant présente l'avantage d'avoir un champ magnétique homogène et un champ variable jusqu'à 2T. Les inconvénients sont que l'aimant est volumineux et donc il n'est pas transportable, le champ est également instable au cours du temps.

L'impulsion radiofréquence est générée à l'aide d'un générateur d'impulsion RF et envoyé sur la bobine. Pour notre application, la bobine est donc utilisée en émission et réception.

La détection se fait de deux façons : avec le capteur GMR et la bobine accordée, qui va permettre de comparer les signaux mesurés et également servir de référence. En effet, le champ magnétique créé par l'électroaimant ne permet pas de moyenner les signaux détectés et d'avoir une résolution correcte pour pouvoir faire de la spectroscopie. C'est la raison pour laquelle la bobine va servir de référence. Pour chaque acquisition, la transformée de Fourier (TF) du signal détecté par la bobine, est tracé. Un traitement des données permet de détecter le pic de la TF, correspondant au signal. Ce pic est ensuite décalé à 0 et est moyenné avec les données précédentes. Ainsi avec ce type de traitement, la variation de champ magnétique n'est plus critique. Cela permet d'avoir une résolution de 14Hz à 13MHz ce qui représente moins de 1ppm de résolution et qui nous permet de faire de la spectroscopie.

Le signal passe ensuite par le spectromètre. En effet, le passage à travers le spectromètre permet d'amplifier le signal et également de ramener la fréquence de travail de quelques MHz à kHz, ce qui fait que l'acquisition de données est plus aisée. Le signal est détecté en parallèle pour la bobine accordée ainsi que pour le capteur GMR. Le spectromètre est un spectromètre classique pour la bobine accordée. Pour le capteur GMR, un amplificateur et un filtre spécifique au capteur est placé en amont du spectromètre. L'acquisition se fait ensuite avec une carte d'acquisition.

- Résultats

Le premier résultat que l'on a obtenu, sur de l'eau a montré que le signal était à la fois détecté par la bobine accordé et par le capteur, en une acquisition. Pour valider ce résultat, la même expérience a été faite dans le cas où la GMR, placé dans le champ magnétique, se trouve dans un état non sensible. Il en ressort que le signal apparait une nouvelle fois sur la voix du capteur GMR alors que l'on ne devrait rien mesurer. Il y avait donc la présence d'un couplage directe entre la bobine accordé et le capteur GMR. Pour éliminer ce couplage, la sensibilité du capteur GMR a été orientée de telle sorte qu'elle soit perpendiculaire à l'axe de la bobine. D'autre part, le capteur GMR est modulé en fréquence.

Le principe de la modulation est que l'on alimente le capteur GMR non plus en DC, mais en AC. Ainsi la tension de sortie de la GMR peut se noter $V_GMR = [R_0 + \frac{dR}{dH} I$ avec R_0 la résistance du capteur, H le champ magnétique qui s'exprime : $H = H_0\ cos(\omega_H t + \varphi_H)$ que l'on cherche à mesurer et I le courant. Le courant est donc en AC et peut se noter ainsi : $I = I_0 cos(\omega_0 t + \varphi_0)$. La tension de la GMR peut donc se noter : $V_{GMR} = R_0 I_0 cos(\omega_0 t + \varphi_0) + (R_1 I_0 H_0)/2[cos[(\omega_H - \omega_0)t + \varphi_H - \varphi_0)] + cos[(\omega_H + \omega_0)t + \varphi_H + \varphi_0)]]$. Si l'on regarde la TF de sortie pour la voix capteur, il apparait, comme le montre la figure ci-dessous, que le couplage direct apparait bien au niveau de la fréquence de résonnance, puis de part et d'autre de ce couplage, décaler de la fréquence à laquelle le capteur est alimenté, le signal réellement détecté par le capteur GMR.

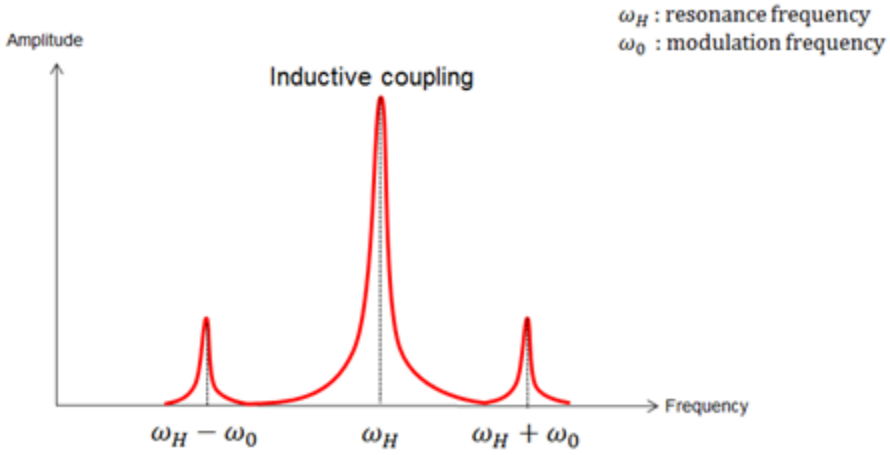

Ainsi voici le résultat que l'on a obtenu sur de l'eau à 0,3T avec le capteur GMR :

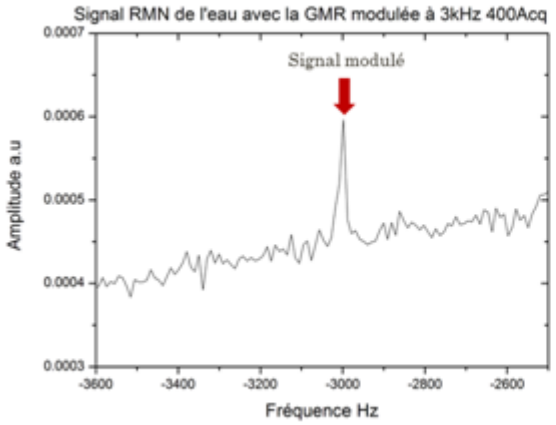

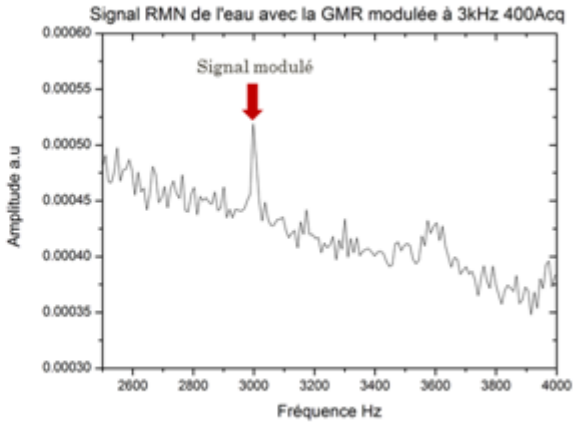

Le signal est bien détecté de part et d'autre du couplage inductif, replacé en 0Hz avec la bobine accordée. On voit sur ces graphiques que l'acquisition est faite avec une modulation de 3kHz et 400 acquisitions. Ainsi, le signal de l'eau apparait bien a +3kHz et -3kHz.

La même mesure a été faite sur de l'éthanol, qui présente 3 raies et qui permet de valider l'approche de la spectroscopie. Voici les graphiques de l'on a obtenu pour de l'éthanol à 3,8kHz et 3000 acquisitions :

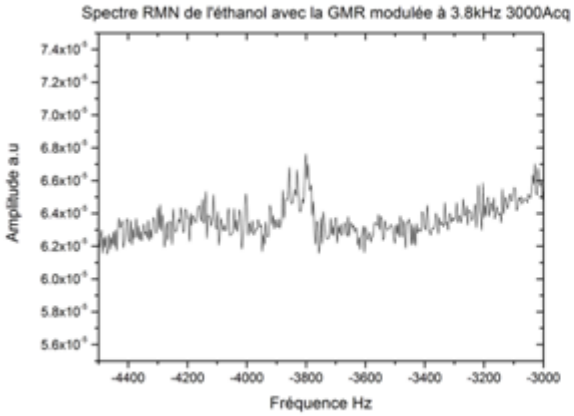

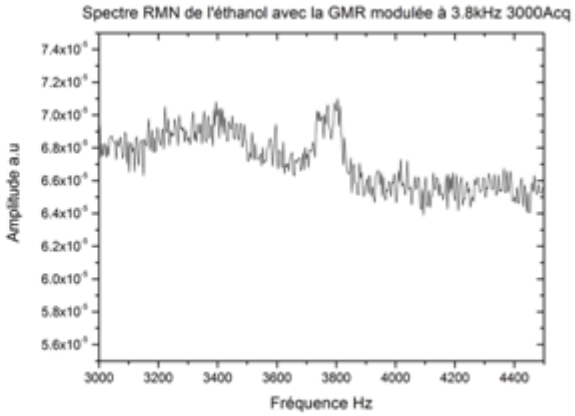

Le signal est bien placé à +3,8kHz et - 3,8kHz. Cependant, lorsque ce signaux sont comparés avec une approche théorique voici ce qui est obtenu :

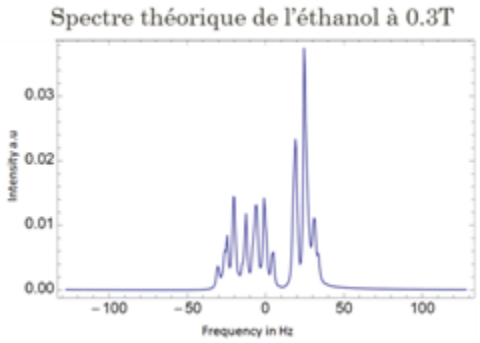

Cette courbe théorique a été obtenue grâce à l'aide P. Berthault (NIMBE). Ce qui est remarquable sur la courbe théorique c'est qu'il n'y a pas uniquement la présence de 3 pics un ensemble de pic plus conséquent. Cela est dû au fait que dans le cas de 0,3T, on est dans un régime de couplage fort. C'est-à-dire que le déplacement chimique est du même ordre de grandeur que le couplage J. Mais lorsque l'on considère notre système, avec sa résolution de 1ppm et que l'on superpose ce que l'on obtient théoriquement avec ce l'on mesure voici ce que l'on obtient :

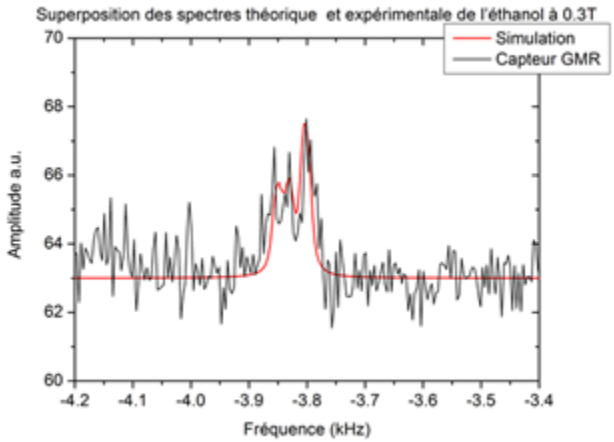

On peut remarquer que les deux courbes se superposent et donc ce que l'on mesure est correct.

Pour s'éloigner de cette zone de couplage fort, les mêmes mesures ont été faites à 0,8T. Mais à ce champs magnétique, même dans l'état ou la GMR est sensible, rien n'est détecté. C'est pourquoi il a été étudié le comportement du capteur GMR en fréquence. Et pour le capteur sur Silicium, il a été remarqué que plus la fréquence était augmentée, plus le capteur subissait un phénomène de couplage direct et cela même lorsque ce dernier n'est pas alimenté. Ce problème n'a pas eu le temps d'être étudié en profondeur et la décision de travailler avec des capteurs sur d'autres substrats a été

choisie tel que l'alumine et le verre. Avant de partir dans les expériences, une étude en fréquence, similaire à celle faite sur le capteur sur silicium, a été effectuée. Cette étude a permis de montrer que ce phénomène de couplage à haute fréquence n'est pas présent. Une autre étude permettant d'étudier la sensibilité des capteurs en fonction du champs magnétique B0 perpendiculaire au capteur a permis de montrer que les capteurs sont utilisable jusque à 1T.

Ensuite les capteurs sont été montés pour pouvoir détecté les signaux. Pour le capteur sur l'alumine voici ce qui a été détecté sur de l'éthanol a 0,3T avec 5000 acquisitions et une fréquence de modulation de 3,4kHz :

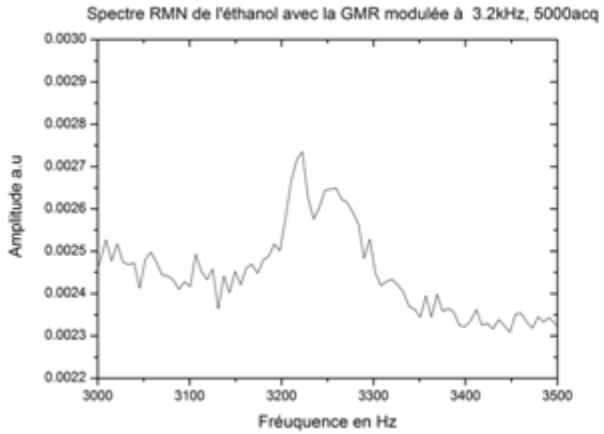

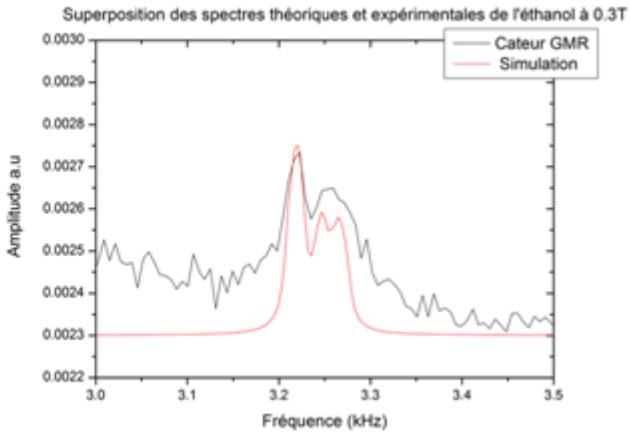

De même que précédemment, les signaux sont en accord avec la théorie.

Ensuite pour ne plus être dans le régime de couplage fort, il a été décidé de faire une mesure à 0,6T sur de l'eau. Voici ce qui a été obtenu avec un capteur sur verre avec une modulation de 5kHz et 1500 acquisitions.

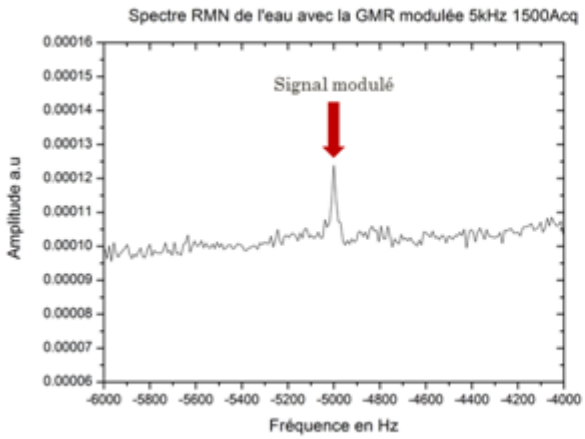

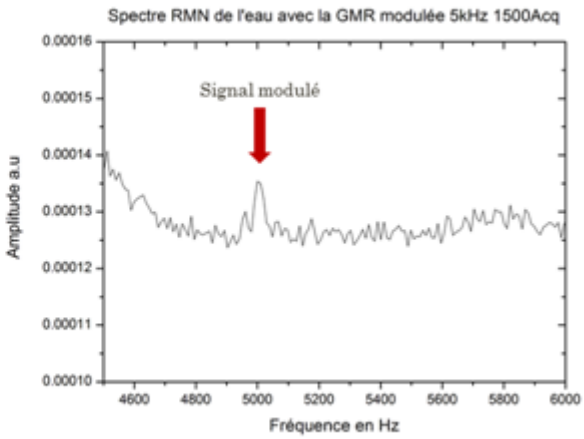

Cela permet de conclure qu'un signal est bien détecté au bon endroit et que l'on peut faire de la spectroscopie avec ce champ magnétique B0. Faute de temps aucune mesure n'a pu être obtenu sur de l'éthanol.

Afin d'appliquer notre système à un système réel, il a été décidé de faire une mesure sur du glutamate, neuro inhibiteur présent dans le cerveau. Pour cela, une concentration comparable à ce qui est présent dans le cerveau a été choisie soit 6mM.L-1 et voici ce qui a été obtenu à 0,3 T :

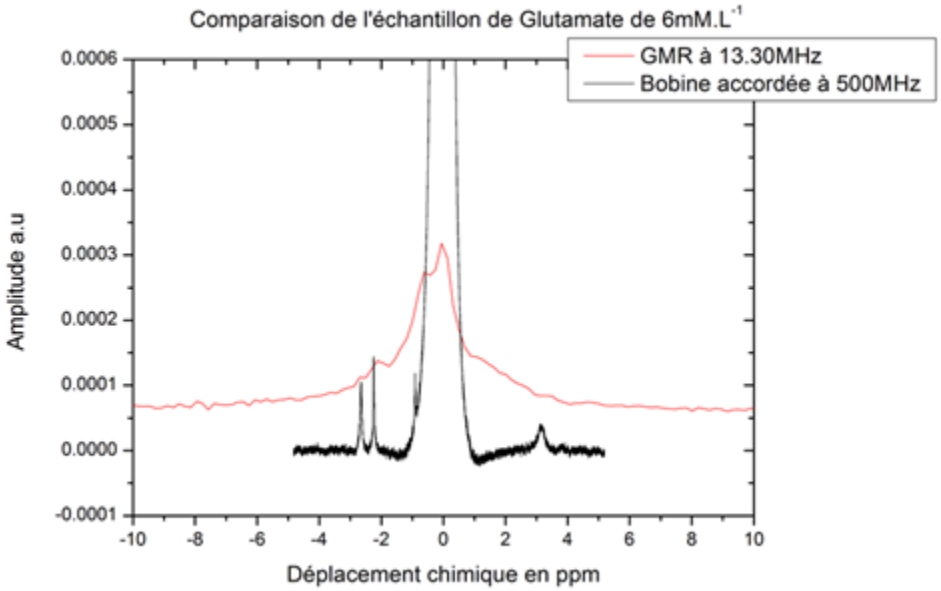

Ce graphique permet de constater que le signal typique du glutamate est bien détecté par le capteur GMR. Cependant, lorsque l'on compare avec le pic central, on peut

constater que cela ne correspond pas. En effet avec la bobine accordée à 500Mhz, le signal du glutamate est très petit comparé au signal central, alors que sur le capteur GMR ce n'est pas le cas. L'hypothèse est que pour le capteur GMR, quelques molécules de glutamate se sont collées sur le capteur, ce qui fait que l'on détecte du signal. Cela implique deux choses. D'une part cela est intéressant car avec le capteur GMR, il est possible de détecter très localement la présence d'une molécule. D'autre part cela a un inconvénient majeur qui est que l'on ne mesure pas la vraie concentration de produit.

En conclusion je peux dire que ce travail de thèse a permis la mesure d'un signal RMN avec un capteur magnétorésistif de type GMR. Ainsi j'ai pu obtenir une mesure très locale du signal, de l'ordre de $20\mu m^3$. D'autre par le SNR que l'on obtient est beaucoup important que ce qui pourrait être obtenu, sur des volumes comparable, avec des bobines accordées classiques.

Cependant, le travail effectué est loin d'être fini. Pour aller plus loin, certaines optimisations sont encore nécessaires.

Il convient d'abord de travailler sur la stabilité du champ magnétique. La façon dont le champ magnétique est stabilisé comporte ses limites et ne nous permet pas actuellement d'obtenir des résolutions inférieures à la ppm. Pour travailler avec un champ stable il faudrait travailler avec un aimant de type supraconducteur.

D'autre part, pour éviter le couplage direct entre la bobine accordée et le capteur GMR, il faudrait penser à avoir une bobine de type lock qui serait placé à l'extérieur du capteur, ou alors travailler avec la bobine qui serait utilisée uniquement pour l'excitation.

Un autre paramètre important à faire évoluer est le positionnement du capteur dans le champ. Actuellement ce positionnement manuel est plus ou moins grossier. Par la suite, pour que les mesures soient reproductibles facilement et rapidement, un positionnement plus précis doit être mis en place.

Enfin la dernière chose qui serait modifiable, serait de travailler avec des capteurs magnéto résistif mais cette fois de type TMR. Travailler avec ces types de capteurs permettrait de gagner un facteur 10 en sensibilité et ainsi un facteur 100 en temps d'acquisition. L'utilisation de ces capteurs au cours de cette thèse n'a pas pu être possible car le laboratoire ne possédait pas les outils nécessaires à leurs fabrications.

Contents

Introduction

Nuclear Magnetic Resonance (NMR) is one of the most leading technologies for the structural determination of biomacromolecules at atomic scale resolution and biomedical imaging. Although this technique was first highlighted in the late thirties by *Rabi and al.*[50], it has continued to evolve until nowadays. This is mainly due to the fact that it finds some applications such as in analytical chemistry, biochemistry and also in civilian's applications such as medical imaging.

The performance of a NMR experiment is given by the signal-to-noise ratio. Usually, to have a signal of high intensity, a high and homogeneous static magnetic fields and a large sample volume is needed. Moreover in conventional cases, signals are detected by tuned coils. Their major drawback is that when the sample size is decreased, the filling factor is also decreased. But sometimes due to the difficulties of obtaining some fluids, experiments on small volumes are only possible. This is particularly true with the cerebrospinal fluid which is obtained by lumbar puncture and that can also be risky for the patient. In general, manipulating at the micron scale allows a faster work in a cleaner and safer environment.

Another drawback with tuned coils is that they are tuned at a specific frequency. And if another working frequency needs to be reached, another full set-up has to be developed. Even if some untuned detection methods, such as atomic optical magnetometers, single nitrogen vacancy in diamonds and superconducting quantum interference device, already exist, they do not permit a low fabrication cost, since their environment requires cryogenics, optics, and fragile objects. In addition to that, their working volume is often fixed and can be too small for some applications. This is the case for instance with NV-center sensors, whose volume of detection is at the nanoscale.

The ideal sensor would then be sensitive enough for small signals detection, untuned, with a wide frequency range, cheap, biocompatible, robust and that can be sized for the different applications. One type of sensor matches all these criteria: Giant MagnetoResisistive (GMR) sensors. Since its discovery in the late eighties by *Fert and al. [2]* on one side and *Grundberg and al. [9]* on other side, these sensors experienced many applications, the most popular one being reading heads in computer hard disks. Indeed these sensors present the advantage to be very sensitive. Their detection is only limited at low frequency by the $\frac{1}{f}$ noise. Moreover they are untuned and they can work in DC or in AC until some GHz. In addition, they have a short recovery time which enables

the measurement of broad signals. They are cheap for two simple reasons. The first one is that they are composed of metallic layers and their working conditions only requires a current flow; the second reason is that their fabrication requires deposition techniques and lithographic methods which are nowadays well known and well mastered. They are biocompatible and robust in as much as they can be deposited on different substrates such as silicon [51], glass [52], alumina [53] or polyamide [54]. By robust we also mean that they can work with strong RF pulses, which is quite convenient for NMR applications. Finally they can also be of any chosen size insofar as sensors are received as wafer and then processed according to the different needed specifications.

The aim of this thesis is to detect NMR signals with spin electronic based sensors in order to perform spectroscopy on small fluid volumes with relatively low magnetic field compared to actual NMR spectroscopy set-up.

In order to have an idea of the required sensitivity of the sensor to detect a signal, some simulations were performed. In a simple way, we thought that to detect the signal, we would put the sensor directly into the sample. Indeed, this permits to create a dissymmetry in the system and obtain a nonzero signal. This signal has been estimated.

The second step of the work consisted in the fabrication process of the sensors. The design was thought to match the specifications. As the sensor will be directly immersed into the sample a bar shape was designed. Sensors were then fabricated with classical microfabrication techniques: ionic etching, sputtering deposition and diamond saw cutting. Once fabricated, sensors were completely characterized to determine their magnetoresistance, sensitivity and noise.

As GMR sensors are not conventional sensors for NMR signals detection, the development of a set-up which can be placed into the magnet was performed. This part includes the shielding around the sensor, a three directional rotation system allowing the placement of the sensor into the magnetic field and the around electronics, with in particular the modulation and demodulation part, and allt the needed filters. To be able to compare with classical tuned coils, we decided to record in parallel the same signal with a tuned coil. For practical reasons the tuned coil was used for emission and reception.

Before proceeding to any measurement, we need to ensure that the sensor is still sensitive into the magnet. For that a calibrated coil permits to test and obtain the sensitivity of the sensor when this one is in presence of the magnetic field.

Measurements were then performed with both tuned coil and GMR sensor. Some results were obtained and compared to high field measurements, 11T compared with our 0.3T.

In this part it has been decided to work on classical samples such as water, to ensure that the set-up is functional, ethanol, to ensure that we are able to do spectroscopy and glutamate, with classical brain concentration, to demonstrate that our set-up is competitive with actual high field tuned coil measurements.

As it was working at 0.3T, to demonstrate that we can do it at another field and to have a better spectral resolution, some measurements were tried at 0.6T. For this part a modification of the homemade spectrometer and a change of the pulse generator had to be done. These measurements permit to realize that with silicon substrate sensors, above 15Mhz, signal directly passes through silicon annihilating the magnetoresistance effect. We then decided to come back at 0.3T and to test some other sensors deposited on different substrates such as glass and alumina. With sensors on alumina we managed to perform measurements on glutamate at 0.3T. And with sensors on glass we managed to perform measurements on water at 0.6T.

Chapter 1

Nuclear Magnetic Resonance

The aim of this first chapter is to give a brief introduction to Nuclear Magnetic Resonance (NMR). Once the main bases are established, I will focus on the various techniques used to achieve and to sense very small volumes of materials. Amongst these techniques, tuned coils, microcoils, atomic optical magnetometers, nitrogen vacancy-centers in diamonds and finally micro-MRI will be described. I will discuss about the advantages and the disadvantages of each technique.

1.1 Principle of Nuclear Magnetic Resonance

1.1.1 Spin definition

Nuclear Magnetic Resonance (NMR) is based on the magnetic properties of atom's nuclei which are composed of neutrons and protons. Some nuclei have an angular momentum and accordingly a magnetic moment. This phenomenon can be explained by classical physics saying that magnetic moment is linked to the rotation of the charge around its own axis, but also by quantum mechanics that states that the angular momentum is quantified and called nuclear spin I. We define the magnetic moment $\vec{\mu}$ such as:

$$\vec{\mu} = \hbar\gamma\vec{I} \tag{1.1}$$

where $\hbar$ is the reduced Planck constant, γ the gyromagnetic ratio of the particle and $\vec{I}$ the nuclear angular moment. Moreover, I_z is quantized and can take 2I+1 values. For protons and neutrons $I = \frac{1}{2}$. In absence of external interaction, all these spin

states are degenerated. But the application of an external magnetic field will break this degeneracy leading to spin states with different energies (see figure 1.1).

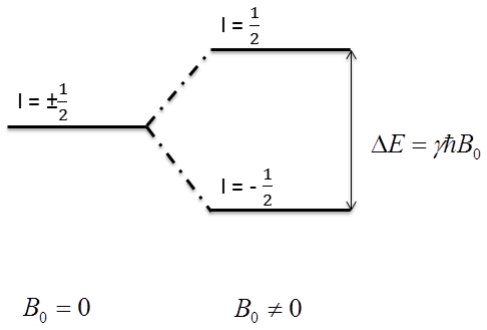

Figure 1.1: Energy splitting for a $\frac{1}{2}$ spin in a magnetic field.

Only atoms presenting a magnetic moment different from 0 are suitable for NMR detection. Thereby, we only consider:

- atoms with an even mass nuclei with an odd number of neutrons
- atoms with an odd mass nuclei

In table 1.1 are presented the characteristics of some of the atoms that can be detected by NMR.

Nuclei	Natural abundance (%)	Spin I	Gyromagnetic constantγ(MHz/T)
^{1}H	99.98	1/2	42.576
^{13}C	1.1	1/2	10.705
^{19}F	100	1/2	40.053
^{23}Na	100	3/2	11.268
^{31}P	100	1/2	17.235

Table 1.1: Gyromagnetic constant and natural abundance of some nuclei usually measured by NMR.

In presence of an external field B_0, the Zeeman interaction occurs between this external field and the nuclear moment $\vec{\mu}$. The energy of this interaction is:

$$E_m = -\vec{\mu}.\vec{B_0} = -I\hbar\gamma B_0 \tag{1.2}$$

The magnetic field splits the degenerated energy levels with a difference of energy proportional to $\vec{B_0}$. This effect is called the Zeeman effect. For a 1/2 spin, the two eigenstates are $-\frac{1}{2}\hbar\gamma B_0$ and $\frac{1}{2}\hbar\gamma B_0$. Figure 1.1 presents this behavior for nuclei with a 1/2 spin (like ^{1}H). Then, the difference of energy between the two states is $\triangle E = \gamma\hbar B_0$. Boltzmann equation describes the difference of population between the spin down and spin up states. Still for 1/2 spin, it can written:

$$\frac{N_\beta}{N_\alpha} = e^{-\frac{\Delta E}{k_b T}} \tag{1.3}$$

where N_α is the state of lower energy and N_β the state of upper energy, T the temperature and k_b Boltzmann constant.

A macroscopic sample contains a very large number of nuclei. When the sample is immersed into a field, magnetic moments align along this field. In the case of atoms that are interesting for NMR, and depending on their gyromagnetic ratio, the number of parallel spins is a little bit more important than the number of anti-parallel spins. This leads to a vectorial sum of all magnetic moments $\vec{\mu} \neq 0$ called nuclear magnetization: $\vec{M}$. Thanks to equations 1.2 and 1.3 the module of this nuclear magnetization can be deduce:

$$M_0 = N\frac{\gamma^2.\hbar^2 B_0}{4k_b T} \tag{1.4}$$

where N is the is the number of spins and T the temperature.

Finally, when a magnetic moment is placed into a magnetic field, it also experiences a torque:

$$\vec{\mathrm{S}} = \vec{\mu} \wedge \vec{B} \tag{1.5}$$

This torque comes from the fact that electrons are in orbit around the nucleus. And we remember that the magnetic moment is proportional to the angular momentum. The torque exerted then produces a change in the angular momentum which is perpendicular to that angular momentum, causing the magnetic moment to precess around the direction of the field rather than being aligned with it.
Using the theorem of the kinetic energy and as $\vec{\mu} = \gamma\vec{L}$, where $\vec{L}$ is the kinetic moment:

$$\frac{d\vec{\mu}}{dt} = \gamma\vec{\mu} \wedge \vec{B} \tag{1.6}$$

Considering a constant field B along the axis z :

$$\begin{cases} \frac{d\mu_x}{dt} = & \gamma B\mu_y \\ \frac{d\mu_y}{dt} = & -\gamma B\mu_x \\ \frac{d\mu_z}{dt} = & 0 \end{cases}$$

The solution of these equations is an oscillating transverse component and a constant longitudinal component. That means a precession of the moment around the field direction at the frequency:

$$\omega_0 = -\gamma B_0 \tag{1.7}$$

This frequency is called the Larmor frequency.

1.1.2 Excitation and Relaxation

To be easily detected, the magnetization precession should be perpendicular to the field $\vec{B_0}$. Thus we apply a radio-frequency pulse $\overrightarrow{B_1}$ perpendicular to the field.
The excitation becomes the superposition of a fixed magnetic field $\overrightarrow{B_0}$ and a rotating magnetic field $\overrightarrow{B_1}$ such that:

$$\overrightarrow{B_0} = \begin{bmatrix} 0 \\ 0 \\ B_0 \end{bmatrix} \text{ and } \overrightarrow{B_1} = \begin{bmatrix} B_1 cos(\omega t) \\ B_1 sin(\omega t) \\ 0 \end{bmatrix}$$

To see the influence of this RF field on the magnetization, we calculate the total magnetization thanks the equation 1.6. The total magnetization can be written as:

$$\frac{d\vec{M}}{dt} = \gamma \overrightarrow{M} \wedge (\overrightarrow{B_0} + \overrightarrow{B_1}(t)) \tag{1.8}$$

The resolution of this equation in not easy since the second member is time depending. A change in the coordinate system can be done to simplify the resolution of the equation. We choose to consider a geometric system in rotation around the z axis at the pulsation ω. In this system the magnetic field $\overrightarrow{B_1}$ is not moving. We choose the axes as X, Y, Z with the unitary vector $\overrightarrow{i'}, \overrightarrow{j'}, \overrightarrow{k'}$ which coincides with $\overrightarrow{i}$, $\overrightarrow{j}$, $\overrightarrow{k}$ at the time $t = 0$ of the establishment of the $\overrightarrow{B_1}$ field. This is illustrated on figure 1.2.

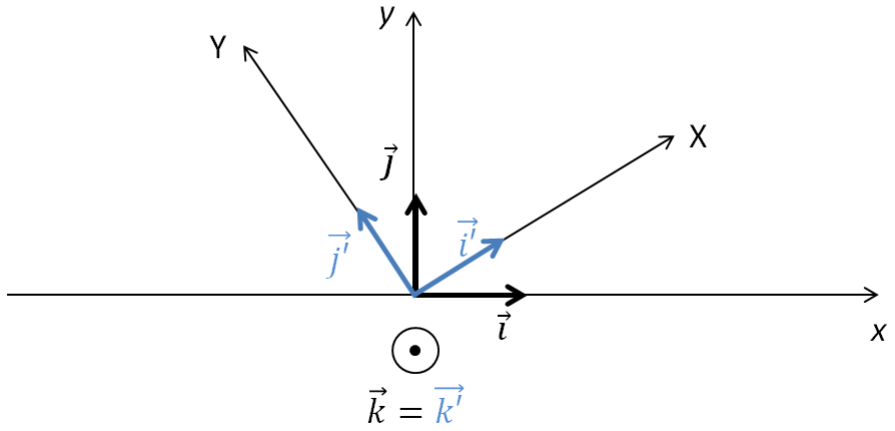

Figure 1.2: Laboratory system in black and rotating system in blue.

After some calculations [64], following equation can be written:

$$\frac{d\vec{M}}{dt} = \gamma\vec{M} \wedge \overrightarrow{B_{eff}} \tag{1.9}$$

The axis and the pulsation of the Larmor precession in the rotating system are given by the direction and the algebraic measurement of $\gamma\overrightarrow{B_{eff}} = (\omega_0 - \omega)\,\vec{k} + B_1\,\vec{u}$ where $\vec{u}$ is the unit vector which is fixed in the rotating system as presented on figure 1.3 and defined as: $\vec{u} = cos(\phi)\,\vec{i'} + sin(\phi)\,\vec{j'}$

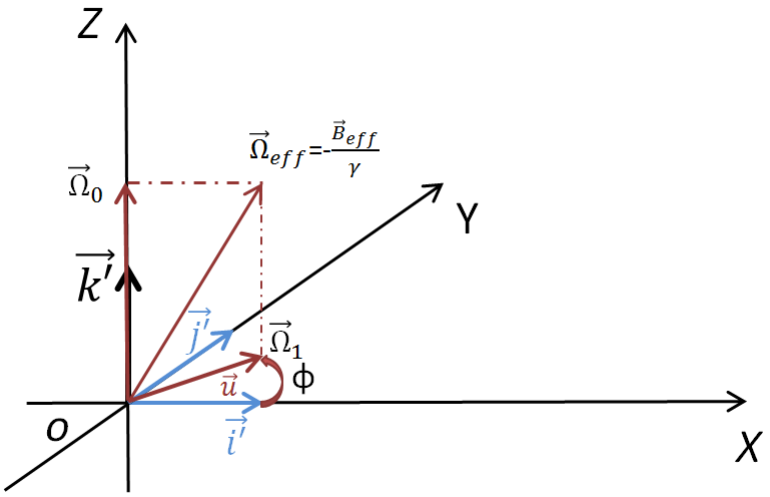

Figure 1.3: Effect of an RF pulse, in red, in the rotating system.

The RF pulse is then able to switch the magnetization out of its equilibrium. The maximum of signal is obtained when the magnetization is perpendicular to the direction of the $\vec{B_0}$ field, that means in xOy the plan.

After the pulse is turned off, and as the field $\vec{B_0}$ is still present, magnetic moments will come back to their equilibrium, parallel to the field, with a movement of precession with an angular speed : $\omega_0 = 2\pi\nu_0$.

This nuclear spins relaxation back to equilibrium following the application of a RF pulse is well described by Bloch set of equations [7]. If we consider a field along the z axis, we can measure different rates of relaxation $\frac{1}{T_1}$ and $\frac{1}{T_2}$which corresponds to, respectively, the longitudinal component and the transverse components 1.11. T_1 is called the spin-lattice relaxation time and T_2 the spin-spin relaxation time.

$$\frac{dM(t)}{dt} = M(t) \times \gamma B(t) - R\left[M(t) - M_0\right] \tag{1.10}$$

where R is the relaxation matrix. When we develop we find:

$$\begin{cases} \frac{dM_x(t)}{dt} = & \gamma\left[M_y(t)B_z(t) - M_z(t)B_y(t)\right] - \frac{M_x(t)}{T_2} \\ \frac{dM_y(t)}{dt} = & \gamma\left[M_z(t)B_x(t) - M_x(t)B_z(t)\right] - \frac{M_y(t)}{T_2} \\ \frac{dM_z(t)}{dt} = & \gamma\left[M_x(t)B_y(t) - M_y(t)B_x(t)\right] - \frac{M_z(t)-M_0}{T_1} \end{cases} \tag{1.11}$$

The measurement of the relaxation magnetization is possible only if T_2 can be defined. For spectroscopy applications linewidth which represents the spread frequency of the spins, does not able the definition of a T_2.

In conclusion, NMR experiment consists in three steps which are polarization, excitation and relaxation. This process is well underscored by figure 1.4.

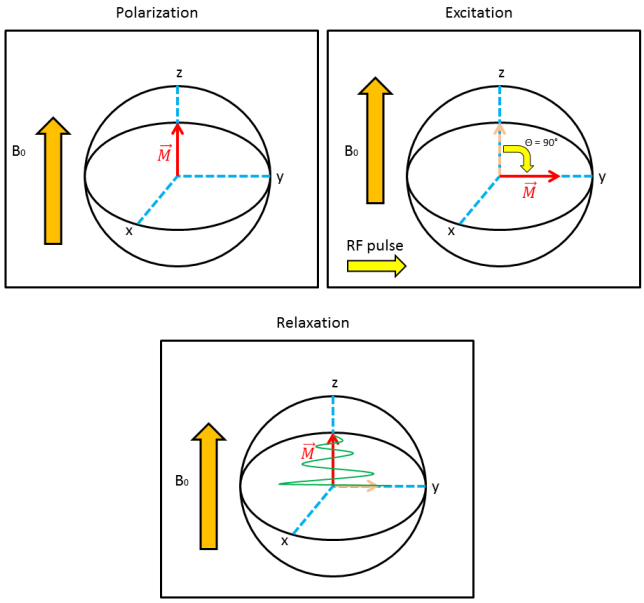

Figure 1.4: Nuclear Magnetic Resonance principle. The magnetic moment $\overrightarrow{M}$ is described for the different stages. First the polarization aligns along the magnetic field. then the RF pulse is applied. Finally the magnetic moments come back to their equilibrium with a movement of precession.

Moreover, the detection of the relaxation always needs to be perpendicular to the field to measure the transverse components of the magnetic moment. But as we said before, after the RF pulse, magnetic moments will come back to their equilibrium, with a movement of precession at the Larmor frequency. To have access to this frequency, its amplitude, its bandwidth and enabling spectroscopy or imaging, the Fourier Transform of the signal has to be calculated. To measure it, I will present two basic pulse sequences which are possible: the Free Induction Decay (FID) and the Spin Echo.

Free Induction Decay (FID): This sequence is composed of a RF pulse which will switch the magnetization direction by an angle of $\frac{\pi}{2}$ in the laboratory system. Then magnetic moments will rotate at the same resonance frequency to come back to their equilibrium (see figure 1.5). We have to use a repetition time, time between two pulses, which is larger than the T_2 apparent to determine a proper signal.

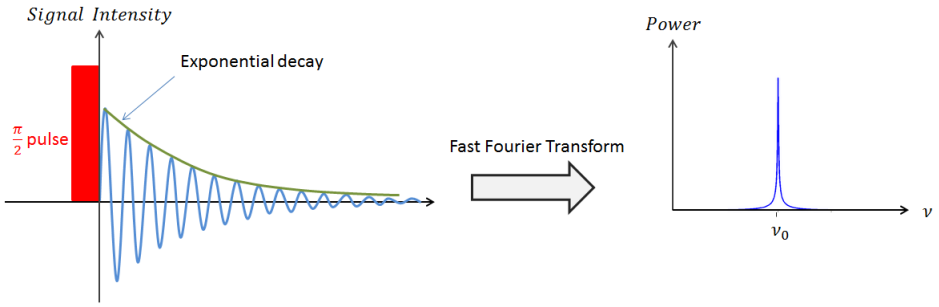

Figure 1.5: Free Induction decay and its Fast Fourier Transform.

Spin Echo Sequence: This sequence compared to the FID sequence, permits to work with a field which is not homogeneous [8], creating a reduction of the transverse magnetization decay time, different from the T_2, noted T_2^*. Indeed, as the Larmor frequency is linked to the field, if there is a small shift $\Delta\vec{B}$ in certain space region then there is a shift $\Delta\nu$ and then after a $\frac{\pi}{2}$ pulse all magnetic moments are not precessing at the same frequency (due to this inhomogeneity). At some point in time after the pulse $\left(\frac{TE}{2}\right)$, a π pulse is applied. After a time TE, for Time Echo, all magnetic moments rephase and produce a signal called an echo (see figure 1.6). In figure 1.7 are presented the different steps of a spin echo sequence for different magnetic moments.

To measure the true T_2, the CPMG (Car-Purcell-Meiboom-Gill) sequence is used. It consists in a train of spin echo sequence as presented on figure 1.8. The envelop of the echo amplitude decays with the time constant T_2.

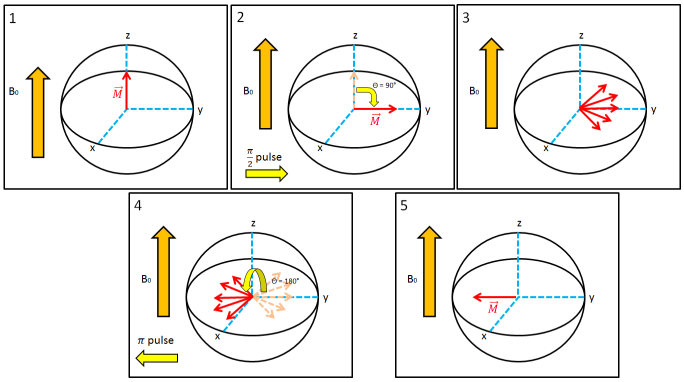

Figure 1.6: Different steps of a spin-echo sequence. 1/The vertical red arrow is the average magnetic moment of a group of spins. 2/ A $\frac{\pi}{2}$ pulse is applied to switch the magnetization direction. 3/ Due to local magnetic field inhomogeneities spins located in a low strength local field slow down whereas others located in a higher field strength accelerate. There is a dephasing. 4/ A π pulse is applied so that the slower spins lead ahead of the main moment and the fast ones trail behind. Progressively, the fast moments catch up with the main moment and the slow moments drift back toward the main moment. 5/ There is a complete refocusing of the spins and we see the echo.

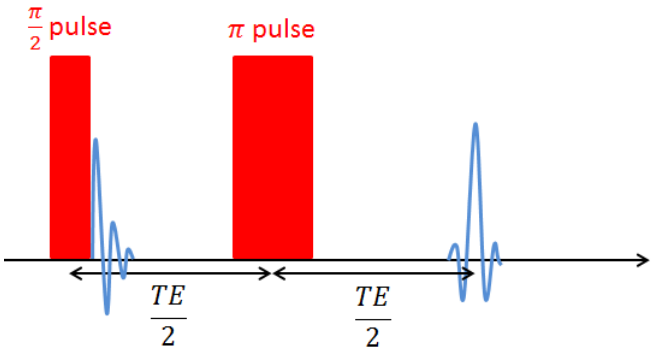

Figure 1.7: Spin-Echo sequence.

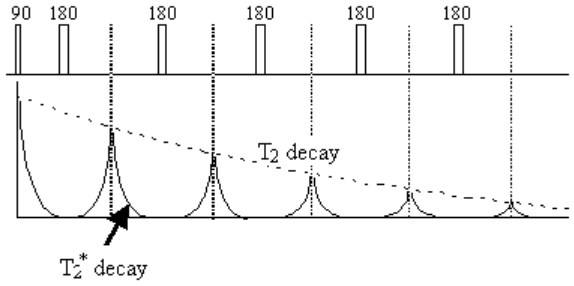

Figure 1.8: CPMG sequence showing a train of refocused spin echo. The dashed line is the envelope of the echo amplitude and decays with the time constant $\frac{1}{T_2}$; from *http://users.fmrib.ox.ac.uk/~stuart/thesis/chapter_2/section2_4.html.*

1.2 Nuclear Magnetic Resonance Spectroscopy

In this section, I will introduce the principle of Nuclear Magnetic Resonance Spectroscopy (NMRS) and more precisely the different types of interactions which lead to NMRS spectra. NMRS is a widely used technique which enables the study of molecules structures, interaction between molecules, molecular kinematic or dynamic, or even the composition of biological or synthetic mixtures.

To perform spectroscopy on hydrogen, the environment and how each hydrogen are linked to other atoms has to be taken into account. These environments induce a shift in resonance frequency. The analysis of these shifts gives inversely information on the environment. To illustrate this part, I will always consider a simple sample: ethanol.

1.3 Spin-electron interaction: chemical shift

1.3.1 Principle

The chemical shift, discovered independently in 1950 by *W. C. Proctor [56]* and *W. C. Dickinson [57]*, is a shift of the resonance frequency. This is due to the fact that the electron local distribution creates a partial screening of the external field B_0. So the magnetic field at the nucleus is not exactly the same as the external field.

$$B = B_0(1 - \sigma)$$

$$\gamma B = \gamma B_0 - \gamma B_0 \sigma$$

$$\sigma = \frac{\gamma B_0 - \gamma B}{\gamma B_0} = \delta$$

where σ is called the shielding factor and is of the order of 10^{-5} for protons.

As this screening effect is proportional to the external field, the chemical shift is commonly expressed in a unit, independent of the external field, it is noted δ and expressed in ppm :

$$\delta = \frac{Frequency\,of\,the\,signal - Frequency\,of\,reference}{Larmor\,frequency}.10^6$$

The frequency of reference is conventionally provided by a molecule which is well known: tetramethylsilane (TMS). TMS is always chosen as the reference since it has 12 hydrogen atoms. And due to its geometry they all have the same environment. A single peak is produced with a high intensity because of the number of hydrogen atoms. Moreover TMS is highly volatile and can easily be evaporated, which is convenient for recovery of samples.

The shielding factor is dependent on the nature of the around atoms and the around chemical bonds, the plot of the NMR spectrum can give us information on the geometry of a molecule or the composition of a sample. This chemical shift covers a range from 0 to 30 ppm, but the vast majority appear in the region of 0-10 ppm in the cas of protons.

1.3.2 Example

Ethanol, whose formula is CH_3-CH_2-OH, has three types of hydrogen. This induces a spectrum with three peaks first shown by *J.T and al* [58]. The splitting between peaks is already well known and given with TMS as reference.

The shift of ethanol hydrogen peaks are 1.11ppm for CH_3, 3.56ppm for CH_2 and 5.19ppm for OH.

We can have the type of graph such as on figure 1.9 where we see the different peaks of the different chemical shift.

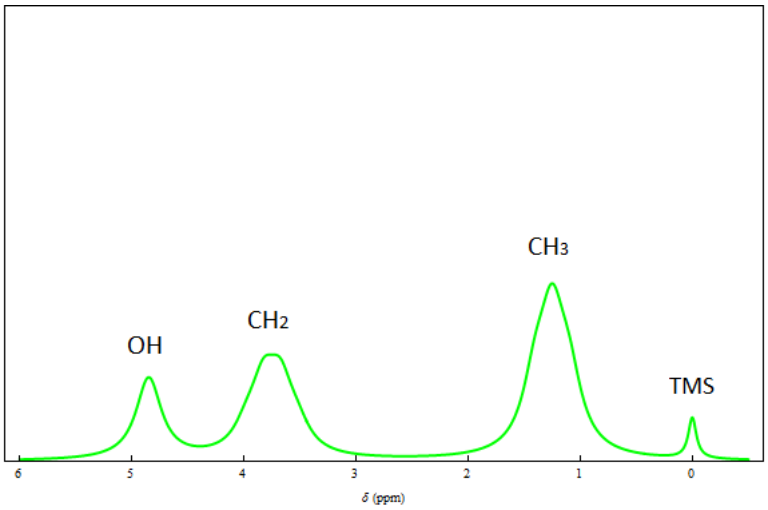

Figure 1.9: NMR spectrum of ethanol only considering the chemical shift.

In our case, we will work with a magnetic field going from 0.3T to 0.8T. This corresponds to chemical shift going from 12Hz to 35Hz per ppm.

1.4 Spin-spin interaction: J-coupling

1.4.1 Principle

In the case where you have enough resolution on spectra, you can see that some signals are made of many peaks, in fact peaks are splitted.

This coupling is due to space orientation, leading to direct coupling or to interaction between nuclei through bonding electrons, leading to indirect coupling.

The direct coupling finds its origin in the interaction of the magnetic moment. It can be shown that this interaction in liquids has a null average value.

The indirect coupling, also called scalar coupling comes from the fact that this interaction doesn't take into account the direction. We can distinguish two types of indirect coupling: heteronuclear and homonuclear.

Heteronuclear: when spins are bound to different nuclei. We call it ${}^1J$ coupling.

Homonuclear when spins are bound to the same types of nuclei. We call it ${}^nJ$ coupling with $n > 1$.

Coupling	Bounding number	Name
${}^2J$	2	Geminal
${}^3J$	3	Vicinal
${}^4J$	4	Long distance

Table 1.2: Different types of ${}^nJ$ coupling for $n = 2, 3, 4$.

This coupling constant is then independent of the applied field and varies as function of the nature of the bounding nuclei and is expressed in Hz.

The observed signal is a multiplet of peaks which are splitted following the $n+1$ rule, where n represents the number of neighbor spins coupled to the nuclei with the same coupling. For instance, if there are 2 neighbors, the observed signal is a triplet (2+1=3). Moreover, the intensity ratio of peaks is given by the Pascal's triangle. Thus a doublet has 1:1 or equal intensities, a triplet has an intensity ratio of 1:2:1, etc...

1.4.2 Example

Coming back to the ethanol example, the chemical shift, due to the presence of the three types of hydrogen, induces a NMR spectrum composed of three peaks. If we also take into account the J-coupling, a splitting of peaks appears into a singulet, a quadruplet and a triplet. For the triplet, the hydrogen has an interaction between them but also with the neighbors (the two hydrogen of the methylene function). So the peak is divided into three peaks. For the quadruplet it is the same thing with the three other hydrogen, so the peak is divided into four. For the proton of the hydrogen, it is alone since the alcohol function do not interact.

The combination of chemical shift and J-coupling lead to the NMR spectrum presented in figure 1.10

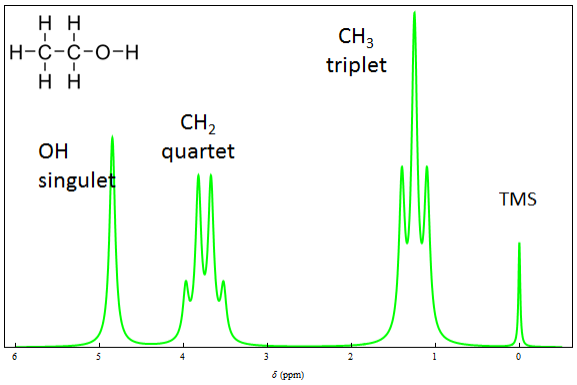

Figure 1.10: NMR spectrum of ethanol considering the chemical shift and the J-coupling.

1.5 Strong coupling regime

1.5.1 Principle

The strong coupling regime appears in the range of magnetic field where the nuclear Zeeman energies are comparable to the energies of the interactions between spins. In

other words, the J-coupling and chemical shift have similar energies. This results in intensity distortions, called "roof effect", and in new transitions which results in the apparition of new peaks. There is no simple methods to deduce the position and the intensities of the peaks. The eigenvalues and eigen vector of the Hamiltonian of the system have to be calculated.
The exact structure of a spectrum of a n spins system follows from the knowledge of the eigenvalues and eigen vector of the Hamiltonian.

$$\hat{H} = \hat{H}_Z + \hat{H}_J \tag{1.12}$$

With $\hat{H}_Z$ the term concerning the Zeeman interaction which represent the interaction between the spins and the B_0 field. It can be written as:

$$\hat{H}_Z = -\sum_{i=1}^{n} \nu_i \hat{I}_Z^i \tag{1.13}$$

where ν_i is the resonant frequency of the spin i and $\hat{I}_Z^i$ the operator associated to the direction z of the spin momentum and concerning the spin i.
And $\hat{H}_J$ the term concerning the indirect coupling (J-coupling) between the n nuclei:

$$\hat{H}_J = \sum_{i=1,\, j>1}^{n} J_{ij} \overrightarrow{\hat{I}_i} . \overrightarrow{\hat{I}_j} \tag{1.14}$$

where J_{ij} is the coupling constant between the spin i and j and $\overrightarrow{\hat{I}_i} . \overrightarrow{\hat{I}_j}$ is the scalar product of the two operators which can be expressed with the up and down operators such as:

$$\overrightarrow{\hat{I}_i} . \overrightarrow{\hat{I}_j} = \hat{I}_Z^i \hat{I}_Z^j + \frac{\left(\hat{I}_+^i \hat{I}_-^j + \hat{I}_-^i \hat{I}_+^j\right)}{2} \tag{1.15}$$

Thus to find eigenvalues and eigen vector of the Hamiltonian, the method consists in the construction of the matrix $[H]$ associated to $\hat{H}$ in a appropriate base. The example shows the resolution of this system for the ethanol molecule.

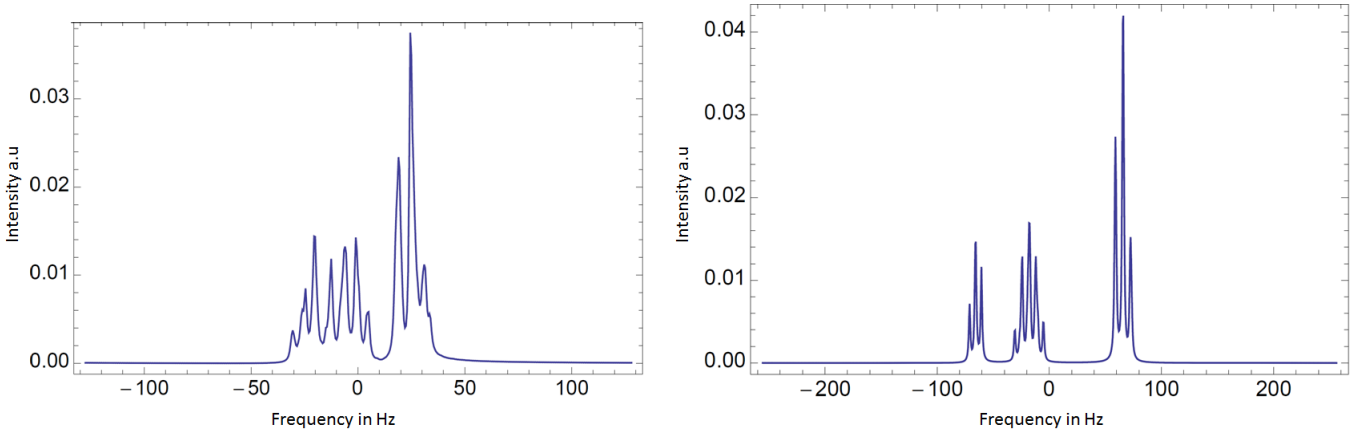

(a) (b)

Figure 1.11: Conventional NMR spectrum of ethanol in strong regime coupling at a)0.3T and b)0.8T.

1.5.2 Example

Considering the different chemical shift of CH_3: 1.25 ppm, CH_2: 3.70ppm and OH: 5.1ppm and also the different J coupling $CH_3 - CH_2$: 6.81Hz and $CH_2 - OH$: 5.37Hz, we are able to plot the two following graphs 1.11 for 0.3T and 0.8T :

We see that NMR spectrum of ethanol is very different between 0.3T and 0.8T. At 0.3T, the mixing of peaks and their distortions are clear whereas at 0.8T, the peak separation is better. Without the calculations, the analysis of such a spectrum can be difficult. For our application, as we do not have enough resolution, we won't consider too much this aspect.

1.6 2D and 3D spectroscopy

As we are talking about NMR spectroscopy, we have to make a short explanation about 2D and 3D NMR. Indeed, spectroscopy is not only limited to ethanol and can be applied to the study of large molecules like proteins. But it is well known that proteins are complex organic macromolecules containing carbon, hydrogen, oxygen, nitrogen, and usually sulfur and are composed of one or more chains of amino acids. The complex structure and the number of atoms lead to a complex NMR spectrum as presented in figure 1.12. We see that the 1D protein spectrum is really complex for interpretation as most of the signals overlap heavily.

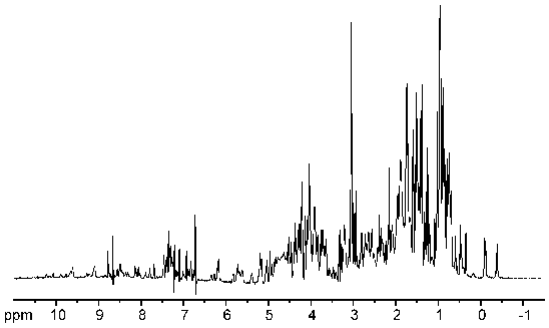

Figure 1.12: High resolution 1D NMR spectrum of a protein; from *http://www.cryst.bbk.ac.uk/PPS2/projects/schirra/html/2dnmr.html.*

For that reason, in 1971 the introduction of a new dimension by *J. Jeener [55]* was proposed.

A classical 2D NMR sequence is composed of 4 steps. The two first ones are the same as for the FID and corresponds to the preparation and the detection. After there is the addition of an evolution time and a step called mixing time as shown on figure 1.13. This type of pulse sequence is called COSY which is an acronym for COrrelation SpectroscopY

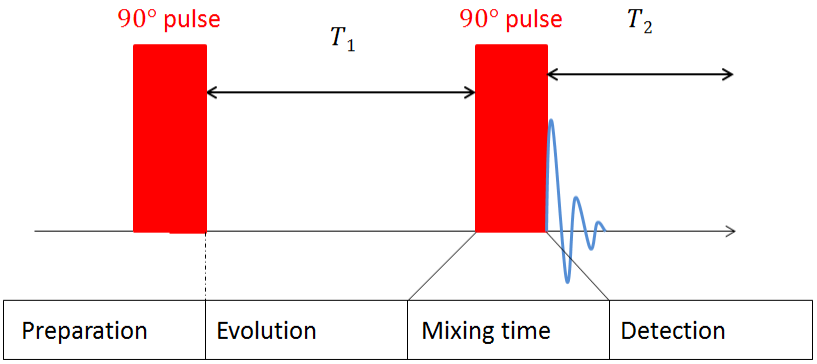

Figure 1.13: Classical 2D NMR pulse sequence experiment.

At the beginning the magnetization is aligned along the magnetic field. The pulse transfers the magnetization along a direction perpendicular to the field as for the FID. During the time T_1 magnetization precess with an angular momentum $\omega_0 = \gamma B_0$. As seen in 1.1.2, magnetization precess in the plane perpendicular to the field and the magnetization after the time $T_1$is :

$$M_x = M_0 sin(2\pi\upsilon t_1) e^{-\frac{t_1}{T_2}}$$

$$M_y = M_0 sin(2\pi\upsilon t_1) e^{-\frac{t_1}{T_2}}$$

Then a second pulse permits to transfer the magnetization in the direction $-z$. The detected part is then the remaining magnetization in the xy plane $M_0 sin(2\pi\upsilon t_1)$. The signal strength depends on the position after the evolution time T_1. The amplitude is modulated by T_1 compared to the Larmor frequency and the Fourier transform provides in the two dimensions the frequency due to the chemical shift. In case of spin-spin coupling, the second pulse does not only induce a change in the transverse magnetization but also in populations in the spin system.

Thus, there is an exchange of magnetization between all nuclei which are coupled together. Their signals are also modulated with respect to the frequencies of neighboring nuclei. This leads to the 2D spectrum peaks and allows us to obtain a spectrum where the homonuclear scalar coupling correlations are represented by spots that are off the diagonal.

As for example figure 1.14 presents a 2D COSY NMR spectrum of strychnine, allowing us to obtain a spectrum where the homonuclear scalar coupling correlations are represented by spots that are off the diagonal.

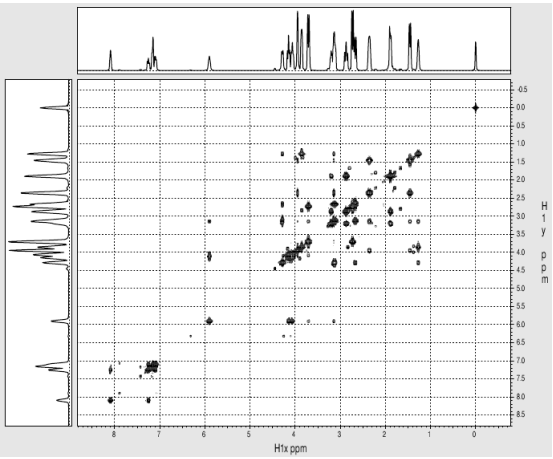

Figure 1.14: COSY NMR spectrum of strychnine; from *nmr.chem.ucsb.edu/protocols/homodec.html.*

With 2D NMR spectroscopy we see that we have much more workable information for complex molecules than in 1D spectrum. Nevertheless for the example presented on

figure 1.14 we see that for some peaks there is still some overlapping. For that reason a three dimensional NMR experiment was invented. It can easily be constructed from a two dimensional spectrum by inserting an additional indirect evolution time and a second mixing period between the first mixing period and the direct data acquisition. Each of the different indirect time periods (T_1, T_2) is incremented separately. The typical pulse sequence is presented on figure 1.15

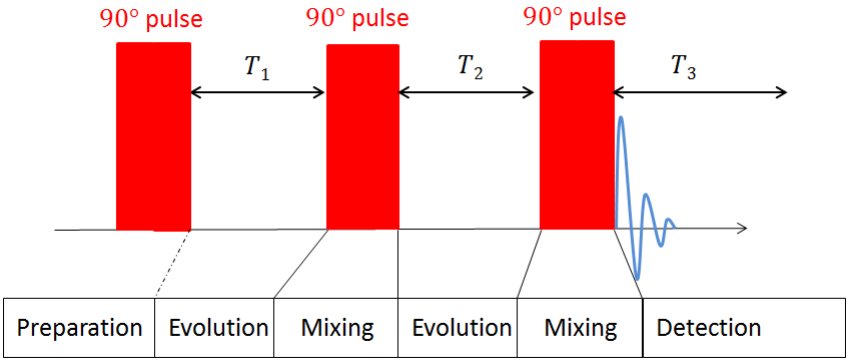

Figure 1.15: Classical 3D NMR pulse sequence experiment.

1.7 Detection methods

In this part we will review some of the techniques which are used to detect NMR signal and more precisely the techniques for local NMR measurements.

1.7.1 Tuned coil

The most common sensor to detect a NMR signal is the tuned coil. A tuned coil is a typical RLC circuit in which the coil is tuned to the working frequency thanks to a capacitance. In figure 1.16 is represented the schematic view of such a circuit. In that case, the resonance frequency is defined as:

$$\omega_0 = \frac{1}{\sqrt{LC}} \tag{1.16}$$

where L corresponds to the inductance of the coil and C to the tuning capacitance.

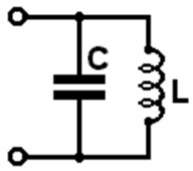

Figure 1.16: LC schematic circuit.

Some parameters are of prime importance when we are working with tuned coils and among them we can notice:

- *Flux going through the coil*

As the signal that we detect is the rotation of the magnetic moment, this creates in the coil by Lenz-Faraday effect an electromotive force (emf) *e.* This emf is proportional to the number of magnetic moments present in the sample positioned inside the tuned coil. The emf can be written as :

$$e = -\frac{d\phi}{dt} \tag{1.17}$$

where ϕ is the flux of the magnetic field. This magnetic flux emitted by the nuclear magnetization across the sensor surface can be express in a simple way using the reciprocity principle [13]:

$$\phi = \int_{Sample} \beta_1 \overrightarrow{(r)} \overrightarrow{M}(r) dV \tag{1.18}$$

With β_1 the field produced by unit of current in the conductor. If we consider that the field is created along the x axis, that means that the magnetization relaxes in the xy plan after a FID and if the magnetization is homogeneous over the sample, then we can write:

$$\phi = M_x \int_{Sample} \overrightarrow{\beta_{1x}}(r) dV \tag{1.19}$$

Where $M_x = M_0 cos\left(\omega_0 t + \phi\right)$. This oscillating flux induces in the coil the electromotive force e.

- *Filling Factor*

The filling factor η can be seen as the ratio of sample volume to the coil volume. But the filling factor is usually defined as the ratio of output energy of the sample to the total energy stored in the coil:

$$\eta = \frac{\int_{Sample} \overrightarrow{\beta_1}(r)^2 dV}{\int_{\infty l} \overrightarrow{\beta_1}(r)^2 dV} \tag{1.20}$$

By definition the total input energy from the coil is linked to its inductance as follow:

$$\mu_0 L = \int_{\infty} \beta_1 (r)^2 dV \tag{1.21}$$

- *Quality factor*

The quality factor Q is the ratio of the maximum magnetic energy stored by the coil divided by the average energy dissipated per radian by the coil. This can be seen as the ratio of the reactive impedance divided by the resistive impedance:

$$Q = \frac{L\omega}{R} \tag{1.22}$$

- *Noise related to RF coils*

In NMR, the major noise source is coming from the coil, but also from the environment. The first noise coming from the coil is called thermal noise [11] and corresponds to a fluctuation of an electric potential in the coil. The voltage mean square of this noise can be written in a bandwidth $\triangle f$ as:

$$< v^2 >= 4k_B T r \triangle f \tag{1.23}$$

At high frequency an electromagnetic effect appears called skin effect where the current tends to flow only on the surface of the conductor in a depth δ [14] which depends on the resistivity ρ and the frequency:

$$\delta = \sqrt{\frac{2\rho}{\omega\mu}} \tag{1.24}$$

This leads to an increase of the coil resistance that can be expressed as function of the length l, its radius r' and if we consider $\delta \ll r'$, it can be written as:

$$r = \rho \frac{l}{2\pi r' \delta} = \frac{l}{2\pi r'} \sqrt{\frac{\omega \mu \rho}{2}} \tag{1.25}$$

We see that to decrease the noise coming from the skin effect, the coil material should have the lowest resistivity possible.

Another noise that we can take into account is the noise coming from the sample. For conductive sample, eddy currents are created by the application of pulses. An induced resistance loss R can be written as [15]:

$$R \approx \frac{\mu_0^2 \omega_0^2 r'^3}{3\rho} \tag{1.26}$$

In general we can defined a total noise spectral density of the coil by:

$$S_v = 4k_B T(R_{coil} + R_{sample}) \tag{1.27}$$

The last important type of noise that we can take into account is the noise coming from the environment. This noise is due to electrical and mechanical noise associated with each component of instrument, to the displacement around the coil of magnetic objects, to the 50 Hz noise.We can minimize the environment noise by shielding the set-up.

Among all the different types of noise listed above, we will only consider the noise coming from the coil in the following parts since we ware working at relatively low frequency.

- *Signal to Noise Ratio (SNR)*

With the previous equations we are now able to give a prety good estimation of the SNR for a tuned coil. In this part, to simplify things, we will only consider a RF coil as an homogeneous solenoid with volume equal to the sample volume, so that we can say that:

$$\vec{\beta_1}(r) \approx \vec{\beta_1}(0) \tag{1.28}$$

where $r = 0$ corresponds to the center of the coil. Then the filling factor, flux and the total energy stored in the coil can be expressed in a simple way as:

$$\eta = \frac{V_S}{V_C},\ \phi = \tilde{M}_x \vec{\beta_1}(0) V_S \ and\ \beta_1(0) = \sqrt{\frac{\mu_0 L}{2V_C}} \tag{1.29}$$

where V_S is the sample volume and V_C is the coil volume and $\tilde{M}_x$ the amplitude of the Fourier transform of the component M_x. With a FID sequence, M_x can be written as :

$$M_x = M_0 e^{-\frac{t}{\tau}} cos(\omega t) \tag{1.30}$$

where τ is the transverse decay due to spin-spin relaxation then $\tau = T_2$ and $\tilde{M}_x = \frac{M_0 T_2}{\sqrt{2}}$. The flux can be reduced to:

$$\phi = \frac{M_0 T_2}{\sqrt{2}} \sqrt{\frac{\mu_0 L}{2V_C}} V_S = \eta \frac{M_0 T_2}{2} \sqrt{\mu_0 L V_C} \tag{1.31}$$

The signal-to-noise ratio, as it is indicated by its name, is the ratio between the signal detected by the coil divided by its noise. For the coil, the signal is defined as the electromotive force, which is expressed in equation 1.17 and the noise taken into account is the thermal noise defined by the equation 1.23.

In consequence the SNR for a solenoid coil and an acquisition bandwidth of 1Hz can be expressed as function of the different parameters as:

$$SNR = \frac{\omega \phi}{\sqrt{4 k_B T R}} = \frac{\eta M_0 T_2}{2} \sqrt{\frac{\omega Q \mu_0 V_C}{4 k_B T}} \tag{1.32}$$

We see that the signal is linked to the external field. But if the sample size decreases, the signal also decreases.

Improvement of NMR signal

One way to improve the NMR signal directly is to play with the sample size. Indeed to reach the highest signal, we need to have highest filling factor η. That means that the coil geometry should perfectly match the sample [13].

Another way to improve the NMR signal is to increase the field strength. As the signal is linked to the sample magnetization, using a higher magnetic field provides a better SNR. Here I present only some techniques allowing the enhancement of the signal strength without increasing the main field.

The first technique called magnetization prepolarization. This technique consists in applying a strong magnetic field during a time T, and then the spin precession is measured at a lower field. This way the signal is strongly enhanced. The measurement is not performed with this strong magnetic field since the prepolarization technique doesn't require an homogeneous field. This way coil designs, for magnetization prepolariation, are simple and cheap. The main problem with this technique is that the application of a strong magnetic field just before the acquisition creates some induced Eddy currents, circular electric currents induced within conductors by a changing magnetic field in the conductor, which can be detrimental to the field homogeneity.

To use further the prepolarization advantages, noble gas can be added inside the sample. Noble gas, for example ^{129}Xe or ^{3}H, are used to transfer their polarization to ^{1}H. Alkali vapor of Rb are polarized by a laser beam, and this polarization is then transferred by spin exchange to Xe atoms. Contrary to the previous technique, this one doesn't require a strong magnetic field and allows to keep intact the homogeneity of the field.

Another technique called Dynamic Nuclear Polarization (DNP) is also often used. This technique, based on Overhauser effect [47], permits to enhance the nuclear magnetization by transferring spin polarization from electrons to nuclei. Unpaired electron spins are added to the studied sample. A RF pulse at the frequency of the electron spin resonance (ESR) is applied. Once the saturation is reached, a transfer of polarization from electron to nuclear spin occurs. The non-equilibrium polarization created is much larger than the corresponding thermal equilibrium polarization.

A last technique called Signal amplification by Reversible Exchange (SABRE) [48] is also proposed. It uses para-H_2 as a source of polarization.

1.7.2 Microcoil

As presented before, one of the best ways to improve the signal-to-noise ratio is to create a coil that perfectly fits the sample size. For samples of micron size, there is a need to fabricate coil also of micron size. Two possibilities are presented, hand-made fabrication and microfabication. Moreover, two types of microcoils can be designed, solenoidal and planar having both their advantages and disadvantages.

1.7.2.1 Solenoidal coils

Coils can be hand-made by winding a wire around a tube. For a microcoil, automated methods have to be used to reach the sub millimiter size. The first relevant method is brought by *Zhang and al.* [16]who automated the winding of a thin copper wire around a quartz capillary in order to perform NMR spectroscopy, see figure 1.17. Another suitable method by *Kratt and al.* [17] combines the automated method with clean room techniques. In this case, they used an automated wire bonding to wind a thin wire gold around thick SU-8 resist hollow cylinders, allowing the possibility to insert a core inside. With this method they could fabricate coils of 100µm of diameter and 550µm height, see figure 1.18.

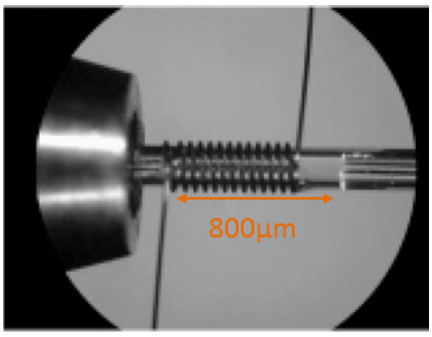

Figure 1.17: Automated wire bonding around a quartz capillary [16].

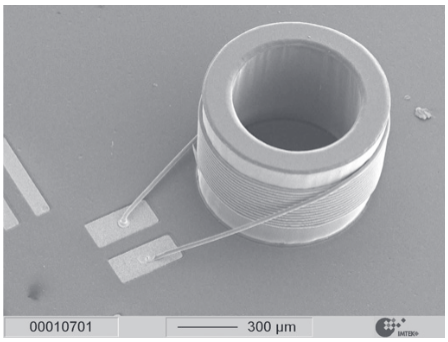

Figure 1.18: Automated wire winding around SU-8 resist hollow cylinder [17].

Other alternatives techniques have been developed and in particular the utilization of microfabrication techniques.

One of the solenoidal coils made with microfabrication technique is presented by *Rogers and al.* [18]. This technique permits to obtain a microcoil around a quartz capillary. The first step consists in evaporating by electron beam evaporation thin layers of titanium and silver. The capillary is then rolled on these lines so that ink generates a coil on the surface of the cylinder. After that a wet etching permits to obtain a microcoil by etching the entire surface which is not protected by the ink. Finally the coil copper layer is deposited on it by electrodeposition. This technique even if it a nice technique in term of microfabrication technique, is difficult to implement. On figure 1.19 is presented the final coil fabricated with this method.

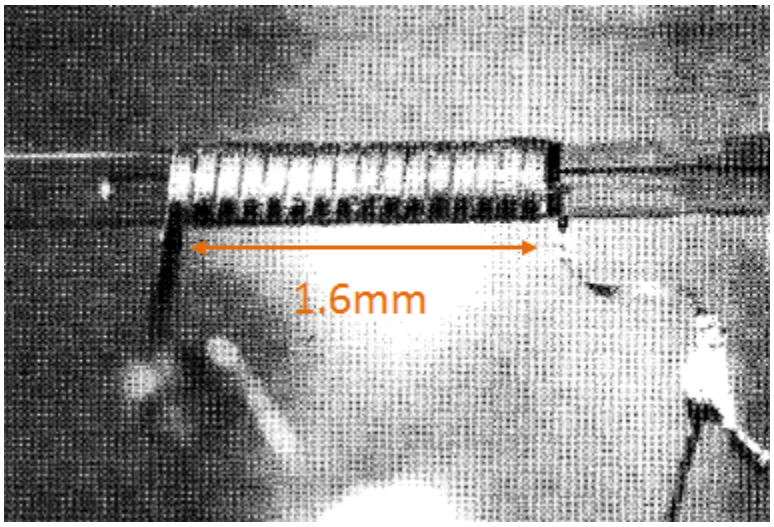

Figure 1.19: Microprinting coil around a microcapillary[18].

Another technique reported by *Sillerud and al. [21]* is the same as the microprinting on quartz capillary, that means that on capillary is deposited by e-beam evaporation layers of chromium and gold. That the coil is then designed with a focused ion beam that will etch these layers. Figure 1.20 shows the final microcoil.

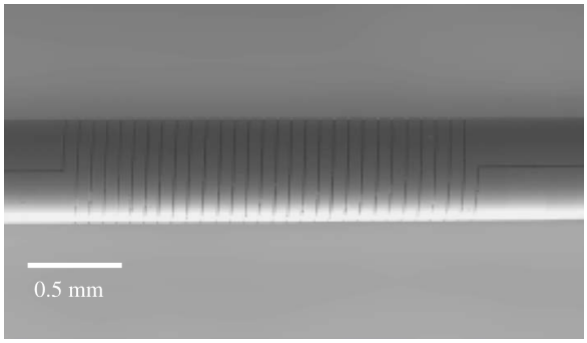

Figure 1.20: Ion etching coil *[21]*.

For other applications, *Park and al. [19],* presented another technique to obtain 3D microcoils. The first step consists in micromolding lower traces by copper electrodeposition. Pillars are defined by UV lithography and micromolded by copper electrodeposition. Using the same sequence, top tracks are deposited in order to end the coil. The final step consists in a lift-off to remove resist present in the microcoil. With this technique they could fabricate coil with dimensions of 700µm length, 400µm width and 40µm height, as presented in figure 1.21. *Woytasik and al. [20]* also developed a technique for 3D microcoil by micromolding to elaborate microcoils on flexible substrates to allow their location as close as possible to the surface to be characterized.

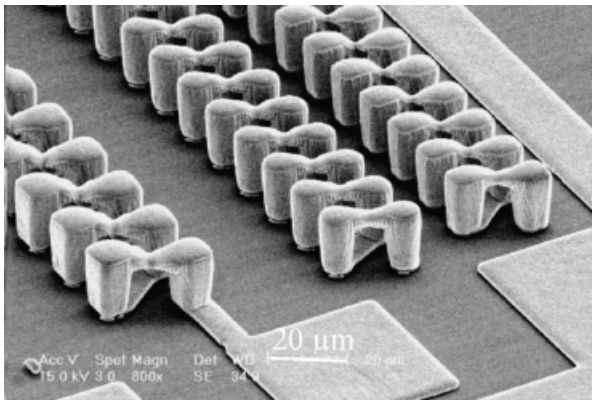

Figure 1.21: Micromolded microcoil *[20].*

Alternative techniques are also used to make 3D microcoils starting from in-plane microcoils. In order to do this, a mechanical deformation as to be done. These mechanical deformations can be of three types: folding in out-of-plane the coil [22], application of a magnetic field [23] or utilization of stress-engineered thin films [24]. NMR spectroscopy experiment has never been done so far on the fabricated microcoils using microfabrication techniques.

1.7.2.2 Planar coils

Even though tridimentional microcoils offers some advantages, such as increasing the filling factor by matching the probe to the sample volume or increasing the sensitivity of low concentration compound, their process of fabrication remains complex and the positioning of the sample is critical. That's why planar coils are developed. With the use of microfabrication, the mass production is easy and the structures can also easily be integrated into lab-on-chip. Planar coils are mainly used for two types of applications, non-invasive and in-vivo, and for these different applications their way of fabrication, their sizes, their shapes are different.

Planar coils and Helmholtz coil First, I present planar coils and Helmholtz coil for non-invasive applications. These coils positioned closely to the sample to study, microchannel or microtank, have the advantage to be easily fabricated and with a mass production but also can be bonded to the outer circuit with microbounding.

Stoker and al. [25] presented a method to achieve microspectroscopy NMR with a 60µm planar coil. Coils were made on GaAs substrate with a combination of microfabrication techniques such as electroplating technologies, a process that uses electric current to reduce dissolved metal cations so that they form a coherent metal coating on an electrode and lift-off. On top of the coil they put a quartz capillary in which there is the liquid to study so that about 1nL is present in the sensitive area. NMR spectroscopy was performed at 5.9T and obtained a line-width of 2Hz from a water sample. This

line-width of 2Hz which represents an homogeneity of $8.10^{-3} ppm$ which is appropriate for spectroscopy where you need to be very precise on the spectrum. Moreover for each acquisition they have a SNR of 25, which is also impressive since for spectroscopy application the spectrum is acquired in a quick time.

In a same way, *Massin and al. [26]* performed the same experience with a microcoil on glass using SU-8 resist and copper electrodeposition.

Implantable planar coil Another alternative of microfludic systems for local NMR is to study the sample in its own environment, that means in-vivo. For this application, special coils are developed. For instance *Renaud and al.* [28] designed a sensor of a needle shape (Figure 1.22). The microcoils are process always with the microfabrication techniques and then the silicon wafer is cut with a die saw to obtain the needle shape. At the top of the needle is present the microcoil of 1000µm length and 500µm width.

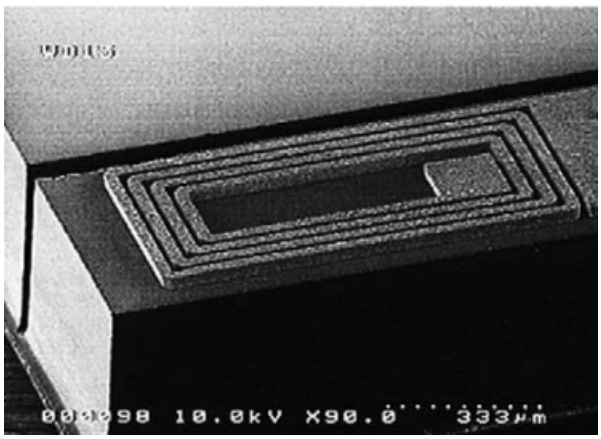

Figure 1.22: Planar coil at the top of the silicon needle [28].

The main difficulties with all theses techniques, is to have a good quality factor for the microcoils. Indeed, the quality factor, which indicates a lower rate of energy loss relative to the stored energy of the resonator, needs to be as important as possible to reduce the number of acquisitions. For microcoils, this quality factor cannot be as important as sub millimiter sized coils. Indeed, planar coils require the use of micron-sized wires which increases the resistivity of the coils. As the quality factor is defined as $Q = \frac{L\omega}{R}$, a high resistivity implies a low quality factor.

Moreover, the microcoils are limited in term of fabrication. They can't reach a size under 100µm due to the fabrication process.Working volumes smaller than the microcoil size, decease the filling factor and increase the number of acquisitions to have a good SNR.

On table 1.3 present the different characteristics and performance of the microcoils for NMR applications. We can see that in practice the volume involved are in the range of thenth of hundred of nL.

Detection Method	Author	Magnetic Field B_0 (T)	Dimension	SNR/nL/acq
Solenoidal coil	*Rogers and al.* [18]	7.05 T	324µm of diameter 1600µm long	$5,9.10^{-1}$
Solenoidal coil	*Sillerud and al. [21]*	1.04T	550µm of diameter 2100µm long	$4,1.10^{-1}$
Planar coil	*Stoker and al.* [25]	5.9 T	200µm of diameter	25
Planar coil	*Massin and al. [26]*	7 T	500µm of diameter	$1,2.10^{-1}$
Implantable coil	*Renaud and al.* [28]	2 T	500µm width 1000µm long	$1,4.10^{-4}$

Table 1.3: Comparaison of the different techniques et caracteristiques of microcoils for NMR application.

1.7.3 Microfabricated Atomic Optical Magnetometers

Based on the principle of magnetic-field-dependence of the polarization of light resonantly[29], this technique is among the most sensitive technologies to detect and characterize magnetic fields. Microfabricated atomic magnetometers possess a high sensitivity. Thanks to the development of microfabrication techniques, encapsulation, their size can be decreased to work on small samples. Moreover they are low-power consumption and less expensive because they can work without cryogenic cooling and more portable than conventional devices such as SQUIDs.

1.7.3.1 Principle of operation

The central element of an atomic magnetometer is the glass cell filled with an alkali gas such as potassium, cesium, rubidium since they present an intrinsic magnetic moment due to their unpaired electrons. Without external perturbations, all these moments are all randomly aligned. The first step is to create a macroscopic magnetic moment with the mechanism of optical pumping [30]. With the application of a light though the gas, each magnetic moment will aligned along the light direction and then create a global magnetic moment. The magnetic field to measure creates the precession at the Larmor frequency of the magnetic moments in the direction of the external field to sense. To measure this magnetic field, another light polarized linearly is sent in the gas, this is called the optical probing [31]. The absorption and dispersion properties of the light change as function of the precession and thus of the applied field.

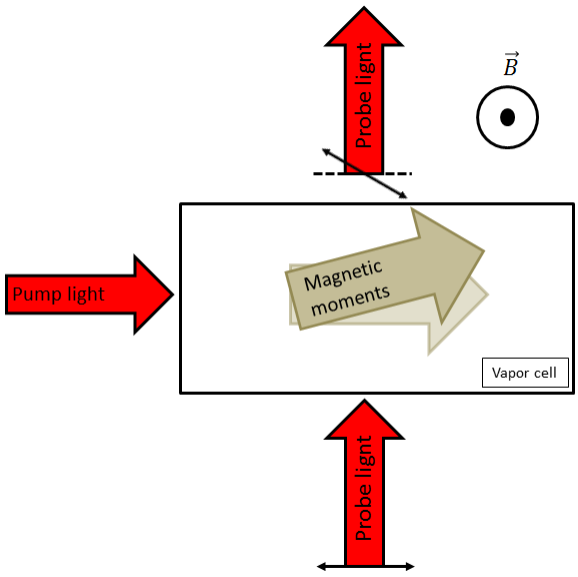

Figure 1.23: Principle of an Atomic Optical Magnetometer. Pump light polarizes the atoms, atomic polarization evolves in the magnetic field, and the resultant state of the atoms' polarization is detected by measuring the polarization rotation of the probe light.

A new type of atomic magnetometers SERF, Spin Exchange Relaxation-Free [32] are also developed. These sensors are made with a high density of alkali vapor of about $10^{14} cm^{-3}$ so that spin exchange is fast compared to their magnetic precession frequency. As a result the average spin interacts with the field and is not destroyed by decoherence, inducing an improved dectectivity.

1.7.3.2 NMR applications

Atomic magnetometers can be used for NMR detection. Although their fabrication is not easy, *Peter and al* [33] managed to miniaturized the sensor size to $12mm^3$. This was performed with the microelectromechanical techniques and has the advantages to be low-power consumption and also to be produced at the wafer lever.

We saw that one possibility to improve of NMR signal was to increase the magnetic field. Classeical atomic magnetometers in this range of magnetic field. That's why *Savukov and al. [35]* developed a magnetometer that can work in the RF range of frequency. To do so, vapor of potassium is optically pumped and placed into a static magnetic field such as the Zeeman resonance of alkali atoms is tuned at the signal frequency.

Then any transverse signal at this frequency will induce a transverse polarization of the atomic spin:

$$P_x = \frac{1}{2}\gamma B_1 T_2 sin\left(\omega_0 t\right)$$

where T_2 is the transverse spin relaxation time. With this configuration, they succed to tune the magnetometer at 99kHz. Later [36], they manage to record a NMR signal of water on a sample of 3cm by 4cm cylindrical glass. The sample was placed 5cm far from the magnetometer and prepolarized at 0.14T with a permanent magnet and the NMR signal is recorded at 62kHz.

For local NMR, *Ledbetter and al. [34]* did spectroscopy on tap-water of a mass-limited sample. They demonstrated a detection method where the sensor is distant from the sample. The atomic magnetometer operates in the regime of SERF and the cell gas is filled with Cs and N_2 at 5000 Torr. To bring water close to the sensor, a microfluidic channel is fabricated. The fluid is first prepolarised at 1T. With this technique they could detect the signal of tap-water on a volume of 1µL. They achieved a line-width of 26 Hz, which represents an homogeneity of $420ppm$ and had a signal-to-noise ratio of 3 for each acquisition. This way they are competitive with microcoils which are actually used for NMR applications.

1.7.4 Single Nitrogen-Vacancy centers in diamond

The main advantage with NV center is that it can be used as a nanoscale magnetic field sensor, and very weak field can be detected.

1.7.4.1 Principle of operation

A Nitrogen-Vacancy (NV) center corresponds to a point defect in the diamond lattice. In fact it is a substitution of a carbon atom by a nitrogen atom such that it creates an excess of one unpaired electron that can be localized on this defect (figure 1.24).

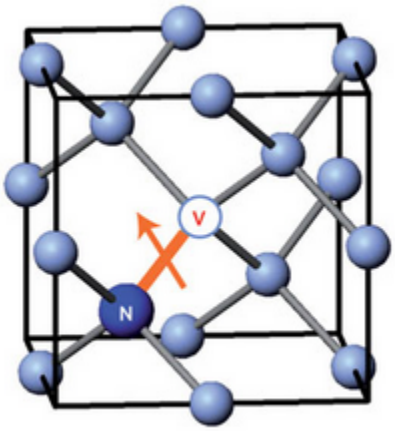

Figure 1.24: Structure of a NV center diamond[37].

There are then two possible states $N-V^-$ and $N-V^0$. Indeed, when the NV center is placed close to a donor electron, an additional unpaired electron can be given to the vacancy site leading to a negatively charged center: $N-V^-$ and to a global spin $S=1$. When the NV center is far from a donor electron, the site keeps its neutral state. But for magnetometry applications, the $N-V^-$ configuration is favorable since $N-V^0$ has not yet been explored for spin manipulations.

The fundamental state is then characterized by a triplet whose degeneracy is removed by the spin-spin interaction into a doublet $m_s = \pm 1$ and a singulet $m_s = 0$. The first excited states is also a triplet and the energy difference between the two states corresponds to $1.945eV$. When an external field is applied, a lifting of degeneracy of the two states $m_s = +1$ and $m_s = -1$ is added and corresponds to $2g\mu_B B_{NV}$ where g is the Lande factor, μ_B the Bohr magneton and B_{NV} the external field (figure 1.25).

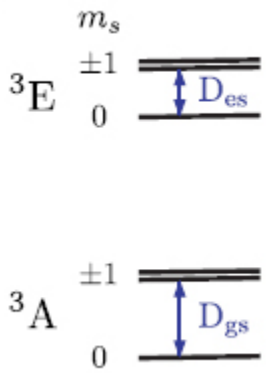

Figure 1.25: Simplified energy-level diagram of the NV center. Dgs and Des correspond respectively, to the zero-field splitting between ms = 0 and ms = ±1 in the triplet ground state ^3A and in the triplet excited state ^3E [37].

With an electron spin resonance (ESR) measurement, it is possible to measure the amplitude of the magnetic field and its orientation compared with the NV center [37] : $\Delta \approx Dcos2\theta$ where D is a parameter of lifting of degeneracy.

1.7.4.2 NMR applications

Staudacher and al. [38] managed to detect a NMR signal on a sample volume of $5nm^3$ where the sensor is 7nm far form the sample. In order to perform this detection, they used the "quantum lock-in detection" method [39]. This allows increasing sensitivity while reducing susceptibility to noise. They managed to obtain an NMR signal on oil and $PMMA$ (a polymer called Poly(methyl methacrylate)) with a line-width of respectively of 14.4 kHz and 46.6kHz. In spite of the fact that this is on a very small sample volume and that they obtained a signal, the obtained line-width is not good enough to perform spectroscopy.

1.8 Micro imaging

The last part that I will develop is called micro-imaging.

As for conventional MRI, the principle is to select a particular space region that we want to study by using a field gradient. This gradient superimposed to the main field and is giving to the local field a spatial dependance:

$$G_i = \frac{\partial B_z}{\partial i} \tag{1.33}$$

Where G_i is the gradient along the direction i and z the direction of the main field. The total field can be expressed by:

$$B_z(\overrightarrow{r}) = B_0 + G_i \overrightarrow{i} . \overrightarrow{r} \tag{1.34}$$

Then the measurement of the frequency gives an information of the location within the sample. Indeed by playing on each gradients, we can define a specific space region and perform a non-invasive NMR measurement.

The resolution of an MRI image is defined by voxels size. Voxels resolution are determined by thickness, field-of-view and matrix element in x and y directions. Conventional MRI achieves a voxel size of the order of few mm^3.

Improving spatial resolution requires longer acquisitions, which is hardly possible with alive samples. But µMRI permits to have a local information in a limited time on in-vivo sample and without intrusion into the sample. In order to have this information, coils geometry are optimized to perfectly match the size of the sample, for example a knee or a head. The major problem to have a small voxel, and then a local information, is to have a precise control of gradients. In clinical MRI setups, gradients are of the order of $100mT.cm^{-1}$ to achieve a resolution of about $1mm^3$. Submillimeter resolution would require gradients of the order of $10T.cm^{-1}$. This can be reached with the use of microcoils presented previously. *Grant and al.* [49] demonstrated imaging on a single neuron. The localized volume was about $220 \times 200 \times 220\mu m^3$.

Other in-vivo measurement have been proven by *A. C. Wright and al. [59]* with RF coil cooled down to 77K. They did two measurements. The first was a demonstration on a phalanx of the right middle finger with a magnetic field of 1.5T and on a voxel of $78 \times 78 \times 1000\mu m^3$. The advantage to work with cooled coils is that the quality factor is better than room temperature coils. Indeed cooling down permits to reduce the coil noise. The other measurement was on a rabbit eye to demonstrate that ophthalmologist imaging was possible. But this technic is only possible for some specific samples.

Another in-vivo measurement has been proven by *J. C. Ginefri and al.* [65] with a RF coil at 7T where they did two measurements. One measurement was performed on a phantom and the other one on a rat brain. The RF coil was fabricated on a flexible polymeric material with an outer diameter of 5.4mm.With the phantom experiment they had a spatial resolution of $220 \times 200\mu m^2$. With the rat brain experiment they had a spatial resolution of $150 \times 150\mu m^2$. Although this technic enables to image micron sizes volume, it is not possible to perform measurement deep into the matter. We only can have a surfacic information.

This technique is also widely used in biology for the study of water, lipid, and carbohydrate distribution in grape berries [60] or for the study of cell metabolism [61].

Conclusion

We saw in this chapter an overview of NMR spectroscopy and Micro-imaging. Different approaches exist and have their own advantages and disadvantages. Tuned coils are the conventional approach for NMR applications. To study millimeter and micron sizes sample, µcoils are develloped. But their fabrication can be a true restraint. Moreover tuned coils are adapted to a specific frequency which also can be a restriction for some applications. We also mentionned atomic optical magnetometers which require the use of optical equipment which can be expensive, their fabrication can also be difficult but are very sensitive and allow to work on small volumes, but spectroscopy is presently

not possible. Single NV-centers are also ultra sensitive, work on very small volumes and are in-vivo compatible but are limited in spectral resolution. Finally µImaging has the advantage to be non invasive but requires a high field and the use of micro-gradient which is complex to implement.

Moreover, we saw that NMRS is a powerful technique to determine the structure of complex samples such as proteins and also the sample properties. As it is a non-invasive technique, it give access to the study of in-vivo samples.

Nowadays there is no real tools that can be easily implemented for NMRS to work on volumes below 1nL.

Chapter 2

MagnetoResistive sensors

The aim of this chapter is to give a brief overview of magnetoresistive effects and how these effects can be used for sensor applications. For that, we will explore the physical origin of the magnetoresistance whether it is giant or tunnel. Knowing the elements that are crucial for a significant magnetoresistance we will understand what makes a good device for sensing a field and how this device behaves in presence of an external field. Finally we will describe the set-up where these sensors will be placed to detect NMR signals.

2.1 Principle

Since the discovery of the electron in 1897 by Joseph John Thomson, a new branch of physics was born: electronics. Electronics is the science that studies electric conduction. This new discovery field got a real direct impact on our usual life with the invention of the transistor in 1947 by W. Shockley, J. Bardeen and W. Brattain. It relies on the principle of charge transfer processes fully ignoring the spin of the electron. Previously, in 1857, William Thomson has discovered another phenomenon: magnetoresistance [4]. This magnetoresistance, which is a galvanomagnetic effect, is a change of resistivity of some materials under a magnetic field. This is also linked with the electronic transport, but in that case, it takes into account the spin of the electron. Spintronics is born.

Spintronics is based on four effects:

- Spin asymmetry. Indeed, in magnetic materials, the number of spins up and down is different, this leads to the apparition of a macroscopic magnetic moment. Moreover, conductive electrons may also have a large asymmetry in spin orbital moment.
- Two conduction channels. The electron spin is conserved on a length scale larger than the spin scattering process (probability of spin inversion is negligible). As a consequence, two conduction channels exist in parallel for spin up and spin down. It is the Mott approximation [1].

- Spin dependent diffusion. The spin diffusion probability will be different for spin up and down conductive electrons as they are parallel or anti-parallel to the magnetization of the layer.
- Spin accumulation. When current is injected from a magnetic material to a non magnetic material, there is apparition of a discordance since the number of spin up and spin down electrons is different in the magnetic material whereas it is the same in the non magnetic material. This will create a transition zone in which the spin asymmetry slowly decreases. The low probability of diffusion with spin flip induces large spin diffusion length.

Theses effects leads to the creation of magnetoresistive devices. Here are the most commonly used devices:

- Anisotropic MagnetoResistance (AMR) which results from the variation of resistivity with the angle between the current flow and the magnetization of the material. This effect arises from the spin-orbit interaction and the magnetization. The scattering of electrons from the s to the d bands is higher when the electrons propagates parallel to the magnetization.
- Giant MagnetoResistance (GMR) was discovered in 1988 in iron (magnetic layer) / chromium (nonmagnetic layer) multilayer by Albert Fert and Peter Grünberg [2][8]. Due to the anti-ferromagnetic exchange coupling between the layers, at zero external field, direction of magnetic moments of the ferromagnetic layers are anti-parallel. In this case, both electron channels are strongly diffused and the result is a high resistivity. When a magnetic filed is applied, strong enough to align the magnetic moments in the same direction, one electron channel is slightly diffused and the result is a low resistivity. Nowadays, more complex artificial structures called Spin Valves were developed to increase their sensitivities to use them as hard-drive read head or for ultra sensitive field sensors.
- Tunnel MagnetoResistance (TMR) was observed in tunnel junction ferromagnetic/insulator/ferromagnetic [3]. A similar behavior as GMR was observed, that means a high variation of resistivity of the junction when the orientation of the ferromagnetic layers changes but the physical mechanism is not the same. Indeed in that case, magnetoresistance is mainly due to the spin asymmetry but also to the electronic structure of the insulator and to the character of the electronic links at the ferromagnetic/insulator interface.

2.1.1 Physical origin of GMR

The observation of the Giant MagnetoResistance in a Fe/Co multilayer ($Fe_{3nm}/Cr_{0.9nm}$) leaded to a Nobel prize in 2007. Within just a decade GMR sensors have been introduced in all hard-disk read-out units. This effect was called Giant MagnetoResistance as it was much larger than usual anisotropic magnetoresistance.

Two major properties have been then underscored. The first one is the existence of an anti-ferromagnetic coupling between magnetization of iron layers through chromium layers. This tends to orientate the magnetization of the iron layer in an anti-parallel way in the absence of magnetic field. When a magnetic field is applied in the structure plane, the magnetization tends to align parallel to the field. The second property is that while there is the changing in the orientation of the magnetization in iron layers, there is a huge diminution of the resistivity.

GMR effect results from a spin asymmetry of the resistivity in magnetic multilayer. Indeed, magnetic layers that are used in spin electronics are ferromagnetic transition metals such as Fe, Ni, Co. Thus, conduction is insured by electron from under-bands s, d or hybrid sd, as presented figure 2.1. In a first approximation it can be considered that electrons of spin up and down conduct current independently [1]. We have a two currents model, the total current being the sum of the two channels due to spin up and down electrons.

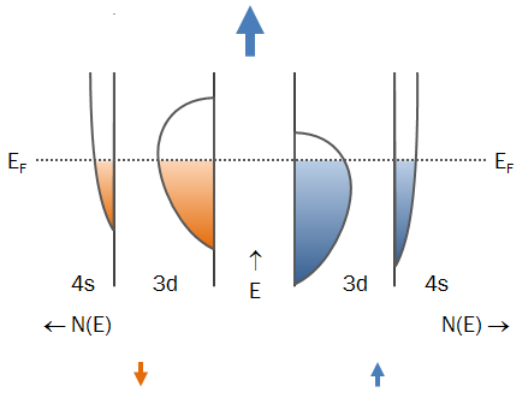

Figure 2.1: Band structure of a ferromagnetic metal, presenting the under-band s and d and the fermi energy level.

Moreover, ferromagnetic transition metals have a difference of state density up and down of the 3d band at the Fermi level (figure 2.2).

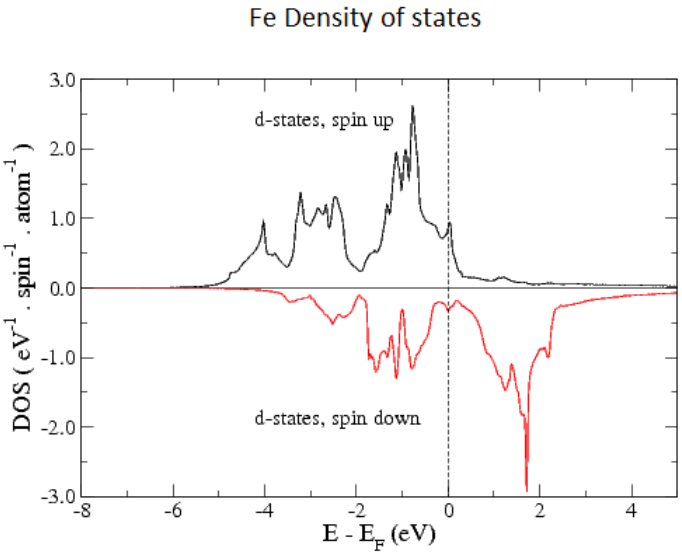

Figure 2.2: Density of States of iron for spin up and down; from *http://www.chiraltem.physics.at/ChiPrag.html*.

This will lead to a different transition probability for spin up and down electrons. In layers where they are in majority, that means electrons aligned in the same direction of the magnetization layer will have a higher conductivity than in layers where they are in minority. In fact, high density of states leads to a stronger scattering and therefore a shorter mean free path.

A spin valve is a GMR device composed of two ferromagnetic layers, separated by a non magnetic layer and is characterized by a resistance variation when the magnetization direction of the magnetic layers changes. Figure 2.3 underscores the resistance variation in function of the magnetic layers direction.

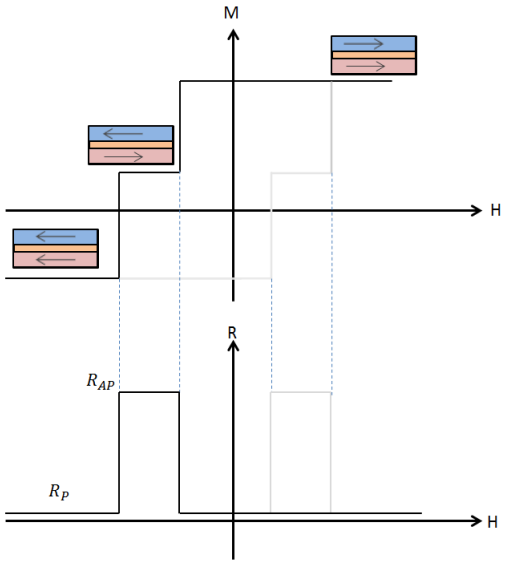

Figure 2.3: Magnetization cycle as function of the scanning magnetic field. The hard layer is characterized by a high coercivity and the soft layer by a low coercivity.

We can distinguish two cases. One case where the two magnetic layers are in the anti-parallel state and one case where the two magnetic layers are in the parallel state.

- Anti-parallel case: in this case each type of electron is alternately strongly and weakly diffused when they get through the magnetic layers (figure 2.4). We can then deduce from that the equivalent electric model. Then the spin valve resistivity equivalent R_{AP} is the following: $R_{AP} = \frac{r+R}{2}$ where r is the resistance corresponding to an electron whose spin is parallel to the corresponding layer and R is the resistance corresponding to an electron whose spin is anti-parallel to the layer.

- Parallel case: when the magnetization layers are aligned, spin up electrons, respectively spin down electrons, are electrons in majority, minority, in all layers so weakly, strongly, diffused (figure 2.5). In the same spirit as previously, resistivity equivalent R_P is the following: $R_P = 2\left(\frac{rR}{r+R}\right)$.

Finally, we can deduce the normalized variation of resistivity:

$$GMR = \frac{\triangle R}{R_{AP}} = \frac{R_{AP} - R_P}{R_{AP}} = \frac{(R-r)^2}{4Rr} \tag{2.1}$$

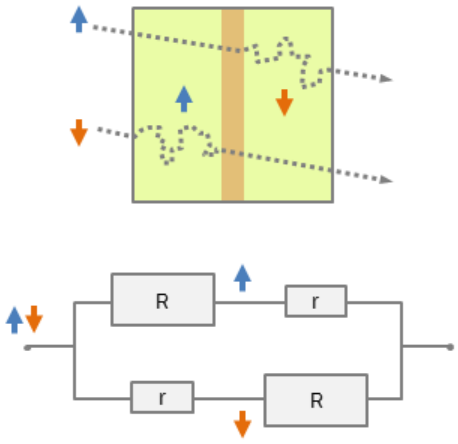

Figure 2.4: Spin valve where layers magnetization are in the anti parallel configuration. We can see the diffusion for both spin and also the electric equivalent circuit.

This equation is valid while layers thickness are thin compared to the spin diffusion length in current perpendicular to plane (CPP) configuration and to the mean free path in current in-plane (CIP) configuration. Indeed there are two measurement configurations possibilities which are CIP, for current in plane, and CPP, for current perpendicular to plane. This is well illustrated in figure 2.6. *Pratt. and al. [44]* underscored the fact that measuring a GMR spin valve with the current perpendicular to plane could increase the magnetoresistance by 50% at 4.2K. Working in CPP configuration with structures of micron size will lead to a very low resistance, making any measurement impossible, for that reason we only work in CIP configuration.

From all this, we can deduce that to obtain a high magnetoresistance, we need a high contrast of diffusion between spin up and spin down, which may come from the thickness of the magnetic layers or to the interfaces with the non magnetic metal.

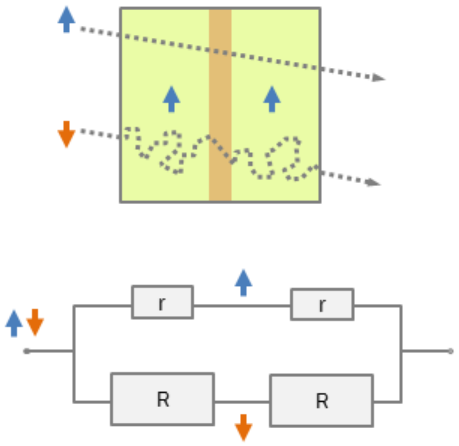

Figure 2.5: Spin valve where layers magnetization are in the parallel configuration. We can see the diffusion for both spin and also the electric equivalent circuit.

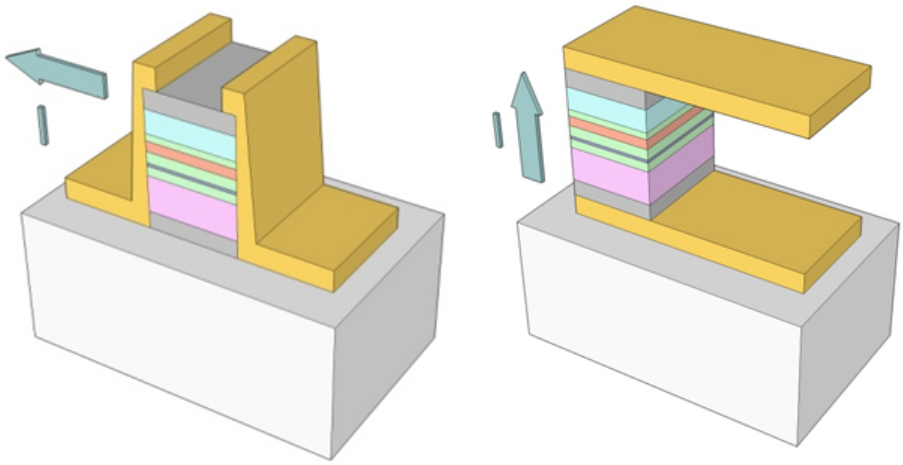

(a) (b)

Figure 2.6: GMR device in a) CIP configuration and b) CPP configuration.

Another key element for the GMR characterization is the sensitivity. The sensitivity is defined as:

$$s_{GMR} = \frac{1}{R_0}\frac{\triangle R}{\triangle H} \tag{2.2}$$

To have a good sensor, a high sensitivity is necessary.

2.1.2 Physical origin of TMR

Another type of magnetoresistive sensors could be used for this work: magnetic tunnel junctions. The use of these sensors types are of a great advantage, since comparatively to GMR, at room temperature, the magnetoresistance ratio can reach 200-300% [46].

In this part, I will first make a quick remind on tunneling effect and then on the physical origin of TMR.

Tunneling effect Magnetic tunnel junctions are composed of an thin insulating layer between two ferromagnetic metallic electrodes. While an electric potential difference is applied between the two electrodes, a current appears. That's the tunneling current. This tunneling current comes from the fact that the electron is seen not only as a particle but also as wave. That is the effect highlighted by de Broglie: the wave–particle duality. The electron posses a non-negligible probability to propagate trough a potential barrier. This current can be written as:

$$I_{tunneling}\,\alpha\, Ae^{-2dK} \tag{2.3}$$

The current decreases exponentially with the thickness d of the barrier, A and K are constants that depend on the properties of the barrier and the energy applied between the two electrodes.With a simple calculus, we can realize that when the distance d is increased by 1Å, the current is divided by 10, highlighting the importance of a good control of the width tunnel barrier.

Tunneling MagnetoResistance principle Magnetic tunnel junctions are composed of three elements which are a "free" layer and a "pinned" layer spaced by a thin insulating layer. When a potential difference is applied between the two electrodes and if the insulated layer is thin enough, a tunneling current is created.

The Tunnel MagnetoResistance (TMR) is characterized by a resistance variation when the magnetization direction of the magnetic layers changes. Figure 2.7 underscores the resistance variation in function of the magnetic layers direction.

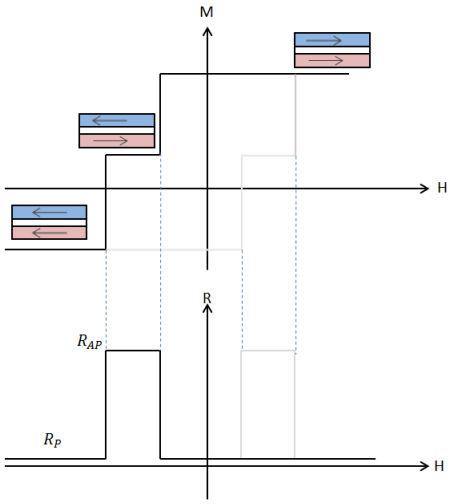

Figure 2.7: Magnetization cycle in function of the magnetic field. The hard layer is characterized by a high coercivity and the soft layer by a low coercivity.

Like for the GMR effect, we define the tunneling magnetoresistance by the following ratio:

$$TMR = \frac{R_{AP} - R_P}{R_P} = \frac{G_P - G_{AP}}{G_{AP}} \tag{2.4}$$

Where R_{AP} is the resistance when the junction is in the anti-parallel state and R_P the resistance in the parallel state and G the corresponding conductances.

Physical origin of TMR The easiest way, to understand the variation phenomenon of the resistance considering the magnetization direction of the ferromagnetic layers, is to consider the Jullière model [45]. This model is based on two main hypothesis.

The first one is that electron spins are conserved as they pass through the tunnel barrier. Thus, as for GMR, a two conduction channels model can be used.

The second one is based on the golden Fermi rule which says that: the tunneling current of each conduction channel is proportional to the product of the densities of tunneling states of the ferromagnetic materials of which the two electrodes are made. However, we have seen in the previous part that densities states of electron up and down were asymmetric. In figure 2.8 is presented a diagram that underscores the tunneling magnetoresistance effect. On the same figure we can defined n and N the densities of state of the minority and majority electrons.

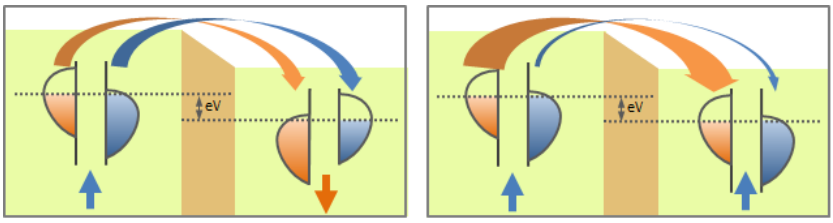

Figure 2.8: Tunneling transport between two ferromagnetic electrodes spaced by an thin insulating barrier under the action of a potential difference. The densities of states are represented by the parabola shifted in energy.

In the configuration where the magnetizations of the electrode are in the parallel state, the majority channel of an electrode corresponds to a majority channel on the other electrode. This leads to a large conductance thus a low resistance. Conversely, a minority channel electrode corresponds to a minority channel on the other electrode. This leads to a low conductance thus an important resistance. This is what is illustrated in the first part of the diagram.

In the configuration where the magnetizations of the electrodes are in the anti-parallel state, the majority channel of an electrode corresponds to a minority channel on the other electrode. This leads to a low conductance thus a higher resistance. Conversely, a minority channel electrode corresponds to a majority channel on the other electrode. This leads to a high conductance thus an low resistance. This is what is illustrated in the second part of the diagram .

When we model this by an equivalent circuit diagram, we have a higher equivalent resistance in the anti-parallel configuration than in the parallel configuration.

TMR is then expressed, according to the densities of state of the electrodes, as follows:

$$TMR = \frac{D_L^{\uparrow} D_R^{\uparrow} - D_L^{\uparrow} D_R^{\downarrow} - D_L^{\downarrow} D_R^{\uparrow}}{D_L^{\uparrow} D_R^{\downarrow} + D_L^{\downarrow} D_R^{\uparrow}} \tag{2.5}$$

Where D corresponds to the density of state of left and right electrode for up and down spins.

TMR can also be expressed, according to the densities of state of the minority and majority electrons, as:

$$TMR = \frac{(n-N)^2}{2nN} \tag{2.6}$$

By setting the polarization as follow:

$$P = \frac{D^{\uparrow}(E_f) - D^{\downarrow}(E_f)}{D^{\uparrow}(E_f) + D^{\downarrow}(E_f)} \, or \, P = \frac{(n-N)}{(n+N)} \tag{2.7}$$

We can the express the TMR as function of the polarization:

$$TMR = \frac{2P_L P_R}{1 - P_L P_R} \tag{2.8}$$

We can conclude that the more the polarization of magnetic metals is close to 100% and the more important the value of the TMR will be. However, in this model, the probability of electron transmission is not taken into account. But this is a good model to understand the tunneling magnetoresistance effect .

Although these sensors present a higher signal-to-noise ratio at room temperature, during this thesis I didn't used them for two main reasons. First we have to process them in CPP configuration. Yet, to have this configuration, you have to perfectly control the etching with an in-situ control. Usually, a SIMS (Secondary Ion Mass Spectroscopy) which analyzes in real time the molecules ejected from the etched surface is used. This necessary machine was not present at the lab. Secondly, these devices are very fragile to any overvoltage. So we decided to validate local NMR concepts with GMR.

2.2 Description of a spin valve

Typical spin valve stacks that are used for our sensors are composed of a hard layer, a spacer and a soft layer. In figure 2.9 is presented the whole stack.

- On the substrate we first have the seed layer which will help the deposition and influence the microstructure of the overlayers. It is generally a tantalum layer.
- Then we have the hard layer. It is called hard layer, a layer whose magnetization orientation is independent from the external field. This layer is obtained by coupling an anti-ferromagnetic layer with a ferromagnetic layer. This coupling comes from the fact that when a ferromagnetic material is in contact with a anti-ferromagnetic material, at the interface, a direct coupling exists which tends to align magnetic moments by exchange interaction. IrMn or PtMn are often chosen as the anti-ferromagnetic layer since they have a high exchange field, they are also highly resistive to induce minimal shunting. They are corrosion resistant and are thermally stable. Meanwhile CoFe is chosen for its high spin polarization. Moreover, this hard layer is often reinforced by an artificial anti-ferromagnetic such as CoFe/Ru/CoFe, which permits to have a zero net magnetization.
- Next we have the spacer. This layer is present to magnetically decouple the ferromagnetic layers. Cu is the best choice compared to Ag or Au. Indeed, the magnetoresistance obtained with Cu is higher than magnetoresistance obtained

with Ag or Au. Furthermore the thickness which provides us the best magnetoresistance is around 2 nm [5]. In fact, thinner: ferromagnetic layers are coupled and thicker there is a spin memory loss.

- Next we have the free layer. This layer is in reality composed of two layers, a first one which is ferromagnetic with a high spin polarization but high coercivity, CoFe and another layer also ferromagnetic but which is magnetically a soft layer, for instance NiFe. Magnetoresistance is also maximized for a certain thickness value around 5nm [5]. Thinner there is diffusive scattering at the boundaries determinant and thicker the conductance in the outer parts shunts the alignment-dependent conductance.

- The final layer is a Tantalum layer. It is present for tow reasons. The first one is to protect the spin valve from oxidation, the other one is to permit the deposition of other layers on top of it as for instance contacts.

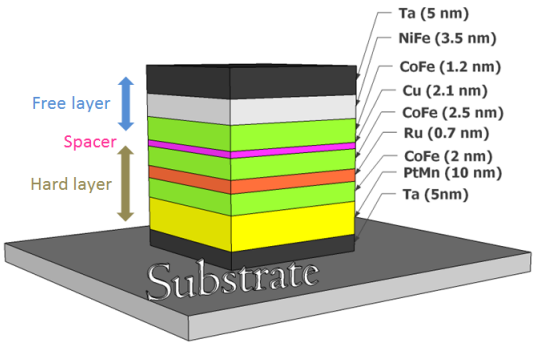

Figure 2.9: Spin valve stack composition with the different layers and their thickness.

2.3 Linearization of a sensor

2.3.1 Shape anisotropy

For sensors applications, we need to be sensitive around zero field. For this reason we need to work in cross anisotropy [40]. That means that we need to have the free layer perpendicular to the pinned layer. In order to have this configuration, the free layer is "pinned" with the anisotropy form with special form as yoke or meander. Figure 2.11 shows a yoke shape. Consequently to obtain the MR curve we place the sensor in the field such that the yoke or the meander is perpendicular to this field. The typical curve that we obtain is presented figure 2.10.

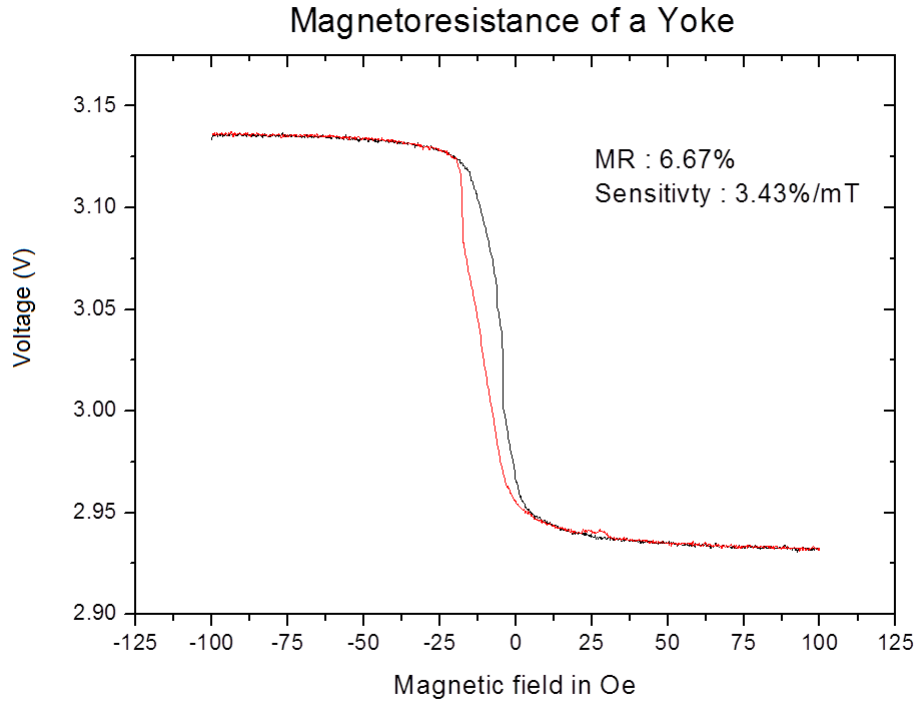

Figure 2.10: Magnetoresistance of a yoke as function of the scanning magnetic field.

Moreover, for sensors applications, we also need to have a reversible and coherent magnetic response. Indeed some hysteretic responses can occur in microscopic-sized magnetic layers due to the formation of magnetic domains. For this reason yoke shapes and meander shapes are chosen [41]. The advantage of such a design is double. First the active part of the yoke is formed of a single domain, see figure 2.11. As a consequence when the sensor is placed into a magnetic field, the magnetization of the free layer should move linearly. The other advantage is the reduction of the magnetic noise at low frequency which is welcome for sensor application where you need to reach high sensitivity and low noise.

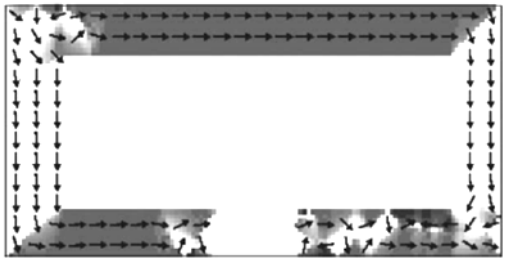

Figure 2.11: Magnetic moment distribution of a yoke. The arrow direction and the color gives the direction of the magnetic domain of the free layer composed of NiFe in absence of external field.[41].

If the width of the sensor is larger than 4µm the shape anisotropy is not strong enough to have a linear response at 0 field. We then may use an external longitudinal bias magnet to ensure it.

2.3.2 Magnetic bias

2.3.2.1 In-plane magnetic bias parallel to the yoke

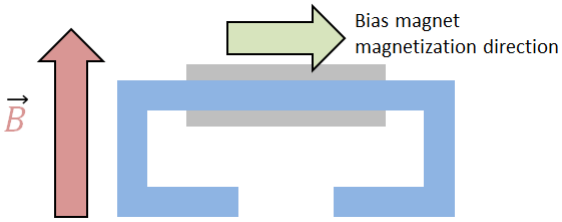

Figure 2.12: Direction of the scanning field in red; direction of the bias magnet in green; yoke shape GMR sensor in blue.

In absence of magnetic field, we see on figure 2.13 that the resistance as function of the field presents an hysteresis. The application of a magnetic field along the direction of the yoke, as presented on figure 2.12, results in the reduction of the hysteresis. This is due to the fact that the free layer never sees a 0 field and ensure a coherent rotation.

We see on figure 2.13 that the centering of the curve hasn't change but we see the hysteresis disappears with a loss of sensitivity.

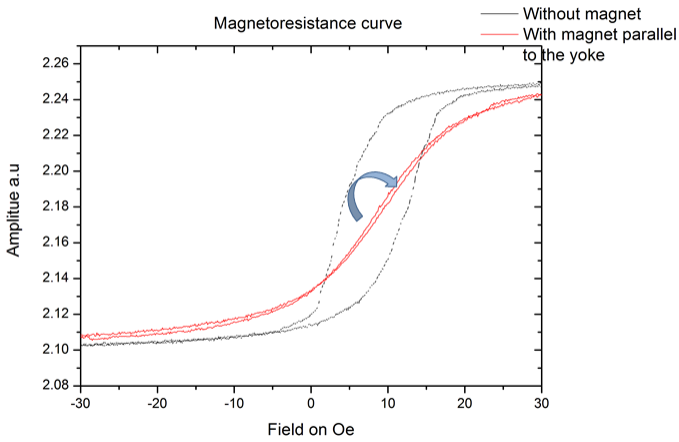

Figure 2.13: Magnetoresistance curve of a yoke in blue and the magnetoresistance curve of the same yoke with a bias magnet parallel to the yoke.

2.3.2.2 In-plane magnetic bias perpendicular to the yoke

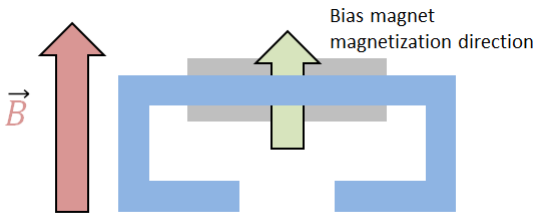

Figure 2.14: Direction of the scanning field in red; direction of the bias magnet in green; yoke shape GMR sensor in blue.

In absence of magnetic field, we see on figure 2.13 that the resistance as function of the field is centered around 5Oe. The application of magnetic field perpendicular to the direction of the yoke, as presented on figure 2.14, results in the shifting of the curve. This can be easily understood by the fact that at zero field the added magnetic field still creates a field. Then the $R(H)$ curve is shifted in the direction of the added magnetic field.

We see on figure 2.15 that the curve is well just shifted on the left.

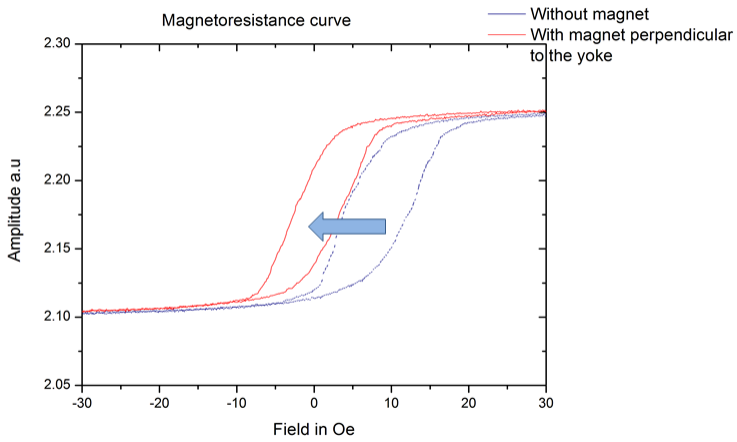

Figure 2.15: Magnetoresistance curve of a yoke in blue and the magnetoresistance curve of the same yoke with a bias magnet perpendicular to the yoke.

2.3.2.3 External field out of plane of the yoke

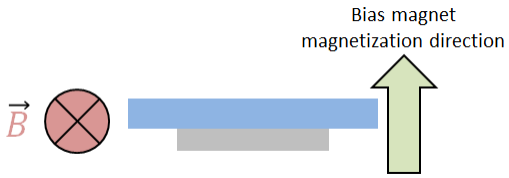

Figure 2.16: Side view of the direction of the scanning field in red; direction of the bias magnet in green; yoke shape GMR sensor in blue.

To well understand what happens when a magnetic field is applied perpendicularly to the GMR stack, figure 2.16, we have to come to the definition of the dipolar energy. When a material is immersed into a magnetic field $\vec{H}$, this one acts as a dipole. This energy comes from the interaction between the dipolar field and the orientation distribution. We can express this energy as:

$$E_d = \frac{1}{2}\mu_0(\overrightarrow{H_d}.\vec{M}) \tag{2.9}$$

Where $\overrightarrow{H_d}$ is the demagnetizing field also called stray field, is the magnetic field generated by the magnetization. $\overrightarrow{H_d}$ can be defined as:

$$\overrightarrow{H_d} = -\overline{\overline{N}}\vec{M}$$

Where $\overline{\overline{N}}$ is the form factor. And if we consider a thin layer we can write:

$$\overline{\overline{N}} = \begin{bmatrix} 0 & 0 & 0 \\ 0 & 0 & 0 \\ 0 & 0 & 1 \end{bmatrix}$$

Finally the demagnetizing field is:

$$\overrightarrow{H_d} = -Mcos(\theta)\overrightarrow{u_z}$$

For a thin layer of Ni/Fe whose magnetization is in-plane we have a $H_d = 8,5.10^5 A/m$ which corresponds to $1T$.

To have a better idea of what is happening, we can see figure 2.17

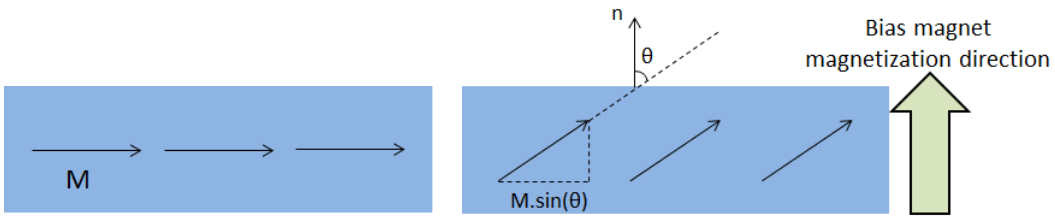

Figure 2.17: Magnetization direction of the layers of a GMR sensor without (a) and with (b) the presence of a bias magnet.

In fact our GMR stack has a spontaneous in-plane magnetization. When the external field is applied, magnetization layers begin to move out of plane. And the residual in-plane magnetization $M.sin\theta$ decreases. This induces a decrease of magnetoresistance until the layer magnetization is completely out of plane.

This last part will be explained more precisely in part 3.2.3, with in particular the plot of the sensitivitya s function of the external field perpendicular to the stack.

2.4 GMR sensors for NMR

2.4.1 Lithographic process

An important work during this thesis was devoted to sensors fabrication. For this, I used some techniques which are specific to the nanotechnologies environment. In the following part, I will explain the different steps for a sensor fabrication. First of all, we must speak about stacks that are used. They are not done by the CEA, but they come from laboratories with whom the CEA collaborates. Theses collaborators are quite numerous but we can mention INESC-MN(Instituto de Engenharia de Sistemas e Computadores – Microsistemas & Nanotechnologias in Lisbon directed by Paolo Freitas), TCD (Trinity Collège of Dublin, laboratory CRANN directed by Mike Coey), Naomi-Sensitec a German company situated in the Mainz, or Allegro Microsystem an American firm situated in Mineapolis (USA). We thus received full GMR wafers; ready to be microprocessed into sensors.

In figure 2.18 is presented the different steps for the GMR process.

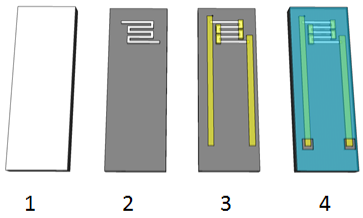

Figure 2.18: Sum-up of the GMR process 1. Cleaning of the full GMR wafer; 2. Definition and etching of the meander shape; 3.Contact deposition in Ti/Au; 4. Passivation layer of Alumina.

2.4.1.1 Cleaning

To develop a structure of the micrometer size as sensors are, we have to work in a clean environment that means with very few particles present in the air. In the CEA Saclay, we work in a class 1000 clean room.

One of the first steps when we have our samples is to clean them. Indeed, during the transport to our laboratory, all wafers are covered with resist to avoid any damage on the sample surface. Cleaning consists in three steps.

In the first step, the sample is placed in an acetone bath. This acetone bath eliminates any trace of organic residue such as the protection resit. In practice the sample is placed in a glassware, himself put in a hot ultrasound tank.

The second step consists in an isopropanol bath. This isoproanol bath eliminates any trace of acetone remaining on it.

The third and final step consists in washing with deionized water. This step will remove any residual dust still present on the sample.

Once these steps done, we dry with a nitrogen jet. If we consider that the sample is clean enough, you can go to the next step. Otherwise the process is repeated until the sample is clean.

2.4.1.2 Photolithography

Photolithography, also called optical lithography, is a process used in microfabrication to pattern parts of a thin film from a bulk substrate. It consists in the use of light to transfer a geometric pattern from a photomask to a light-sensitive chemical "photoresist", or simply "resist", on the substrate.

Before spreading resist on the sample, a pre-annealing is done at 100°C to remove by evaporation any solvent traces. This pre-annealing also permits to improve the photoresist grip and homogeneity during the spin coating. To obtain a thin photoresist layer on the sample we use a spinner. The photoresist, used is the S1813, from Shipley, which enable us to obtain a layer of about 1.3µm if it is spinned at 5000rpm during 60sec. A positive resist is a photosensitive polymer whose chain links are broken during an UV exposure. A revelator, AZ351B, dissolves the insolated resist so that we are able, thanks to a mask, to pattern any design on a sample. For that we use a UV mask aligner MJB3 (Karl Suss), of 365nm wavelength and 10mW/cm^2 power, to place very precisely the sample under the mask. The mask is composed of two parts. One part in quartz which lets the UV pass and one part in chromium which blocks them and thus defines the sensor shape after development in the revelator.

In table 2.1 are presented parameters used for the photolitography.

Resist	Spinner recipe	Annealing	Exposure time	Revelator time
S-1813	500 rpm 5sec - 5000 60 sec	3min at 100°C	13 sec	MF 319 45 sec

Table 2.1: Photolithography parameters.

2.4.1.3 Ionic etching

Lithography permits to define specific patterns. The next step consists in etching to transfer the defined patterns on the GMR. In order to do it, an ion beam etching is used. In this frame we perform a physical etching. That means that we do not use a reactive gas to etch but only ion bombardment with an inert gas, such as argon. Thus we have an anisotropic etching. Accelerated argon ions will strike the wafer surface, resulting in the dislocation of the surface atoms. Power is provided by a RF energy source. In table 2.2 are presented the different parameters used for this etching.

Once the etching done, it only remains to remove the resist present on the sample. For this, just like for cleaning, the wafer is bathed into acetone. By the end we have our GMR that has the desired shape for the sensor.

Ar Pressure	Voltage	Electrode Voltage	RF frequency	RF power	I
$1{,}1.10^{-4}$mbar	152 V	700 V	13 MHz	90 W	7 mA

Table 2.2: Etching parameters in the sputter chamber where Voltage stands for the voltage applied to accelerate ions on the sample and Electrode Voltage stands for the voltage applied to extract electrons from the electrode.

2.4.1.4 Contact deposition

Once our sensor shape defined on the GMR, we need to make measurements of it. Therefore we have to deposit contacts. For this, we perform the same procedure as before, that means that we do a photolithography of our contacts on the sample. This step is quite difficult since it requires that contacts are relatively well aligned with the yoke. To make this alignment precisely marks are present on the mask and also on the sample. In my case alignments marks were cross that needed to be fitted into each other. Figure 2.19 shows a microscope picture of marks alignments.

Figure 2.19: Cross alignment marks. In yellow the mark made by the contact depostion.

The deposit itself is composed of two layers which are Ta/Cu/Ta or Ti/Au. The first configuration in Ta/Cu/Ta is not a good choice and this for the simple reason that when the sensor is immersed into a liquid, copper oxidizes, even with the presence of a passivation layer on top of it, see figure 2.20. For that reason Ti/Au is thereafter selected.

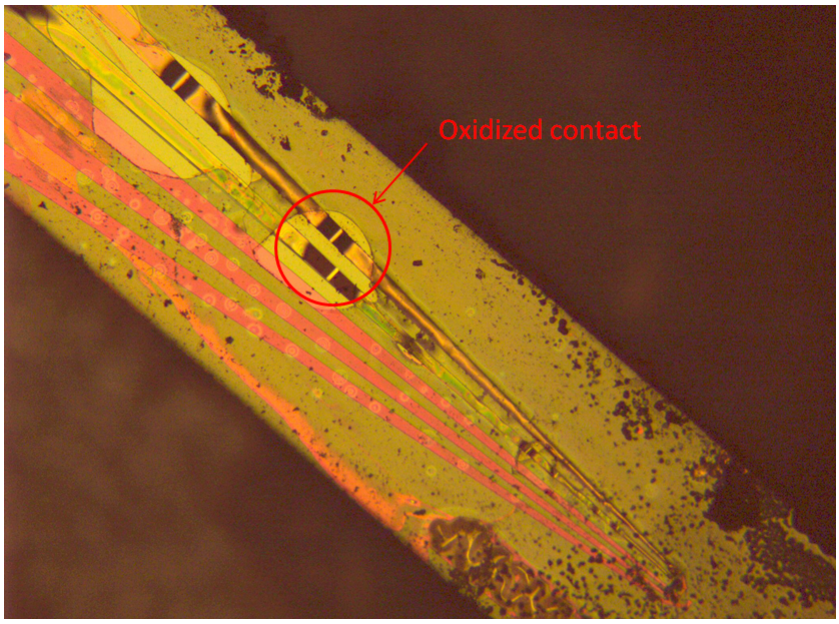

Figure 2.20: Oxidized Ta/Cu: Ta contacts after 2 days immersed in water.

The first layer of Titanium is called an adhesive layer, to increase the adhesion between the substrate and gold layer. The choice of this conductive layer is very important since we need to choose a material with a low contact resistivity and also a good stability. Moreover as our sensor will be immersed in liquid, we need a material which does not oxidize and that is the case for gold.

The deposition is performed with an Electron Beam Evaporation chamber. It consists in, a chamber with a very low pressure (10^{-7} mbar) to allow passage of electrons from the electron gun to the material to evaporate. Electron beam is generated and accelerated up to a high kinetic energy and directed towards the material to evaporate. It results in a production of heat. Due to temperature and vacuum level, the material evaporates and coats our surface sample placed in front of the target. In table 2.3 are present the different parameters used for this E-beam evaporation.

Material	Pressure	High Tension	Source current	Deposition rate
Ti	$1{,}1.10^{-7}$mbar	9 kV	66 mA	0,8Å/sec
Au	$4{,}0.10^{-7}$mbar	9 kV	300 mA	1,2Å/sec

Table 2.3: Evaporation parameters in the E-beam chamber.

Once all layers are deposited, just as before, we need to remove the resist present on the sample (and at the same time layers present on the resist). This step is called the lift-off. The major difficulty with this method is the grip of the deposited material on the sample. Indeed, if grip is not good enough, all the deposited material will leave

during the lift-off, hence the importance of pre-etching 30 seconds the sample before deposition.

2.4.1.5 GMR passivation

Before using our sensor, we have to protect it against oxidation and also against fluid on which we will perform NMR. The passivation is composed of two steps. The first one is the deposition by sputtering of an insulating layer. The second one the deposition of a resist layer which will permit to have a very smooth and impermeable surface. So we need to passivate the whole sample but we still need to let free place from passivation to permit us to contact our sensor. For this we also need to perform a photolithography.

The principle for the sputtering deposition is the following: plasma is formed with an inert gas. Ions from the gas are accelerated and bombard a target (here alumina) and thereby extracts target atoms that will then come and deposit on the sample. Alumina is an insulating material and to make a good deposition and avoid charge accumulation on the target surface we use an RF plasma. Once the layer is deposited, we lift-off the sample.

The last step for the passivation is the deposition of a thin resist layer, in my case SU-8-2010, since this resist is quite impermeable which is really attractive for my experiments. Indeed, as the sensor will be placed into the liquid, we need an impermeable resist. We have to notice that the passivation layer should not be too thick, otherwise the weak signal that we want to measure with our sensor will be too low.

In table 2.4 and 2.5 are presented the different parameters used for the passivation layers.

Ar Pressure	RF frequency	RF Power	Deposition time	Al_2O_3thickness
5,0.10^{-3}mbar	13MHz	200 W	2 h	200 nm

Table 2.4: Sputtering deposition parameters.

Spinner recipe	Annealing	Resist Thickness
500 rpm 5sec - 4000rpm 60sec	1min 85°C - 5min 120°C - 1 min 85°C	2 µm

Table 2.5: Su-8-2010 passivation layer parameters.

Passivation problems Even though passivation was performed on sensor, after a while, typically three weeks, sensors are no more usable. Due to a too long time in a liquid resist begins to lift off, see figure 2.21, and then creates some short circuit, see figures 2.22a and 2.22b

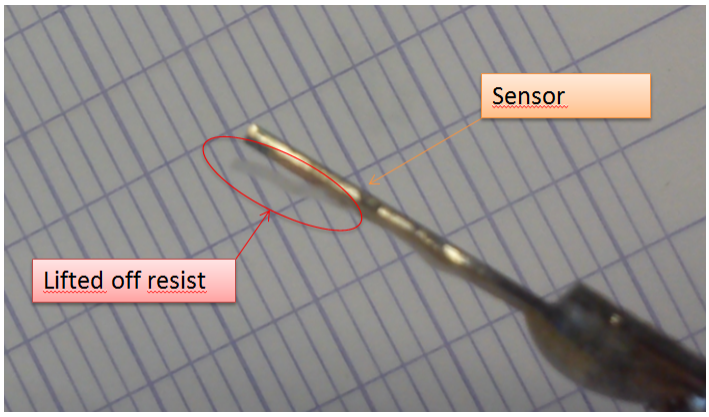

Figure 2.21: Lifted off resist on sensor.

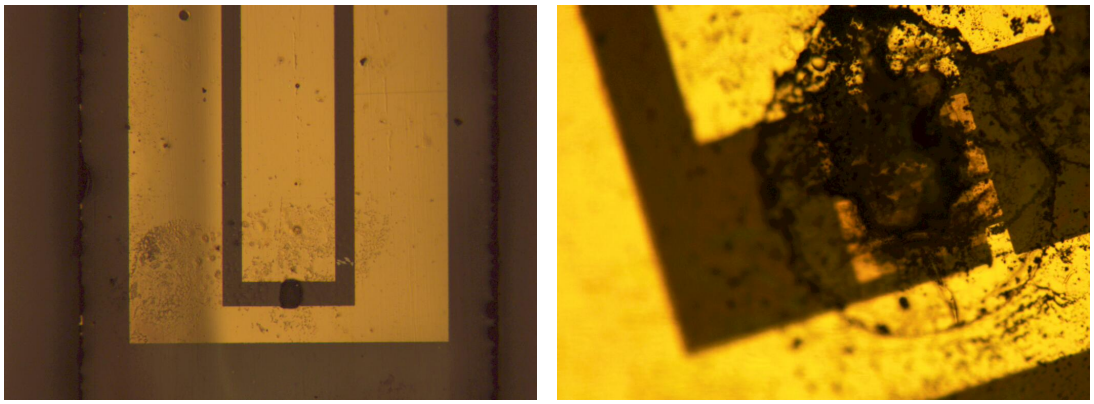

(a) Large view of the short circuit on the GMR sensor.

(b) Zoom on short circuit.

Figure 2.22: Short circuit on GMR sensors after three weeks of measurement in water and ethanol.

2.4.2 MagnetoResistance characterization

In order to underscore the MR effect, sensor is mounted on a PCB (Printed Circuit Board) via a bit of wax. Sensor is connected to the PCB thanks to 25µm diameter aluminum wires. These wires linking metal contacts of the sample to the PCB tracks are done with a ultrasonic welding machine. Once sensor is connected, it is put in a coil for a field scan. Figure 2.23 shows the full set-up to characterize the MR and the sensitivity.

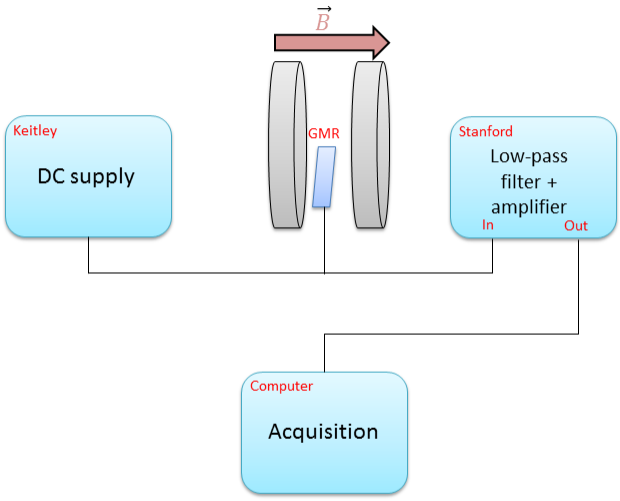

Figure 2.23: MR set-up with the DC supply for the GMR sensor. The signal is amplified and filtered by a standford. The acquisiton is made by the computer.

The sensor is supplied by DC with a Keitley current source. The Helmholtz coil, supplied by Kepco, scans the field from -150 Oe to +150 Oe and we obtain the variation of resistivity of the sensor after passing through a standford preamplifier which permits to amplify the signal and also to filter it. Indeed, the signal is noisy and to avoid the electrical 50 Hz, we filter with a low-pass filter at 30Hz. The signal is then acquired on a computer.

2.4.3 Noise characterization

2.4.3.1 Noise definition

Noise is defined as all unwanted signal limiting the understanding of an input signal. Noise level or spectral density is expressed in volt per square root hertz $\left(V/\sqrt{Hz}\right)$or Ampere per square root hertz $\left(A/\sqrt{Hz}\right)$ and corresponds to the amplitude of the fluctuations of a signal to be measured normalized in a 1Hz band.
Noise comes from several sources:

- Sources external to the device and independent of the signal, thus located outside the system.

- Sources internal to the device, which may depend on the signal

In the case of sensors, we try to characterize the internal noise of the device and for that we place the sensor under specific conditions to minimize external noise sources. Noise measurements are performed into a shielded room. Moreover noise can be classified into two types: white noise (thermal noise and shot noise) independent of frequency and noise dependent in frequency as 1 / f noise or telegraphic noise.

Johnson noise (Thermal noise) This noise is directly linked with the resistance R of the sensor. It was first observed by J.B. Johnson [10] who saw random fluctuations of voltage across electrical resistors. Later on Nyquist explained this phenomenon which takes its origin from thermal fluctuations [11]. In a material, electron of energy $E = k_b T$, adopt a disordered motion: the Brownian motion. This motion is then independent of the frequency and then it is called a white noise. In a resistance R, the noise spectral density is given in voltage by the Nyquist formula:

$$S_{V,th}^{1/2} = \sqrt{4k_b TR} \tag{2.10}$$

Thermal noise represents the fundamental limitation for the sensor.

1/f noise 1/f noise or scintillation noise is a noise whose power spectral density is inversely proportional to the frequency. We easily realize that at low frequency this noise will be predominant. Its origins are quite numerous; nevertheless in the case of conductive materials, 1/f noise is caused by fluctuations of conductivity due to trapping of charges by the defects. In 1969, Hooge [12] proposed a semi-empirical relation of the spectral density of this noise:

$$S_{V,th}^{1/2} = \frac{\gamma_H V^2}{N_C f} \tag{2.11}$$

with V the potential difference across the conductor , N_C the number of charge carriers in the material (typically with $N_C = nc.v$, nc the charge carrier density and the volume v), the frequency f and the Hooge constant γ_h. 1/f noise is very important for small magnetic structures like our sensors. We can thus define a frequency f_C: cutoff frequency. This is the frequency at which the 1/f noise starts to dominate the white noise.

Random telegraphic noise Random Telegraphic Noise (RTN) or Lorentzian noise is a phenomenon that can be explained by a random procedure carrier jumping between two level states of high and low energy with a characteristic time. This noise appears for small dimension sensors. If a sensor presents a large RTN, then it becomes quite difficult to work with it and requires an electronic treatment.

2.4.3.2 Noise measurement

Noise set-up measurement The set-up for noise measurement should be as less noisy as possible since we should be able to measure the sensor noise without the noise of the environment. The first precaution, which can easily be done is to place the sensor in a shielded place, either in a shielded room or a mu-metal box.

The environment is not the only parameter which has to be taken into account. The electronic measurement circuit also has to be considered. One of the major electronic noises is the 50Hz which comes from ac electricity networks. For that, the major parts of our measurement instruments are working on batteries.

The output signal, after being amplified by preamplifier, is then directed to a 2MHz sample rate acquisition card. The FFT is then plotted on a computer, which itself is on batteries.

Figure presents the full noise set-up measurement 2.24.

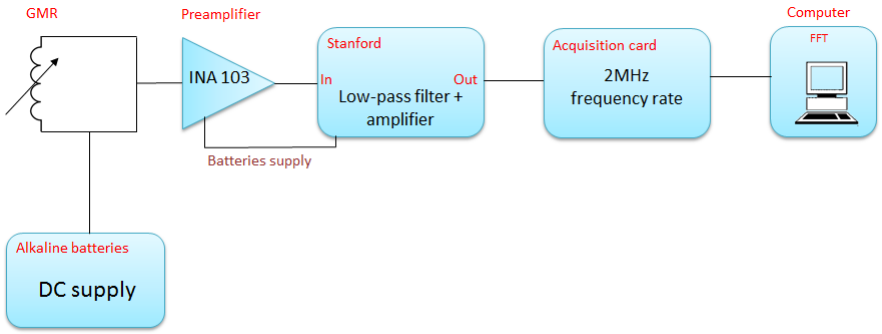

Figure 2.24: Noise set-up measurement. The signal is first amplified by a INA 103 preamplifier and then amplified again and filtered by a standford. Acquisition is made by an acquisition card and data are processed by a computer.

Noise measurement of the sensor To measure the noise of our sensor, the Wheatstone bridge configuration is chosen, see figure 2.25. As our GMR is not a fixed resistance, a variable resistance should be added to the R_2 resistance to well balance the bridge. Since it is balanced, we are sure to not saturate the preamplifier and the standford. In the coil a 300Hz signal is send and we obtain, on the GMR, a resistance variation. The output voltage is measured:

$$V_{out} = V_b \frac{\frac{\Delta R}{R}}{2\left(2 + \frac{\Delta R}{R}\right)} \tag{2.12}$$

Where ΔR is the variation of resistance of the GMR sensor.

The acquisition is made with a computer, which then plots the FFT of the raw signal. The first measurement is to verify that the chain amplification is correct. For that a first measure with a 50 Ω resistance is done. This curve should have a noise level corresponding to the thermal noise with a 50 Ω resistance. This done, we can then go forward with the sensor measurement. Without supplying it, we plot the same curve and we see that the curve corresponds to the correct thermal noise. Once these two measurements done, we know that our set-up is correct and we can supply the sensor. For different voltage we plot curves. In figure 2.26 is presented the type of curve that we obtain with different voltage into the GMR. We see that the more there is current in our sensor, the more the 1/f noise is high. Moreover, we see that at 10kHz there is a decrease in the noise. This is due to a filter to avoid any aliasing frequency. We see at 300Hz a peak which corresponds to signal detected by the sensor and other peaks at 50Hz and its harmonics due to environment. A more precise analysis will be given in part 5.3.

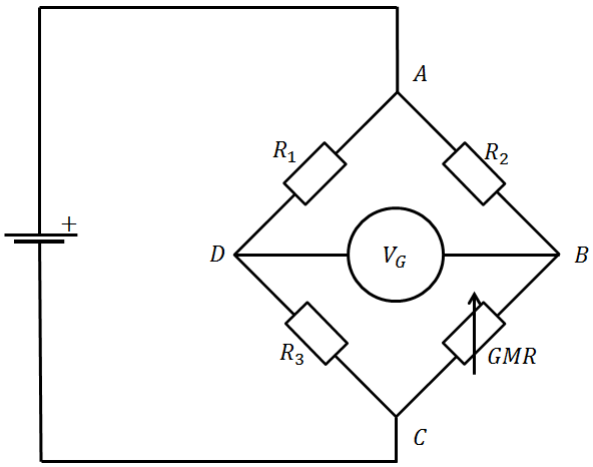

Figure 2.25: Wheatstone bridge with one of the resistance is the GMR sensor.

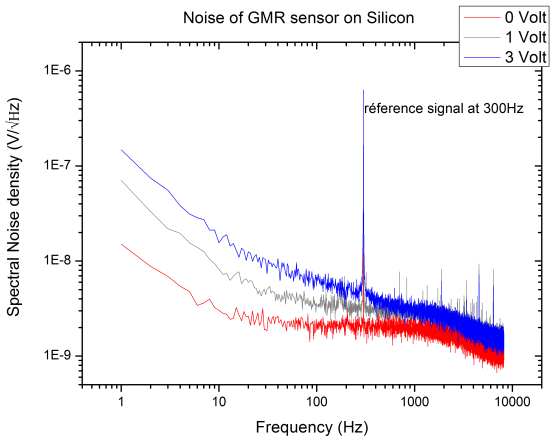

Figure 2.26: Typical GMR noise measurement curve for a meander shape supplied with three different voltages.

Conclusion

This part which is a small presentation of magnetoresistive sensors permits to have a good idea of how they work, how they are characterized in term of sensitivity and noise and how they can be used for different applications. The part concerning the effect of the external field on sensors is important since it is going to predict the behavior of our sensor while it will be placed in the magnet. Due to the presence of hysteresis in the sensor characterization, we understand that the position of the sensor in the magnet is the keystone of the problem.

Chapter 3

Experimental Set-up and Simulations

This part will permit to understand the experimental set-up established for NMR measurements. We will describe the different parts of the set-up and how the acquisitions are performed. We will see that some problems still remain but thanks to some tricks we will overcome them. A short part is also dedicated to simulations. Considering the experimental set-up and the predicted working magnetic field, we can do some simulations to estimate signals amplitudes both for a classical tuned coil and for the GMR sensors. For the magnetoresistive sensors we will consider two different configurations: the first one where the sensor is directly immersed in the sample, the second one where the sensor is over a microcapillary.

3.1 Permanent field

3.1.1 External field

- The first approach was to design a portable set-up.

In this configuration, the external magnetic field B_0, also called principal field was generated by a permanent magnet, made of neodymium, iron and boron (figure 3.1) whose magnetic field was 86,2mT. This field induces a resonance frequency of 3.67MHz for hydrogen in the NMR spectrum. The set-up is completed with adjusting screws, to place quite precisely the sample within the magnet, excitation coil and a home-made shim coil. Despite the presence of these shim coils, the field was not homogeneous enough to allow any measurement. Figure 3.2 shows the obtained signal on water after 19 000 acquisitions. The signal was obtained with a spin-echo sequence. We see a signal of 1ms long reflecting a lack of homogeneity, which is not compatible with NMRS. Indeed, field variation within the sample induces a variation in the resonance frequency. To increase the signal strength, the B_0 magnetic field also has to be increase. But there

is no simple way to increase both magnetic field and homogeneity with a portable set-up.

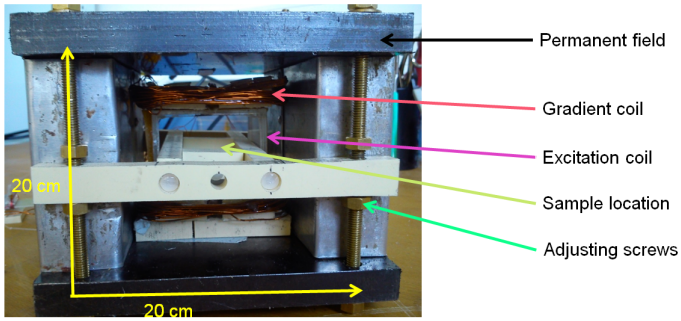

Figure 3.1: Permanent magnet with inside the presence of home-made shim coils, excitation coil, for the the placement of the GMR sensor in a sensitive state. The GMR sensor is placed into such a states thanks to adjusting screws.

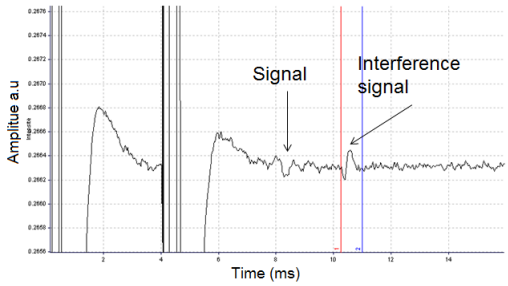

Figure 3.2: Signal of water detected by a tuned coil with the permanent magnet after 19000 acquisitions at 3.67MHz. An interference signal is present at 11ms and the NMR signal is present at 8ms. This signal is obtained with a spin-echo sequence.

- The decision to work with an electromagnet was taken in order to demonstrate that the developed set-up in functional.

For the electromagnet case, the field is created by two circular Helmholtz coils flowed by a current. To avoid a too important heating, coils are cooled down by a constant flow of water at 18°C. As we need to have a very precise field, and as we only have a gaussmeter which is not very accurate, a power resistance of 0.1Ω has been added in series with the coils. The voltage measurements at its terminals allows an accurate field measurement.

The sample is placed into the space between the two coils (fig 3.3)

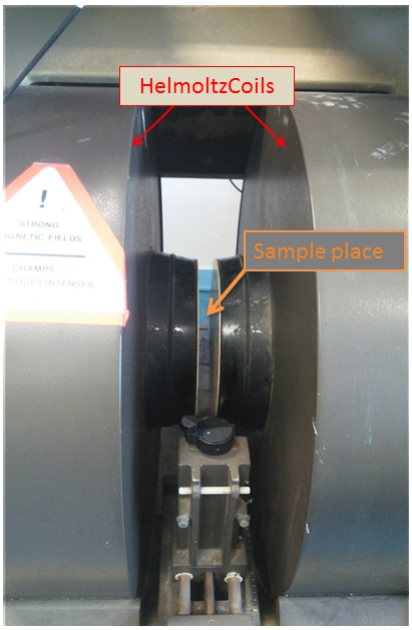

Figure 3.3: Electromagnet with sample location. The electromagnet is composed of a Helmotz coil. The sample location is in the 5cm magnet air gap.

With this kind of magnet, we are able to reach 2.2 T but for our application we will only work at a maximum of 780mT. To be able to do spectroscopy, the field needs to be as homogeneous as possible inside the sample volume.

Moreover, for long NMR acquisition, the field also needs to be stable.

3.1.2 Shim

Even if the external field is present, it also has to be homogeneous over the sample size. Shim coils are used. It consists in coils creating small magnetic fields to compensate the B_0 inhomogeneities. Figure 3.4 presents the field homogeneity without shimming. To perform this measurement, a tuned coil with water is placed into the field close to the resonance frequency. The coil is moved in depth and in height and the displacement of frequency is measured. As the shielded box is of the width of the gap of the magnet, the homogeneity in width cannot be done. Even if the field is not very stable, the frequency displacement due to field homogeneity is much higher than the one due to field stability. Finally, we see that the positioning of the sample is very crucial to work in the best conditions.

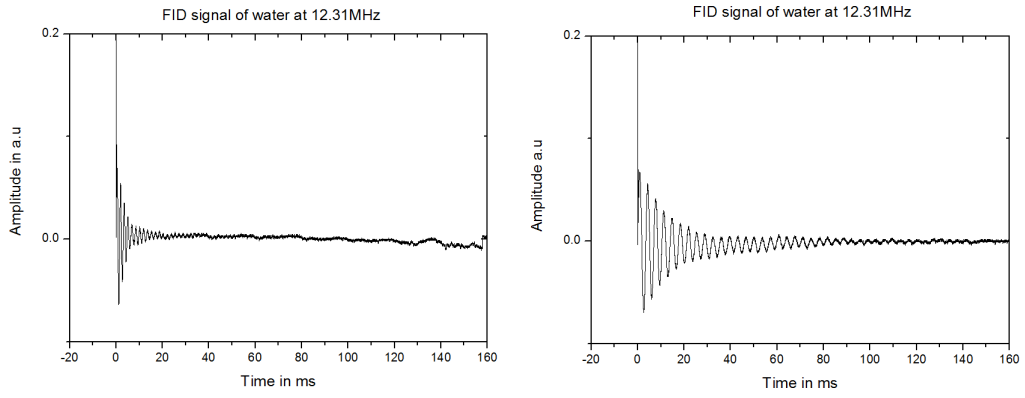

(a) (b)

Figure 3.5: FID signal of water at 12.31MHz a) without shimming and b) with optimized shimming

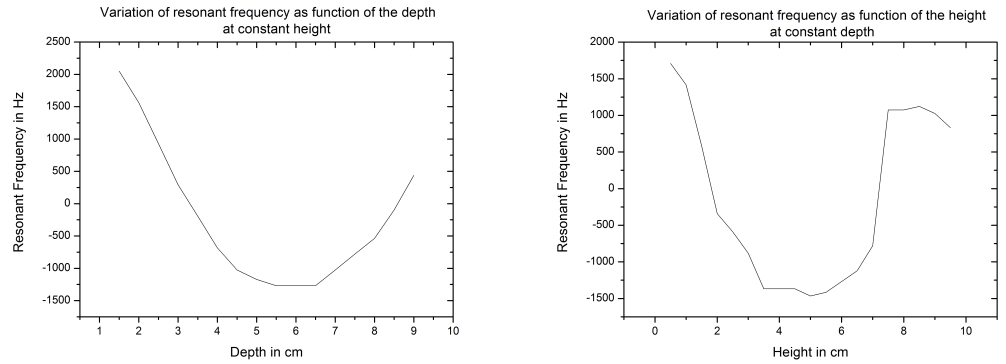

(a) Field homogeneity in width at constant height of 5cm.

(b) Field homogeneity in height at constant width of 5cm.

Figure 3.4: Field homogeneity without shimming.

In order to compensate field inhomogeneities, we have to use shim coils. These coils create a $\triangle B$ field which combines with B_0 to give a homogeneous field. In practice, there is the need of many coils to compensate the field at the first order following the three axis of space X, Y and Z. For our magnet there is also the possibility to compensate higher order terms Y^2, Y^3,Y^4, YZ, YZ^2,XY, X, XZ, $Z_{coarase}$, $Curve_{coarase}$ and $Curve_{fine}$ with knobs acting on the different shim coils.

In figure 3.5 is presented a FID with and without shimming. We clearly see that when the field is homogeneous, the apparent relaxation lasts longer, consequently the FFT peak will be narrower.

3.1.3 Field lock and stability

The permanent field is not stable over time. This drift is due to two main problems. The first one is the heating of the coils even if coils are cooled down with a flow of water. The second one is that the coils power supply is not stable. But to have a stable field the current injected into coils has to be constant. Usually, to compensate these instabilities, we use a lock mode. This mode consists in the measurement of the dispersion of the signal of deuterium ^2H, since it has a short T_1 allowing the use of rapid pulse-acquire measurement. This permits to define the compensation that has to be added. Unfortunately, for our magnet, the lock mode is not present. In figure 3.6 is presented the NMR signal of water with a tuned coil for one acquisition and for 5 acquisitions. We clearly see that due to the problem of stability, there is a loss of information.

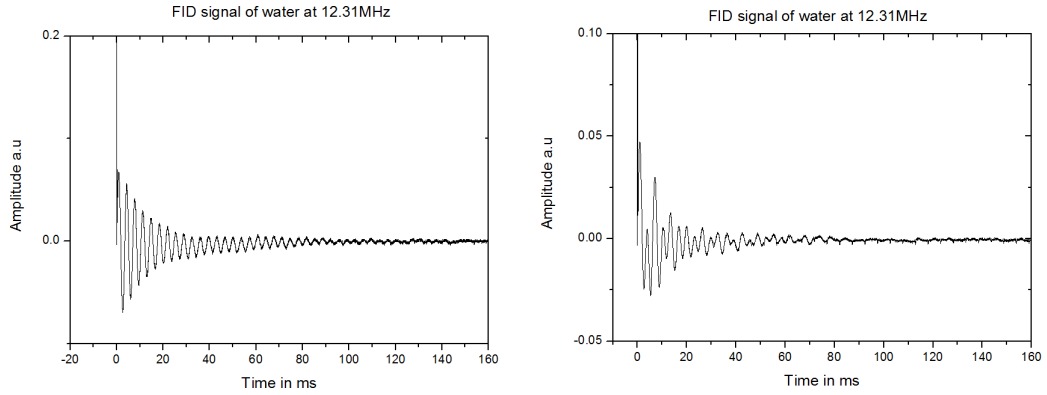

(a) (b)

Figure 3.6: NMR signal of water at 13.225MHz with a) one acquisition and b) 5 acquisitions. We see that the signal lasting for about 160ms for one acquisition is sorely reduced when there is averaging.

To overcome the problem of stability, we use the NMR tuned coil signal to lock the field. For each acquisition, the FFT of the tuned coil signal is plotted. The FFT peak is then replaced at 0Hz and is averaged with the previous peaks.

This is possible for our application, since we study simple liquids with few peaks. To work on other samples, an external lock should be added.

In conclusion, even if there is a shift in frequency, as FFT peaks are always replaced and averaged at 0Hz there is no more widening of peaks. In figure 3.7 and 3.8 are presented the way peaks are replaced and the results that we obtained with this technique.

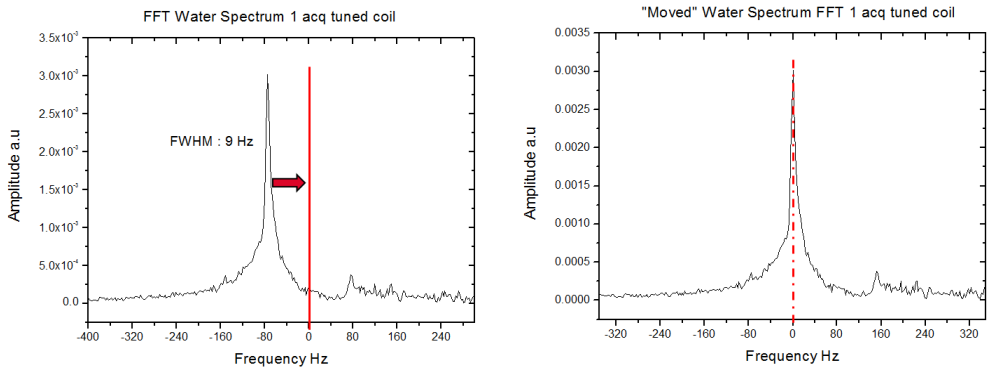

Figure 3.7: Presentation of the peak replacement. On the right the FFT is plotted and on the left, the peak is replaced in 0Hz.

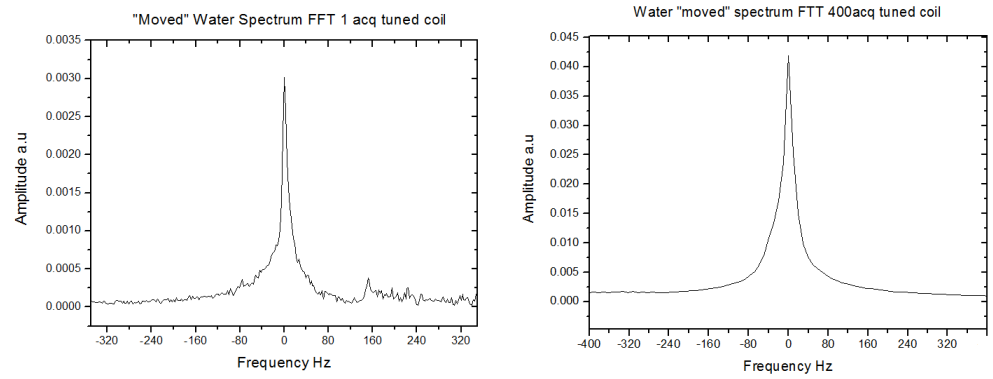

Figure 3.8: On the left the FFT with one acquisition when the peak is replaced at 0 Hz and on the left the same peak with an averaging on 400 acquisitions.

This lock system is nevertheless limited. Indeed, the spectral resolution limits the maximum resolution that can be obtained.

3.2 Excitation

Excitation is made by antenna which delivers pulses required to tilt the orientation of the magnetic moments. But we also have to take into account the electronic part allowing the generation and the amplification of the pulses.

I won't enter too much into details in this part for the generation and amplification part but I will focus more on the configuration and the tuning of the excitation coil.

One of the major consideration for the excitation is the homogeneity of the pulse over the sample. Indeed, when we work in FID configuration, if the pulse is not homogeneous, then the orientation of all magnetic moments after the pulse are not the same. This implies a decrease of the signal amplitude.

In practice, the antenna is a solenoidal coil made of a copper wire. The inductance is measured and the coil is then tuned at the resonance frequency corresponding to the applied field. As we are working at high frequency, there is the need of matching impedance of the circuit at 50 Ohms, in order to maximize the power transfer and minimize signal reflection. This coil is oriented transverse to the external field.

3.3 Reception

The reception part is the most important part. Indeed it is composed of two separate parts. As presented before, we first need a tuned coil, to make a reference for the field variation. But there is also the presence of the GMR sensor.

3.3.1 Pick-up coil

The first thing to do when we are working with pick-up coil is to tune and make the impedance matching. As seen previously, equation 1.16, a tuned coil is tuned to the Larmor frequency via this formula: $\nu_0 = \frac{1}{2\pi\sqrt{LC}}$. To tune the coil to the correct frequency, a capacitance is added in parallel to the coil. This gives the following circuit 3.9.

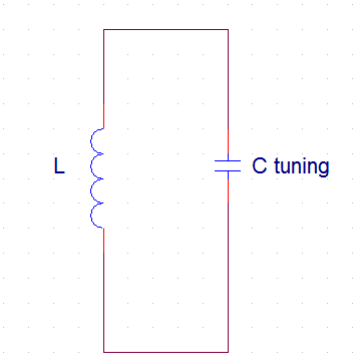

Figure 3.9: Frequency tuning of the coil by adding a capacitance in parallel to the coil.

For high frequencies and due to the fact that the signal enter into a low noise preamplifier, whose input impedance is 50 Ohms, previous circuit also has to be matched in impedance. For this, another capacitance, called the matching capacitance, is added in series [43]. The equivalent circuit is drawn figure 3.10:

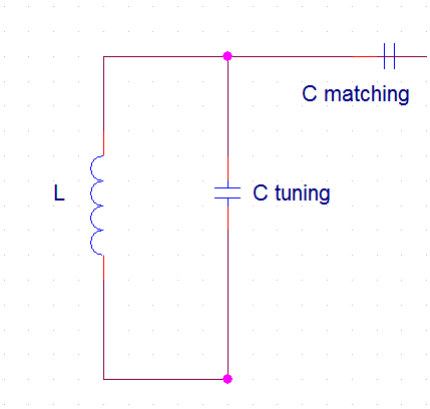

Figure 3.10: Impedance matching of the tuned coil with the addition of a capacitance in series to the LC circuit.

As the tuned coil is not only used for excitation but also for reception a band-pass filter around the resonance frequency is added. In practice, in series to the previous circuit 3.10 a low pass filter is added, giving the following circuit 3.11.

In practice, to reduce the amplitude of the pulses seen by the preamplifier the band-pass filter is cut by diodes. Indeed when diodes are conducting, each nodes become a short-circuit to the mass.

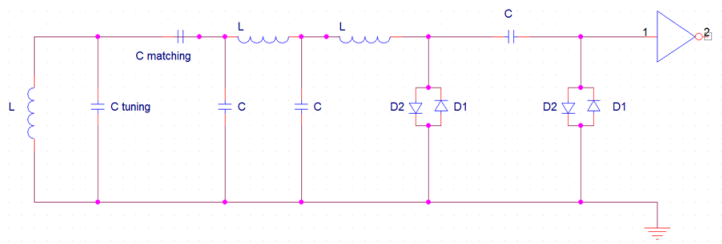

Figure 3.11: Tank circuit with the low pass-filter and the band-pass filter.

3.3.2 GMR sensor

Concerning the GMR sensor, there is no need to tune. Indeed, one of the advantages of the GMR sensors is that they can work from few Hz to GHz. In a first approach, the sensor is simply immersed into the liquid as presented in figure 3.12. Unfortunately, in this configuration a direct coupling appears between the sensor and the excitation coil. We solved this problem by modulating the GMR bias voltage at few kHz. At this level, another problem occurs which is that the frequency modulation was creating coupling in the spectrometer. Thus, just after the GMR, and before the low-noise preamplifier, a band-pass filter around the Larmor frequency is added as presented in figure 3.13.

Hence we added a low pass filter to bias the GMR with a cutting frequency at 20kHz and a high pass filter at 1MHz to detect the GMR signal around the Larmor frequency.

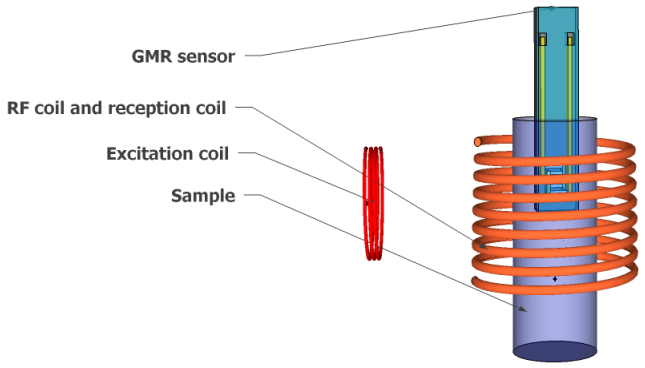

Figure 3.12: GMR immersed in the sample. The tuned coil around the sample for the lock-in and the excitation coil to position in a sensitive state the GMR into the magnetic field B_0.

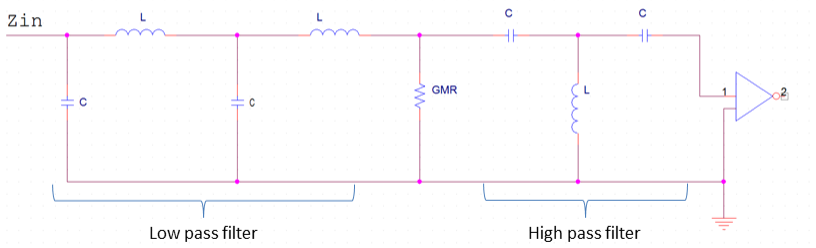

Figure 3.13: GMR filter with the presence of low pass and high pass filters, to maximise noise filtering due to the environment and the coupling coming from the modulation.

3.4 Spectrometer

The spectrometer that we use is a home made spectrometer composed of two distinct parts which are emission and reception. The emission part generates RF pulses for spin excitation. It creates pulses with a programmable amplitude, phase and duration. The reception part amplifies and demodulates the NMR signal. In this spectrometer we

have a third part, the digital part, which handles communications with the computer and creates time sequences able to realize complex pulses with various amplitudes and phases.

3.4.1 Emission

As we said, the emission part is used for the pulse generation with controlled amplitude, phase, shape, frequency and duration. All these parameters are very important since they create the B_1 field and then impact on the strength of the signal. The frequency generation is performed by a four channel commercial DDS synthesizer. Two channels are used to create the phase and quadrature frequencies for the pulse generation. It can vary from 0.1 to 100MHz with a 0.1Hz accuracy. These frequencies are first sent to a multiplexer and inverted to create 4 phases at 90°. The chosen frequency is sent to an amplitude modulator with 12 bits of accuracy, 50ns of response time and then sent to a shaper which adds an extra attenuation of 80db. A commercial 1kW RF power amplifier is used to deliver the pulses to the emitter coil.

3.4.2 Reception

The signal detected by the coil or the GMR sensor is of few MHz. The reception is a multichannel amplifier and demodulator with phase and quadrature outputs. One channel is used for the tuned coil global detection and one for the GMR local detection. A first stage very low noise preamplifier is used for each channel.

The scheme of the spectrometer is presented in figure 3.14.

Let's consider a resonance frequency of ω_0. The input signal is:

$$Acos(\omega_0 t + \varphi_0)$$

The subtraction process is carried out by a device called a mixer. Indeed, a frequency synthesizer send a frequency ω_S close to ω_0 to the mixer. At the output of the synthetizer we have:

$$Acos(\omega_0 t+\varphi_0)cos(\omega_S t+\varphi_S) = \frac{A}{2}\left[cos((\omega_0+\omega_S)t+\varphi_0+\varphi_S) + cos((\omega_0-\omega_S)t+\varphi_0-\varphi_S\right]$$

At this point we obtain two signals. One at $\omega_0 + \omega_S$ and another one at $\omega_0 - \omega_S$. With a low-pass filter the high frequency signal disappear and we keep the low frequency signal, whose digitization is possible.

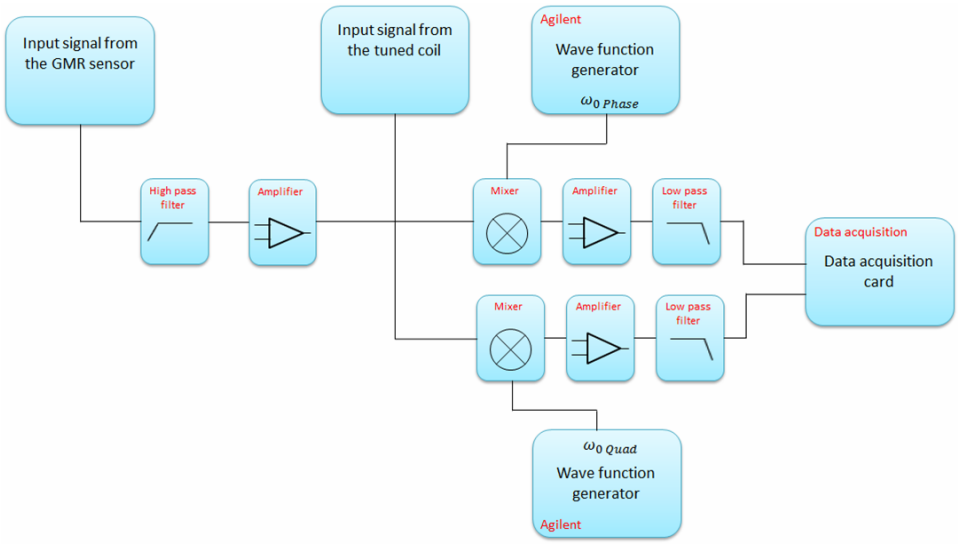

Figure 3.14: Spectrometer scheme for the acquisition channel of the tuned coil or GMR sensor. The mixer is present for demodulation, the amplifier to amplify the demodulated signal and the low pass filter to filter any remaining high frequency noise. The acquisition is made by a data acquisition card.

Moreover, we can notice that when the demodulation frequency corresponds to the resonance frequency, it gives a zero output frequency. In order to distinguish between negative and positive frequencies relative to the carrier frequency the quadrature detection must be employed. The quadrature detection is based on the same scheme of the simple detection, but here we use one more channel which is dephased by $\frac{\pi}{2}$.

After the demodulation, the signal is amplified, filtered with a low-pass filter at 10kHz and acquired with a 16 bits fast acquisition card, FFT and averaging are done by the computer.

An overall scheme of the total reception chain is presented in figure 3.15.

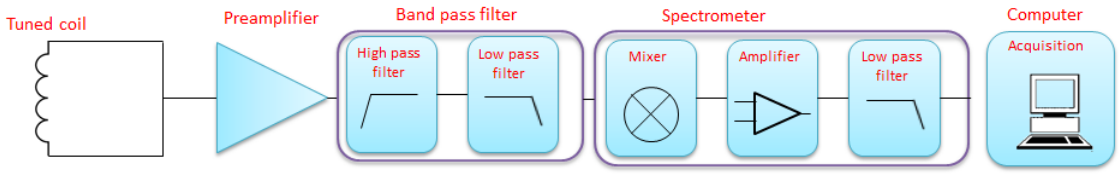

Figure 3.15: Overall scheme of the reception chain for the tuned coil channel.

The total amplification of the acquisition measured was 1100. This seems correct since we have an amplification by the preamplifier of 40dB, which represents a linear amplification of 100, and an amplification of 60dB by the demodulation part, which represents a linear amplification of 1000.

3.5 Dipolar magnetic field induction

Once the set-up is well established, we need to have an idea of the order of magnitude of the expected signal. This part presents the different simulations performed. The first experiment is the simplest experiment that can be done, where the sensor is directly immersed into the sample. This configuration enables to perform NMR spectroscopy on in-vivo samples and also to have an local information of a sample localized deep in some matter. The other simulation concerns the set-up where a microcapillary with a very few fluid volume is placed over the GMR sensor. This second configuration enables to work with very small samples which are difficult to obtain. With this configuration, we will also be able to compare the time that it takes, for a tuned coil and for a GMR sensor, to have the same SNR for a given volume.

3.5.1 Sensor immersed into a sample volume

To estimate the minimum required detectivity of a sensor to measure the signal without any averaging, we define a sample as a cube of water of 50x50x50 μm^3. We consider this sample just after a $\frac{\pi}{2}$ pulse . We decompose this sample into dipole of $1nm^3$ with a magnetic moment $\vec{m}$, calculated with the equation 1.4, aligned along the z axis. In figure 3.16 is presented the sample geometry.

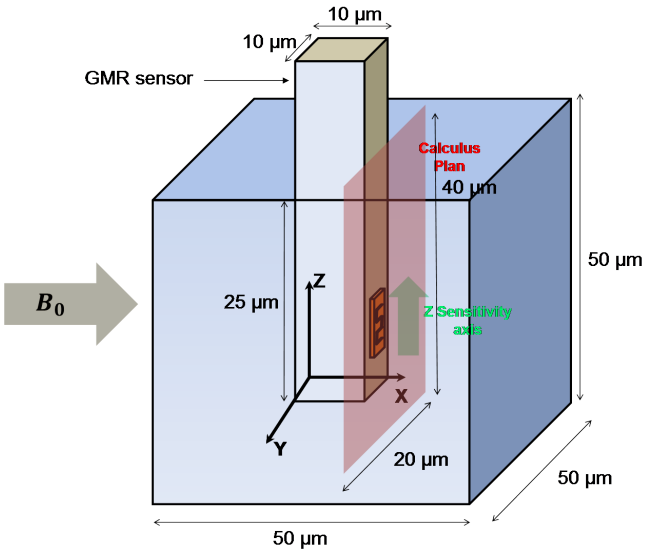

Figure 3.16: Sample geometry. In blue the sample and in orange the GMR sensor, sensitive along the Z axis. The B_0 field is applied along the Z direction.

The dipolar equation is:

$$\vec{B} = \frac{\mu_0}{4\pi}\left(\frac{3\vec{m}\cdot\vec{r}}{r^2}\vec{r} - \vec{m}\right) * \frac{1}{r^3} \tag{3.1}$$

Where $\vec{B}$ is the magnetic field generated by the moment $\vec{m}$ at the position $\vec{r}(x, y, z)$ and μ_0 is the vacuum permeability. Let's develop this expression into Cartesian coordinates :

$$\begin{pmatrix} B_x \\ B_y \\ B_z \end{pmatrix} = \frac{\mu_0}{4\pi}\begin{pmatrix} \dfrac{3\begin{pmatrix} x \\ y \\ z \end{pmatrix}\left[\begin{pmatrix} 0 \\ 0 \\ m \end{pmatrix} \bullet \begin{pmatrix} x \\ y \\ z \end{pmatrix}\right]}{(x^2+y^2+z^2)^{\frac{5}{2}}} - \dfrac{\begin{pmatrix} 0 \\ 0 \\ m \end{pmatrix}}{(x^2+y^2+z^2)^{\frac{3}{2}}} \\ \\ \end{pmatrix} \tag{3.2}$$

$$\begin{cases} B_x = & \frac{3\mu_0 mxz}{4\pi(x^2+y^2+z^2)^{\frac{5}{2}}} \\ B_y = & \frac{3\mu_0 ymz}{4\pi(x^2+y^2+z^2)^{\frac{5}{2}}} \\ B_z = & \frac{3\mu_0 m}{4\pi(x^2+y^2+z^2)^{\frac{3}{2}}}\left(\frac{3z^2}{(x^2+y^2+z^2)^{\frac{3}{e}}} - 1\right) \end{cases}$$

As our magnetic sensors are sensitive only along the z direction, we only consider the B_z component. We choose a sensor whose size is 10µm by 10µm placed in the middle of the xy plane in a magnetic field B_0 of 300mT. In this configuration, we can plot the magnetic field $B_z$obtained along the x direction, at the position y which corresponds the middle of the sensor (figure 3.17). We can then estimate that the signal created is around 15pT at 5µm far from the sensor.

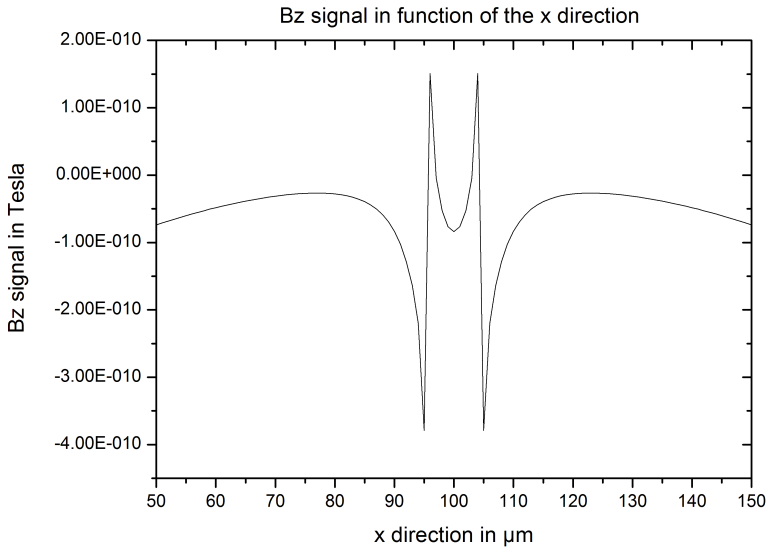

Figure 3.17: $B_z(T)$ in function of the x direction.

We can see that the dissymetry induced by the sensor into the cube of water creates a non 0 field around the sensor. Very close to the sensor, we see that we have a signal that can be measured. But to see what amount of fluid around the sensor participate in the creation of this B_z field, we have calculated for different sphere of water around the sensor the B_z field created. Graph 3.18 is obtained:

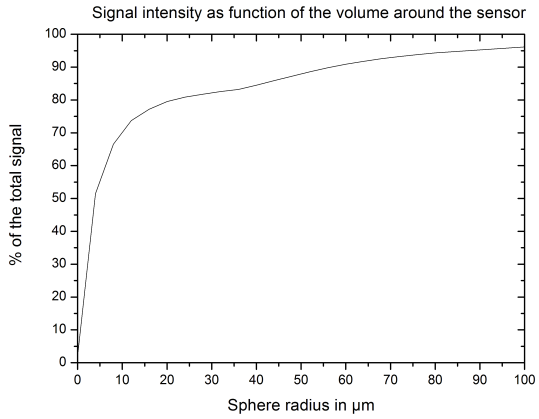

Figure 3.18: Influence of the environment on the signal seen by the sensor.

We can deduce that the part of fluid contributing the most to the signal is a sphere around the sensor of 20µm of radius. Indeed we see that a sphere of 20µm of radius is enough to have 80% of our total signal.

Nevertheless, decomposing the sample into dipole of $1nm^3$ is not exact. Indeed, the number of proton H inside $1\text{n}m^3$ is:

$$N = 2N_A \frac{M_{1\mu m^3}}{M_{H_2O}} = 67$$

where $M_{1\mu m^3}$ is the weight of $1\text{n}m^3$ of water, and M_{H_2O} the molecular mass of water. Table 3.1 represents the difference of simulated signal, at 5µm far from the sensor at the B_0 field of 100mT, as function of the number of dipole that we take into account.

Number of dipoles in $1\mu m^3$	Signal in T	Relative difference	Calculation duration
8.10^6	$7,16.10^{-11}$	0	1-2 minutes
$8,4.10^7$	$7,84.10^{-11}$	9,0%	2-4 minutes
$5,1.10^8$	$8,18.10^{-11}$	13,2%	4-5 minutes
$4,1.10^9$	$8,36.10^{-11}$	15,3%	45-50 minutes
$6,7.10^{10}$	$8,47.10^{-11}$	16,7%	4 hours

Table 3.1: B_z signal strength evolution as function of the dipole number in $1\mu m^3$ of water. The table also presents the relative difference made while the number of dipole increases its the calculation time.

In conclusion we see that the obtained simulated signal with 8.10^6 dipoles is not too far from the signal that we will obtain if we take into account all dipoles. Moreover we see a huge difference in the calculation time. In order to reduce time calculation and to have have a good order of magnitude of the "real" signal we work with 5.10^8 dipoles per μm^3.

3.5.2 Sensor over a cylinder

The ideal set-up would be to design a microfluidic system where the GMR would be placed over a microcapillary making possible NMR spectroscopy on very few fluid volume. So let's consider this configuration, where the sensor is placed over a microcapillary such as figure 3.19.

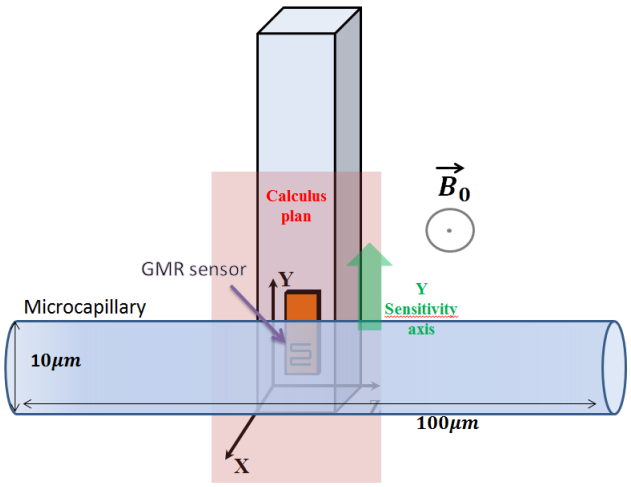

Figure 3.19: GMR sensor over a microcapillary and the B_0 field perpendicular to the microcapillary. The GMR sensor is sensitive along the Y axis.

If we consider a cylinder of 100µm long and 10µm of diameter, the B_0 field of 300 mT is perpendicular to the capillary and the sensor is sensitive along the Y direction. We saw previously that the sensor needs to be very close to the sample to be able to detect a moderate signal. Here we decided to put the GMR 1µm far from the capillary. Considering this geometry, figure 3.20, we have the following order of magnitude of field detected by the sensor.

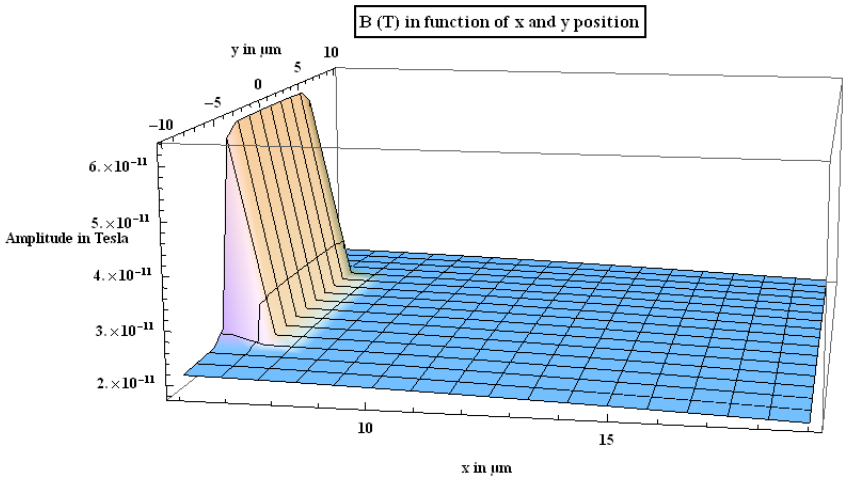

Figure 3.20: Order of magnitude the signal detected by a GMR sensor 1µm far from a capillary.

We see that to obtain the maximum of signal, the sensor should be centered above the capillary and as close as possible of the surface. In practice, a thin capillary is chosen and our GMR sensor is placed very close to capillary.

3.5.3 Signal-to-Noise Ratio

3.5.3.1 Tuned coil

Let's estimate the signal to noise ratio that we have on a tuned coil in order to have an idea of the needed number of acquisition. We consider the configuration where the sample is placed into the tuned coil and the GMR sensor immersed into the sample. We rely on the formula 1.32. To be as close as possible to our set-up, we take a coil volume of $1,2.10^{-6}m^3$ and the sample size is changed in order to change the filling factor.

We then see the the evolution of the SNR as function of the filling factor for both the tuned coil and the GMR sensor for a B_0 field of 100mT, see graph 3.21. Here we have considered a sample of pure water.

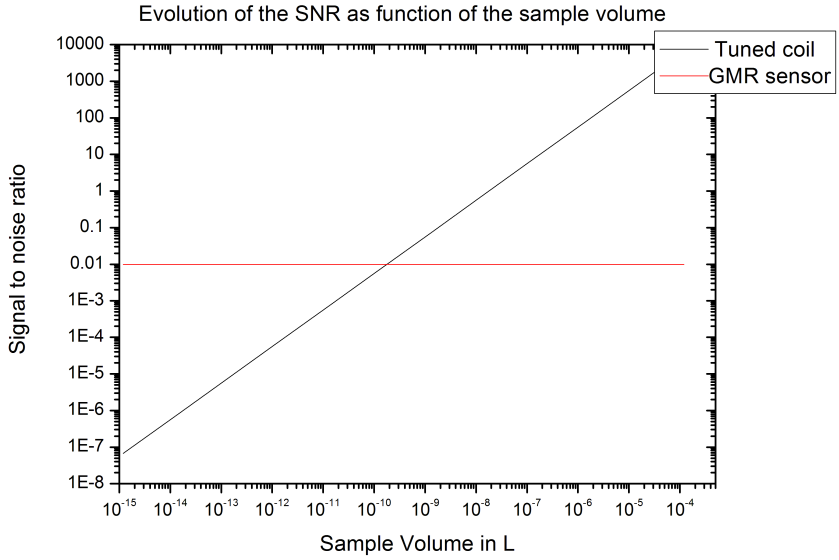

Figure 3.21: Evolution of the SNR as function of the sample volume for both tuned coil with a fixed size of $1,2.10^{-6}m^3$ and GMR sensor at a B_0 field of 100mT.

This graph enables to understand that the tuned coil is the best sensor for NMR applications when the filling factor is high. But as the sample size is decreased, there is a critical size where the GMR sensor become more competitive than the tuned coil. Indeed for sample volumes of few nL the GMR sensor is more sensitive than the tuned coil. This is due to the fact that the tuned coil does not match the sample size.

If we make one acquisition per seconds it will take $2,23.10^{15}seconds$, which represents about 7.10^7years, for a coil of $1.2cm^3$, to obtain a SNR of 10 for a sample size of $1.1\mu m^3(1,1.10^{-3}pL)$. To work with this sample size, the GMR will be preferred.

3.5.3.2 GMR sensor

Let's do the same thing on the point of view of GMR sensors. To do so, we need to know the behavior of the sensor while it is placed into the field. As the magnetoresistance curve shows us that the sensor is not centered and also present a big hysteresis, we have to use the field a bias magnet and also to perform the sensitivity measurement in-situ as presented in part 3.2.

For that we designed a coil that will be placed into the shield box, as presented on figure 3.22. The coil placed approximately $2cm$ far from the sensor. We calibrate it with a gaussmeter. The coil is supplied with a Keitley at 30Hz with a current of $105mA$. We measured a signal of the coil of: $165nT$.

To evaluate the sensitivity of the sensor into the field , we consider a sensor whose sensitivity is around 8% as seen in part 3.3.2.1. The sensor is supplied with 5V which gives a sensitivity of $45mV/mT$. The coil signal detected by the sensor should then be 8.25µV. But with the oscilloscope we have a signal of 6.4µV. We deduce that the sensor sensitivity into a field of $0.3T$ is of 7%.

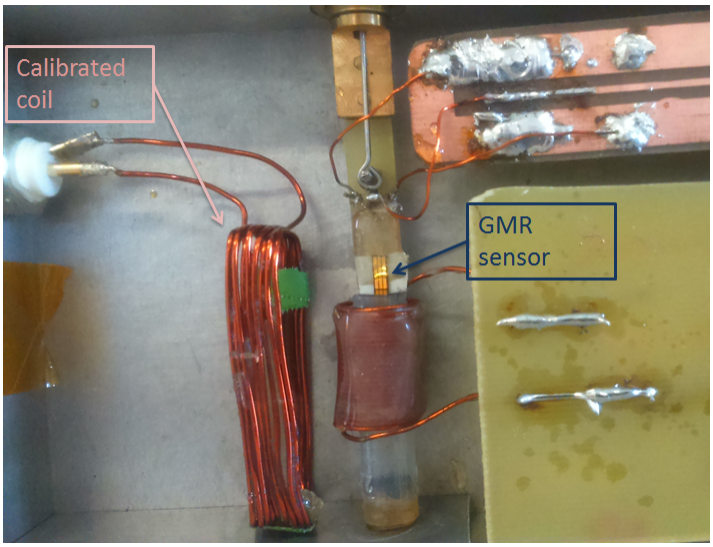

Figure 3.22: Sensitivity test coil and the sensor into the excitation and reception coil.

Now that we have an order of idea of the sensor sensitivity into the field, we can estimate the number of needed acquisition to obtain a good SNR. The signal that we try to measure is of the order of $15pT$ at 0.3T. As the sensor sensitivity is 7%. Considering the sensor noise of $5nV/\sqrt{Hz}$, as seen in part 3.3.2.2. To have a SNR of 2 we have to perform 360 acquisitions.

Conclusion

With this chapter we noticed that the set-up is a conventional set-up for NMR excepted that we use a trick to have a "field stability" for averaging. Moreover, the use of GMR sensors can allow to work with a small volume of fluid. Indeed, we can easily adjust the size of the GMR sensor to fit the sample size and geometry. We saw that for a small sample volume, GMR can be very competitive to conventional tuned coils. Effectively, in the first chapter we understood that decreasing the size of the tuned coils under 100µm of diameter represents a true challenge but this is not the case GMR sensors.

Chapter 4

Magnetoresistive sensors characterization

In this chapter, the sensors deposited on different substrates are compared according to the characterization methods presented in chapter 3. First we will study the response of each sensor in terms of magnetoresistance, noise and sensitivity. As sensors will be immersed into a magnetic field, we will then investigate the response of the sensors while a magnetic field is applied perpendicularly. Finally, as the NMR signal is around few MHz, we will also investigate the response of the sensors as function of the frequency.

4.1 Sensors shape and stack

The sensor shape is of a huge importance. As discussed in 2.2.2, a good shape leads to a linear sensitivity around zero magnetic field and to a relatively low noise. For our application the meander shape was chosen since it provides a high resistivity to be able to handle a high voltage in order to have a high sensitivity. Meander are short-circuited at the sides to avoid additional magnetic noise. Three different widths of meanders width were designed: 15µm, 5µm and 3µm in order to be able to have three different sizes of samples. Considering a typical resistivity of 12Ω/□ we can estimate the resistance and the maximum input voltage allowed of each sensor with the following table:

Line width in µm	15	5	3
Line length in µm	150	70	30
Number of lines	9	6	5
Maximum Voltage in V	15	5	1.8
Estimated Resistance in Ω	2000	1000	600

In figure 4.1 is presented the layout design of the meander for the lithographic process. The maximal current for a safe generator is 1mA/µm width. The higher the maximum voltage is, the higher the sensitivity of the sensor will be.

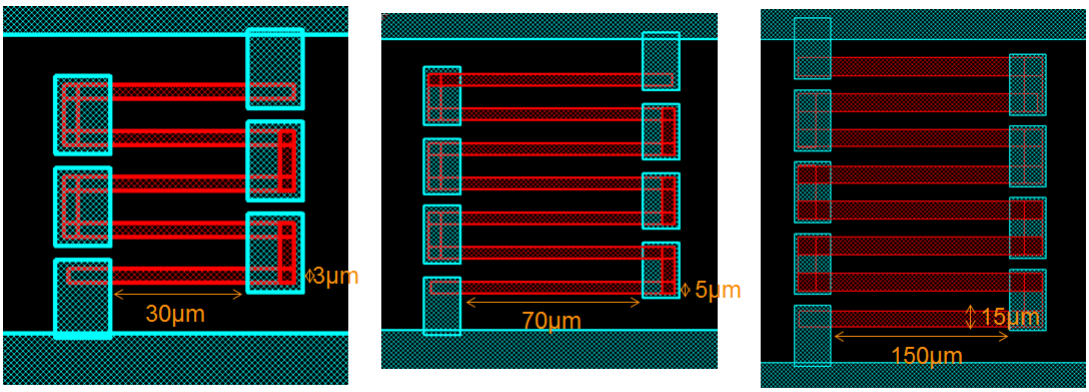

Figure 4.1: Schema of the three GMR meander designs. In red: GMR meanders and in blue the contacts.

The stack used for the NMR application is a typical GMR spin valve deposited on a silicon substrate. The composition of the GMR stack is:

$$Ru_{1nm}/PtMn_{18nm}/CoFe_{2nm}/Ru_{0.85nm}/CoFe_{2.1nm}/Cu_{2.5nm}/CoFe_{1nm}/NiFe_{3.5nm}/Ru_{0.4nm}/Ta_{5nm}$$

The sensor is designed following the process described in section 3.3.1.

For the first NMR application, that means where the sensor is placed into the liquid, the device needs to have a needle shape. As several sensors were processed on the same wafer, to separate them we have to add a cutting step. For that, a diamond saw was used. The principle is a rotating diamond disk which goes through the sample and with the rotation of the disk cuts it. To avoid too much heating of the sample and also to keep the disk safe, a constant net water flows over the disk. To prevent the sample from any corrosion and pollution, a protective resist is spinned on it. This resist layer is removed by a simple lift-off with acetone. This diamond saw ensures a cutting width of a few hundred of µm. The final device is presented figure 4.2.

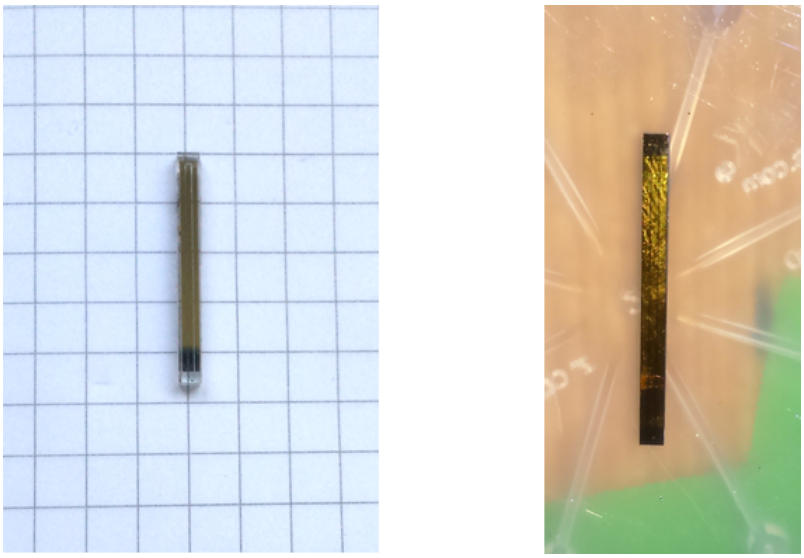

Figure 4.2: Bar shape of the GMR sensor with on the right GMR on glass and on the left GMR on silicon. The GMR on glass is thicker than the GMR on silicon.

For a reason discussed in section 5.5, GMR on alumina and GMR on glass and alumina were preferred to GMR on silicon. The GMR stack is then:

$$Ta_{5nm}/NiFe_{3.5nm}/CoFe_{1.2nm}/Cu_{2.9nm}/CoFe_{2.5nm}/IrMn_{10nm}/Ta_{10nm}$$

The main difference between GMR on silicon substrate, GMR on glass substrate and GMR on alumina substrate comes from the thickness of the substrate: 700µm for silicon, 3mm for glass and 300µm for alumina.

4.2 Magnetoresistance characterization

Sensors that we used were first deposited on silicon with the stack presented above. Due to coupling effect through silicon at high frequencies, explained in 5.5, we decided to work on other substrates such as glass and alumina. This part shows the different magnetoresistance curves for each substrate for a sensor with a 5µm width, with the set-up described in part 2.3.2.

- GMR on silicon

The choice of silicon substrate sensor was first adopted since it is the most common substrate and the fabrication process is well established and mastered. Figure 4.3 shows the magnetoresistance curve of the sensor. We see that the magnetoresistance is relatively good since it is 6.9%. This sensor presents an hysteresis of 8.7 Oe and it is centered around 5.3Oe. The in-plane residual component of the B_0 external magnetic

field was used to reduce the hysteresis and to shift the center to zero Oe. By changing the sensor orientation, we reach the right direction of bias magnetization, as presented in part 2.2, allowing the sensor to be functional. Moreover, we see the sensitive part of the curve is quite straight which allows us to have a good sensitivity with the proper bias field.

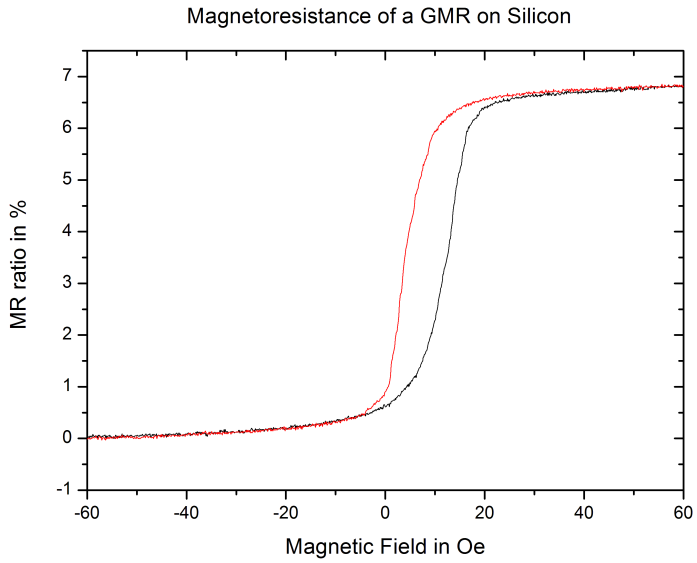

Figure 4.3: Magnetoresistance curve of GMR sensor on silicon

- GMR on glass

The major difference between GMR on glass and GMR on silicon is the substrate thickness. Indeed the silicon substrate was 700µm thick whereas the glass substrate is 3mm thick. Figure 4.4 shows the magnetoresistance curve of the sensor on glass. We see that the magnetoresistance is higher than for the sensor on silicon. Indeed, here the magnetoresistance is of 9.1%. As previously, the sensor presents an hysteresis of 1.65Oe and is centered around 0Oe. We can also notice that the sensitive part of the curve is straight. The absence of synthetic antiferromagnetic (SAF) layer, may lead to an easier reversal of the direction magnetization of the hard layer into the field. We can conclude that although they present a high magnetoresistance, these types of sensors won't be the ideal candidate for our application, as presented in section 5.4.

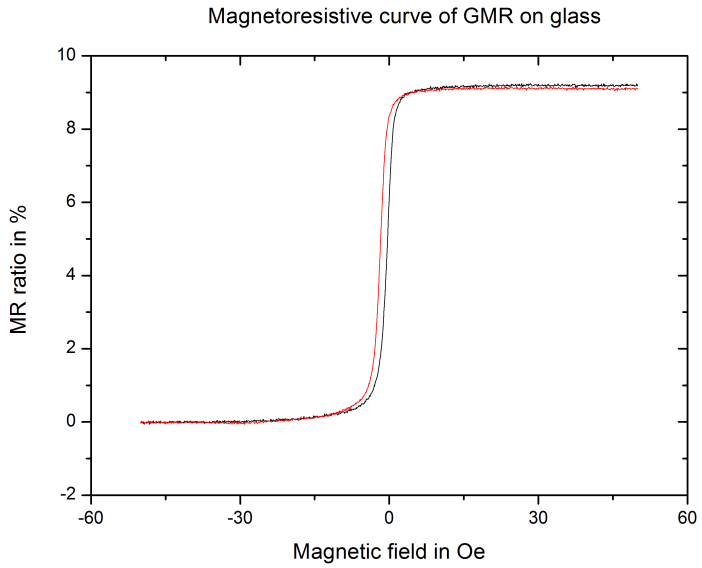

Figure 4.4: Magnetoresistance curve of a GMR sensor on glass

- GMR on alumina

Another type of substrate that we used is alumina. Figure 4.5 shows the magnetoresistance curve of the sensor. We see that the magnetoresistance is lower than the two others. Here the magnetoresistance is of 5.5%. Nevertheless, this sensor present the advantage to have a small hysteresis of 2Oe, so we won't need to apply a high magnetic bias. Moreover, we see that the sensitive part of the curve is relatively straight. The only drawback is that the sensor is centered around -14Oe, but this can be easily adjusted with the external magnetic field.

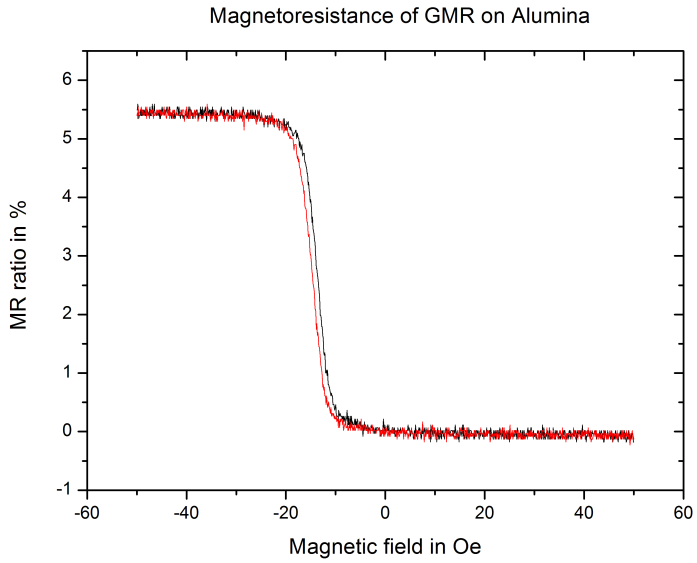

Figure 4.5: Magnetoresistance curve of a GMR sensor on alumina

Discussion Let's first discuss about the magnetoresistance obtained with the three different sensors. Besides the fact that they are composed of different stacks, the reason of the variation of magnetoresistance can be explained by the use of different substrate. Indeed, as explained by *Kano and al.* [64], the improvement in the sharpness of interface leads to an increase of the magnetoresistance. Here we see that the maximum of magnetoresistance is obtained with the device on glass. Indeed the glass has a smooth surface whereas alumina and silicon oxide have a rougher surface.

From the physical point of view, the presence of an hysteresis means that the internal magnetization pattern of the material does not depend on instantaneous applied magnetic field, but is a combined effect with magnetization history. The origin of the hysteresis is various. It can come from the sensor shape. For small size samples, the shape anisotropy allows having a more linear and hysteresis free behavior. But here for a same sensor shape we have different behaviors. But we also have to take into account the fact that the grain boundary diffusion of Cu layer into the magnetic layers can lead to a decoupling of the grains, leading to an enhancement of the coercivity [62]. A last point that can also explain the difference of coercivity, as detailed by *Liu and al.* [63], is the thickness of the free layer of NiFe. There is a optimal thickness of the NiFe layer in bilayer NiFe/CoFe to have a minimum of coercivity. This is explained by the grain size of the bilayer. The grain size depends on the roughness of the the initial surface roughness.

In absence of the hysteresis effect, and taking into account the magnetoresistance, it gives us an idea of the maximum of sensitivity that we can have with each sensors: 6.65%/mT for GMR on silicon, 9.3%/mT for GMR on glass and 5.01%/mT for GMR

on alumina.

4.3 Noise characterization

As for magnetoresistance characterizations, we performed noise characterizations on each substrate of the same width size 5µm. This part shows the different noise curves for each substrate, following the set-up explained in part 2.3.3. At high frequencies, the low frequency noise can be neglected and the only contributing noise is the thermal noise. However such measurements give an overview of the GMR quality and may be of importance for very low field NMR.

- GMR on silicon

Figure 4.6 shows the noise curve of the sensor on silicon. We see the $\frac{1}{f}$ noise at low frequencies and rapidly, around 100Hz, we are in the white noise region. Even when the voltage is increased the sensor noise is in the white noise at our working frequency.

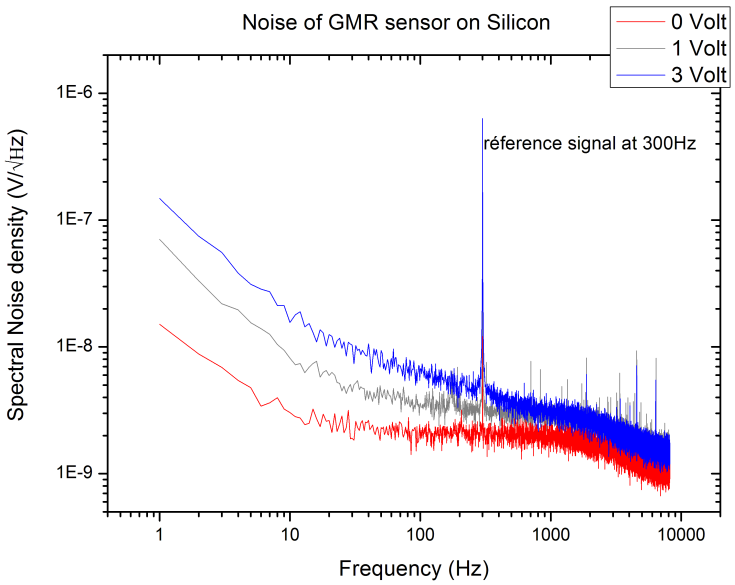

Figure 4.6: Noise curves of a GMR sensor on silicon for three different voltage supply.

- GMR on glass

Figure 4.7 shows the noise curve of the sensor on glass. At low frequencies, we can notice that this type of sensor presents much more $\frac{1}{f}$ noise. The presence of many peaks on the graph is a signature of RTN (random telegraph noise) due presumably to a lower GMR processing quality.

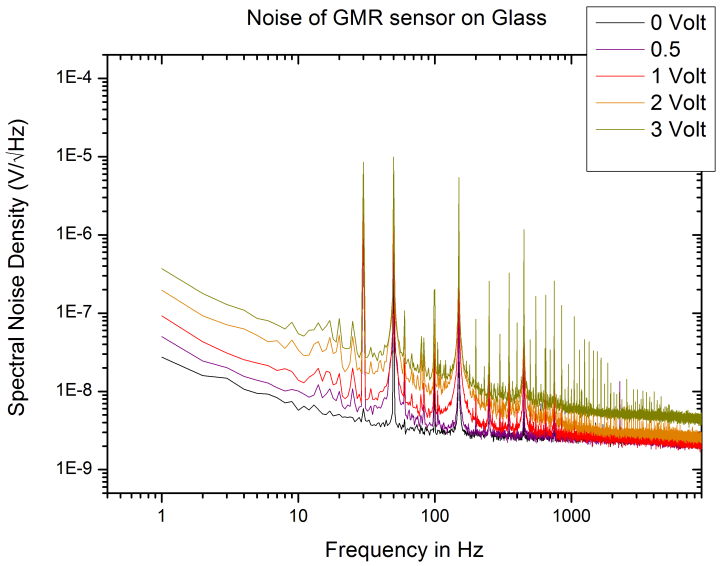

Figure 4.7: Noise curves of a GMR sensor on glass for 5 different voltage supply.

- GMR on alumina

Figure 4.8 shows the noise curve of the sensor on alumina.As for silicon and glass substrate, GMR on alumina substrate presents a $\frac{1}{f}$ noise at low frequencies and a white noise in the frequencies of interest range. The noise is again larger than the noise of GMR of silicon.

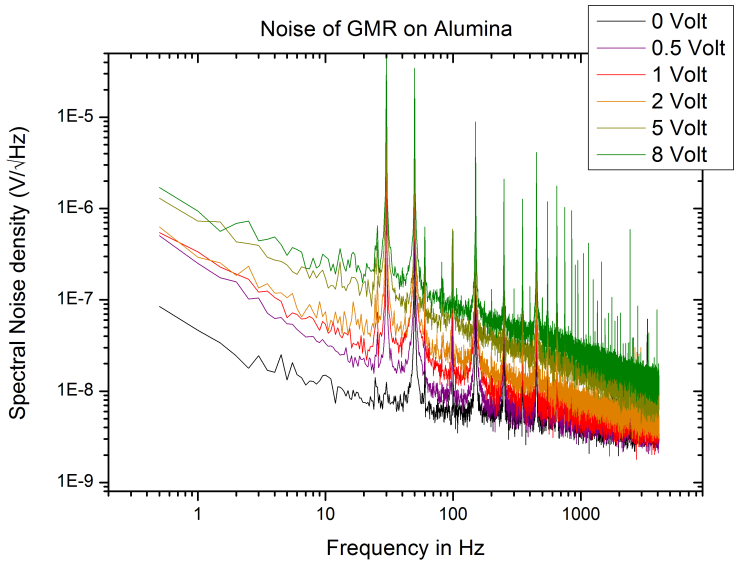

Figure 4.8: Noise curves of a GMR sensor on alumina for six different voltage supply

Discussion We see that on each curves we have a thermal noise of 2.4 $nV/H^{1/2}$ for GMR on silicon, $3.4nV/H^{1/2}$ and $3.2nV/H^{1/2}$ for GMR on alumina. This is in agreement with the theoretic thermal noise. Indeed, the resistance of the sensor on silicon is 500Ω, leading to a theoretical noise of $2.8nV/H^{1/2}$. The resistance of the sensor on glass is 920Ω, leading to a theoretical noise of $3.9nV/H^{1/2}$. And the resistance of the sensor on glass is 1005Ω, leading to a theoretical noise of $4.0nV/H^{1/2}$. The difference of measured resistances comes from the different sensor sizes, the process which is not perfect and also from the stacks used which are different. We also notice that the measured thermal noise is higher than the theory since in the theory we do not take into account the noise coming from the preamplifier.

Another point that can be discussed here is the fact that there is some RTN noise on devices on glass and alumina. As this noise is mainly due to the formation of domain walls and thus the apparition of energetic configurations in the free layer, we can explain it by the fact that there is some deterioration of the free layer maybe because the satck were older.

4.4 Sensitivity as function of the external field B_0

As the GMR is in-plane sensitive, the external field should be applied perpendicular to the sensor as presented in figure 4.9. As shown in part 3.2.1, by applying a field perpendicular to the GMR and by playing a bit on the sensor's orientation, we can adjust the sensitivity.

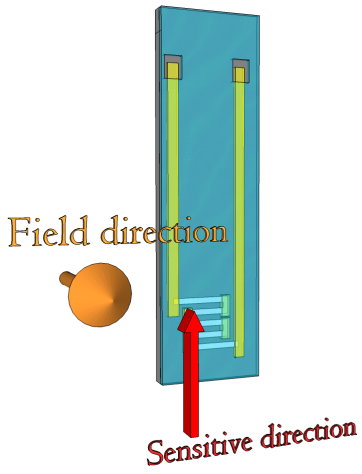

Figure 4.9: Sensitivity direction and B_0 magnetic field direction.

As the working field for our application goes up to 0.8T, the external field needs to be very perpendicular to the GMR. Indeed if the field is not perfectly perpendicular, the residual in plane component of the field saturates the sensor. For our sensor this component should be lower than 1mT. So the alignment of the GMR into the field is a crucial point. To adjust the sensor as precisely as possible a two dimensions home-made control system, presented figure 4.10, was fabricated. It is composed of a stem allowing the θ rotation. As we also need to control the angle between the GMR and the vertical, another stem is present. This one, via a screw system, will push or pull the PCB and then rotate by a small angle the sensor. We have to notice that here, everything is nonmagnetic.

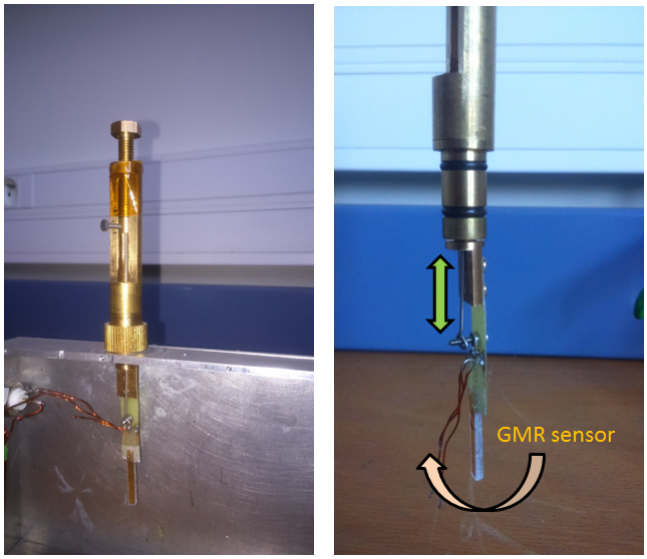

(a) (b)

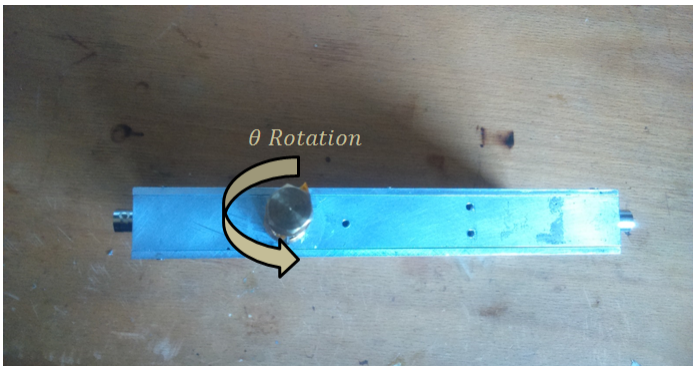

(c)

Figure 4.10: Control system to adjust the GMR into the B_0 external field. a) Global view of the control system b) Side view of the system with a glass GMR sensor mounted on c) Top view of the system.

Once this control system is linked to the rest of the set-up, we can plot the variation of sensitivity as function of the external field for each sensor. The result for the sensor on silicon is presented on figure 4.11, for the sensor on alumina is presented on figure 4.15 and for the sensor on glass is presented on figure 4.13.

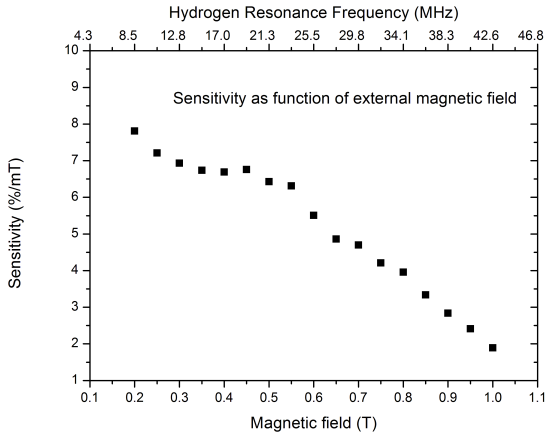

Figure 4.11: Evolution of the sensitivity as function of an applied external field perpendicular to the GMR plane for silicon substrate.

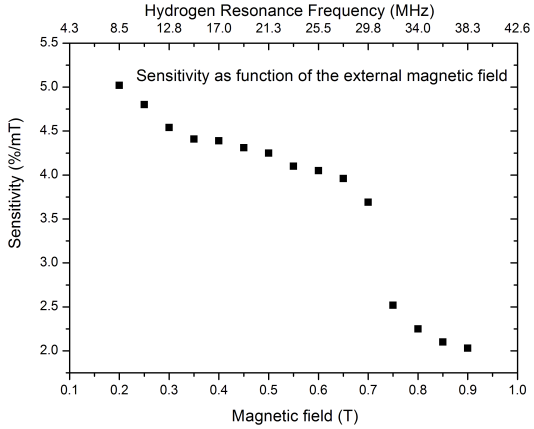

Figure 4.12: Evolution of the sensitivity as function of an applied external field perpendicular to the GMR plane for alumina substrate.

From these graphs we can easily see that in presence of a perpendicular field, the sensitivity of the GMR decreases as the field increases. This is due to the fact that the magnetization layer of the GMR, which is initially in-plane tends to rotate out of plane, inducing a reduction of the MR effect, due to dipolar anisotropy. This reduction varies as function of the cosinus. And we saw in section 2.3.2.3, that for a thin layer of NiFe, the demagnetizing field was around 1T. This explanation seems to agree with our results which explicate that at 1T we have almost lost all the sensitivity of the sensor on silicon and on glass.

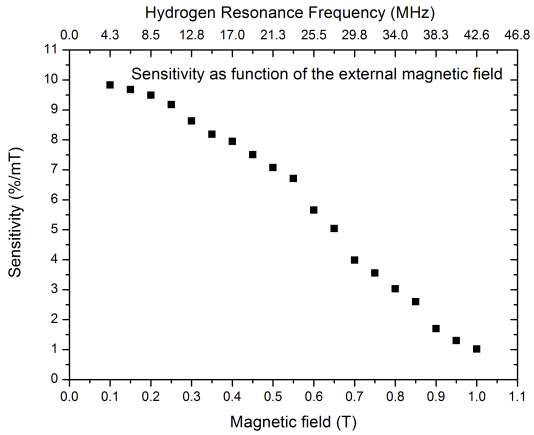

Figure 4.13: Evolution of the sensitivity as function of an applied external field perpendicular to the GMR plane for glass substrate.

Concerning GMR on alumina, we can first observe the same behavior as previously, which is a reduction of sensitivity varying as function of a cosinus. Then around 0.7T, there is a huge loss of sensitivity. This is due to the absence of SAF in the hard layer of the stack. The hard layer begins to reverse.

We can define the figure of merit of detection as the magnitude of the detected signal which is the product of the NMR signal, proportional to the field, and of the sensitivity of the sensor for a given geometry. Figure 4.14 gives that figure of merit as function of the external field for the sensor on silicon, figure 4.15 for the sensor on alumina and figure 4.16 for the sensor on glass.

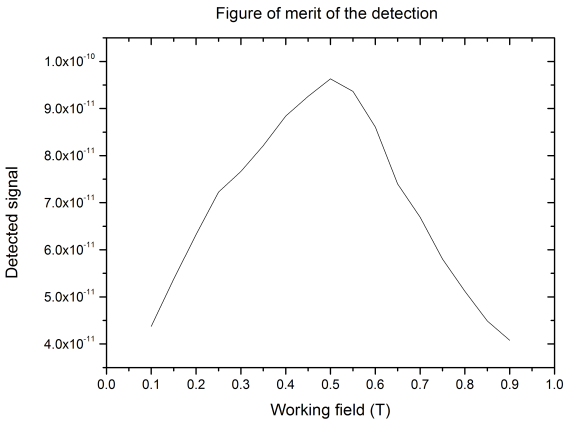

Figure 4.14: Evolution of the detected signal as function of an applied external magnetic field perpendicular to the GMR plane for sensor on silicon.

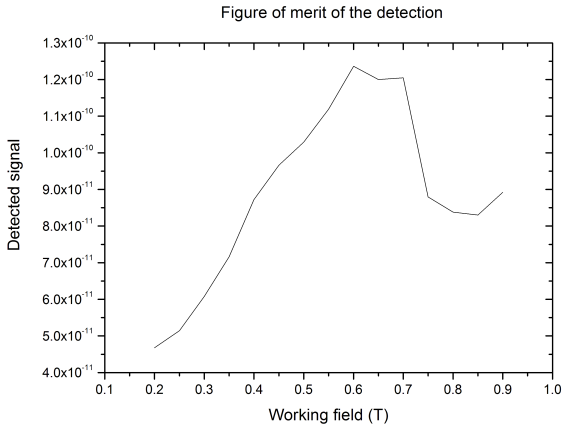

Figure 4.15: Evolution of the detected signal as function of an applied external field perpendicular to the GMR plane for sensor on alumina.

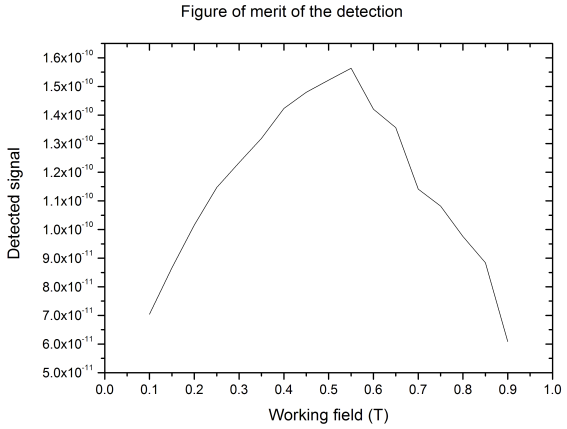

Figure 4.16: Evolution of the detected signal as function of an applied external field perpendicular to the GMR plane for sensor on glass.

This factor of merit may incorporate also the fact that at higher fields, the separation between NMR lines is better for an identical line width of each line. For our application the ideal working field is around 0.5 to 0.6T for each sensor.

4.5 GMR response as function of the frequency

Although GMR have a range of working frequency from few Hz to GHz, we decided to test the response of GMR sensors as function of the frequency. The first test was GMR on a silicon substrate, the second one a GMR on glass and the last one a GMR on alumina.

To perform such a measurement, a coil is designed to be as close as possible to the sensor as presented figure 4.17. To avoid any direct coupling between the coil and the reception chain, the sensor is modulated via an AC power delivered by a Keitley generator, typically 2mA with a 2kHz frequency. This modulation principle will be explained more in detail in part 5.2.2. We then observe the signal on a spectrum analyzer.

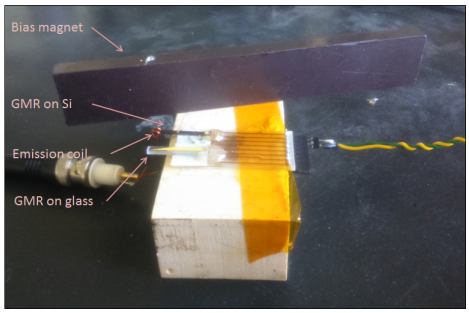

(a) Sensors and emission coil for GMR response in frequency

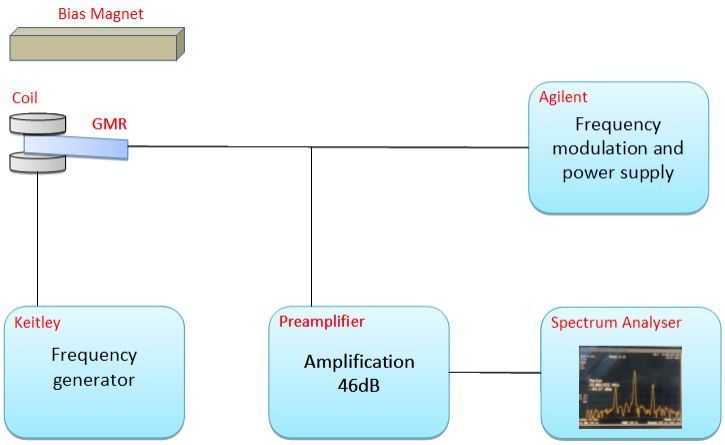

(b) Set-up scheme measurement

Figure 4.17: Frequency measurement of the GMR.

GMR response was studied between 1MHz to 26MHz frequencies. For this measurement two configurations were applied.

The first one when the GMR is in a sensitive state. As we see with the MR curves, at zero field, each sensors were in a saturated state. A bias magnet is then required to make them sensitive. The placement and the orientation of the magnet, providing the best output signal, was indicated by sending a 1 kHz into the coil and seeing the output signal directly on the oscilloscope.

The second one when the GMR is in a saturated state.

With this experiment we were able to plot graphs 4.18.

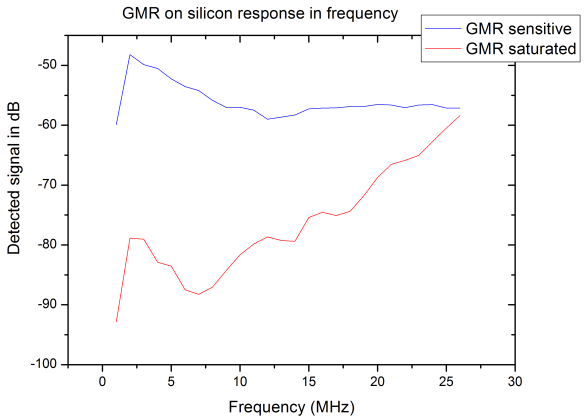

(a) GMR response as function of the frequency for silicon substrate.

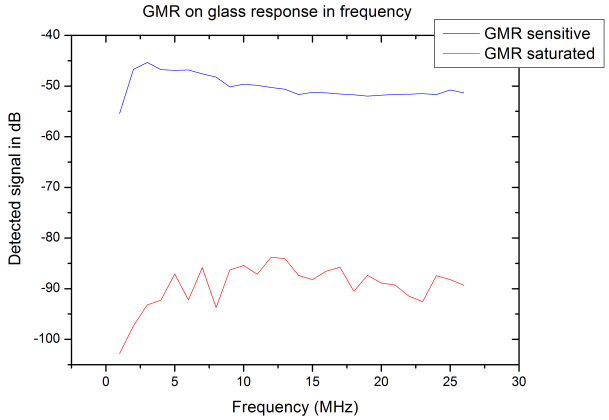

(b) GMR response as function of the frequency for glass substrate.

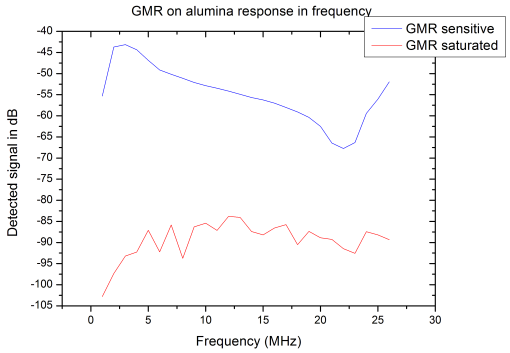

(c) GMR response as function of the frequency for alumina substrate.

Figure 4.18: GMR frequency response as function of the different substrates: silicon, glass and alumina. In red the when the sensor is in a sensitive configuration. In blue when the sensor is in a saturated configuration.

For each experiment the base noise level was around -90dB. We can conclude from these graphs that for GMR deposited on siliconat frequencies higher than 2MHz, a coupling through silicon appears. So at higher frequencies the measured signal is a combination of a coupled signal and a GMR signal. This phenomenon occurs even with the bulk silicon wafer. This point is still in discussion to understand what is really happening. But it seems that the silicon plays the role of a diode. GMR sensors are deposited on wafer of silicon on insulator. As the silicon is doped, at high frequencies, we could think that the wafer plays the role of a diode and the signal passes directly through it. By increasing the frequency, the coupling is also increasing and beyond a certain frequency, the direct coupling is dominant. At 0.6T the direct coupling through silicon

is such that the magnetoresistance effect is no more present.

Concerning the GMR on glass and alumina, we see that in the non sensitive state, the detected signal is around the base noise level. So we can consider that the signal detected in the sensitive state is the real signal detected by the sensor.

Conclusion

Here we showed that sensors present conventional magnetoresistance response. This chapter permits to highlight the fact that in presence of a magnetic field, applied perpendicularly to the sensor, there is a loss of sensitivity. But with the study of the figure of merit, we can find the best configuration, for the detection of the NMR signal, which is situated around 0.6T. An unexpected direct coupling was also highlighted with the sensors deposited on silicon. This point still needs to be understood. But for a first measurement we can work at low frequency with the sensor deposited on silicon. To work at higher frequencies, we will privilege sensor deposited on alumina or glass.

Chapter 5

Results

After laying the foundations of NMR on one side and of the magnetoresistance on other side, this chapter presents the obtained results. We begin to present the results obtained with a classical tuned coil for two magnetic field strengths,to prove that the built set-up works and determine the resolution limit of field. Finally we will present the different NMR spectrum obtained on water, ethanol, glutamate with the magnetoresistive sensors.

5.1 Determination of the set-up characteristics with the use of the tuned coil

Before working on GMR devices, experiments were performed with tuned coils in order to determine the different important characteristics of the set-up. For that we well use tuned coils whose role is dual: calibration and field adjustment. A first series of experiments were performed on water to validate the set-up and determine the best resolution that can be obtained. A second series of experiments were performed on ethanol since the spectroscopy aspect is the heart of the project.

5.1.1 13,30 MHz measurements

5.1.1.1 Water

The first NMR signal was obtained with water at 0.3T. This field value was chosen arbitrarily. We decided to choose water since its NMR spectrum consists in a single peak. Moreover, water is a simple liquid, well known and present in many domains. On figure 5.1 is presented the tuned coil used for the detection. The coil is empty allowing the positioning of a glass tube of 5mmx5mm inside.

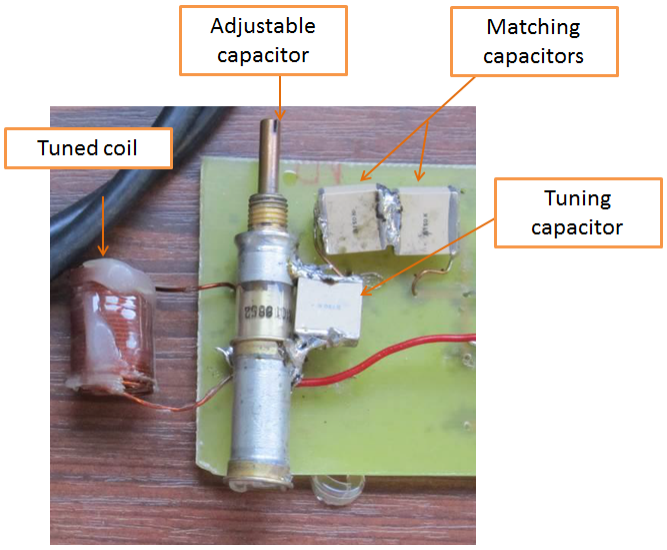

Figure 5.1: Tuned coil with its tuning and matching capacitors.

Below are presented the results that we obtained and that confirms that our NMR set-up is functional. Figure 5.2a presents the direct signal obtained and figure 5.2b shows the FFT of the direct signal. We can see that with one acquisition we have a bandwidth of 14Hz, which represents a homogeneity of 1ppm. To go forward, the spectroscopy of a simple ethanol phantom is performed.

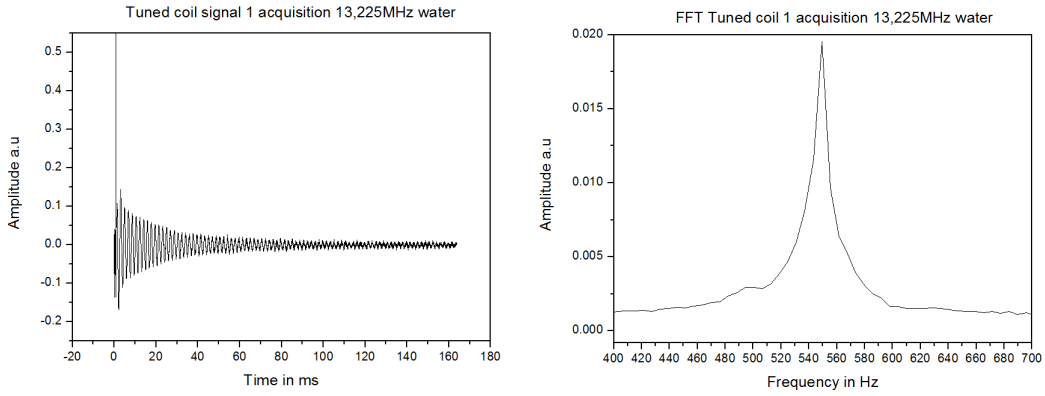

(a) (b)

Figure 5.2: NMR signal of water at 13.34MHz with no averaging (a) and its corresponding FFT spectrum (b)

5.1.1.2 Ethanol

Let's now consider a simple well known liquid: ethanol. Indeed, ethanol NMR spectrum consists in a set of three peaks, as presented in chapter 2. Figure 5.3 presents the

theoretical ethanol NMR spectra expressed in ppm. So for a frequency of 13,30 MHz we have an idea of the minimum required homogeneity to obtain the three set of peaks, which is of 13Hz.

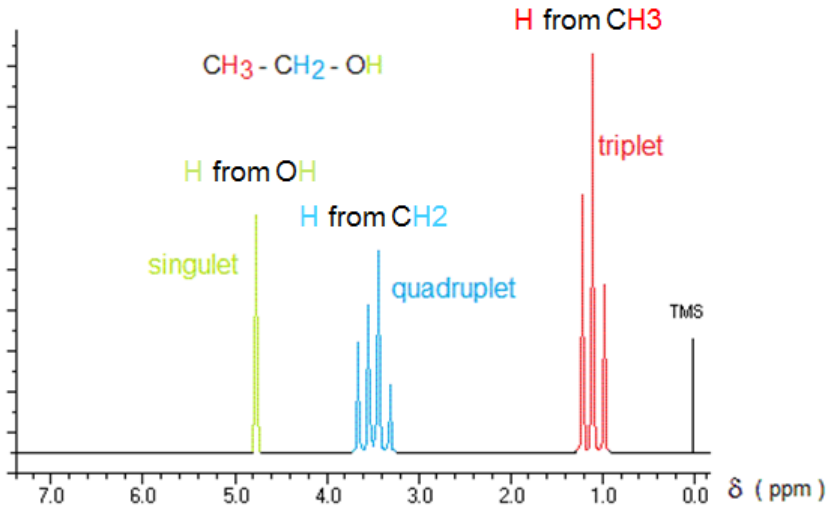

Figure 5.3: theoretical ethanol NMR spectra expressed in ppm in high field with TMS as the reference.

On figure 5.4 is presented the results that we obtained and that confirms that NMR spectroscopy is functional with this set-up. If we consider the first peak as the reference, we see that the distance between the first peak and the second peak is of 35Hz, which corresponds to 2.62ppm at 13.30MHz ,which is in adequation with the theoretical graph. Likewise for the third peak, the distance to the first peak is 59Hz, which corresponds to 4.42ppm at 13.30MHz.

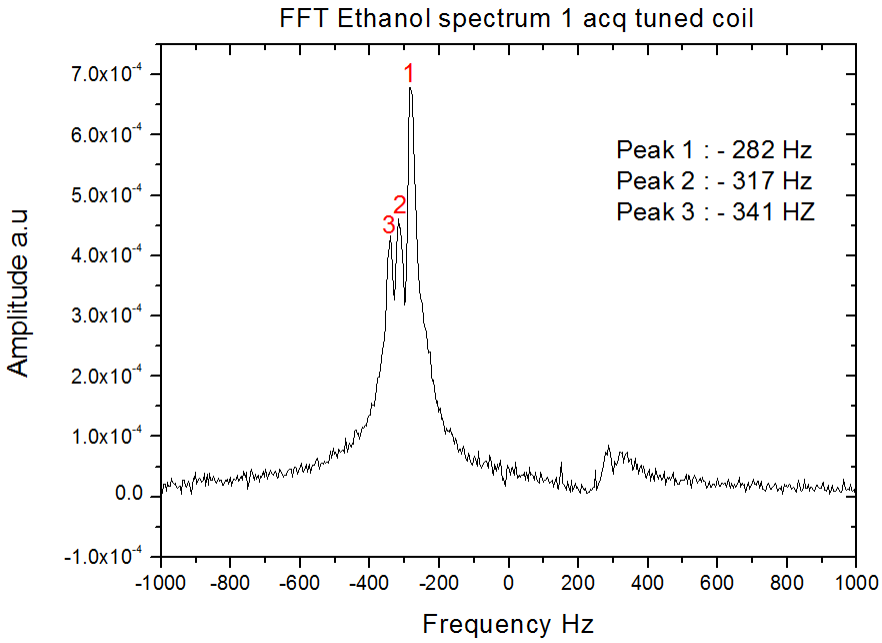

Figure 5.4: Ethanol NMR spectrum obtained with the tuned coil at 13,34MHz with the three expected peaks.

With the help of Patrick Berthauld form the Laboratoire Structure et Dynamique par Résonance Magnétique of the CEA Saclay, we were able to perform the same measurement at high field : 11T. To reach this field, they use a superconductive magnet. Figure 5.5 shows the result that was obtained. We see that the resolution is better than in our graph. Let's make a comparison between the two graphs. Figure 5.6 is a superposition of both graphics at 13,30MHz and at 500Mhz, which permits to realize that despite the lack of resolution of our set-up, we are still able to do spectroscopy.

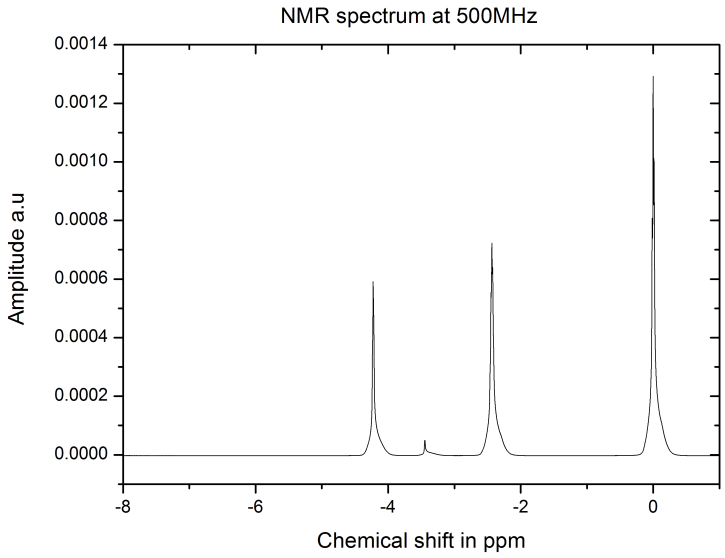

Figure 5.5: Ethanol NMR spectrum at 500MHz.

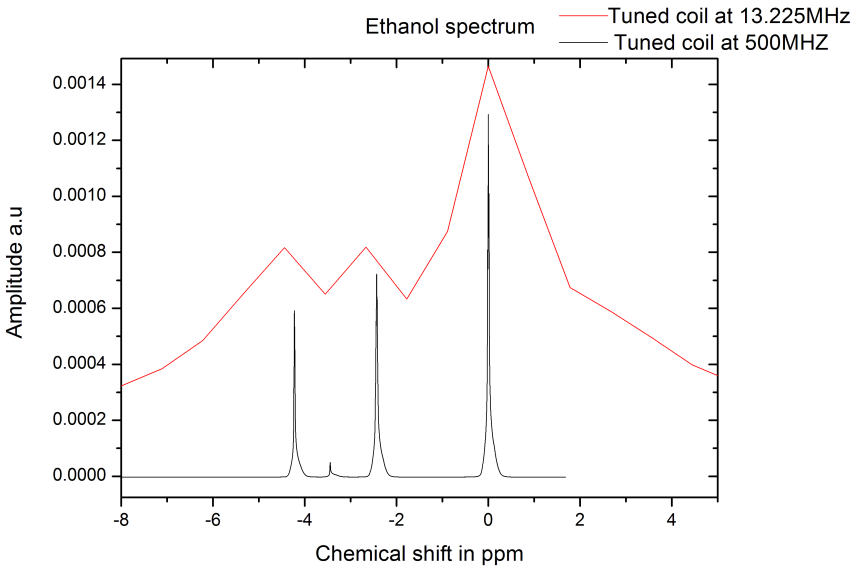

Figure 5.6: Ethanol NMR spectrum at 13,30 MHz and 500MHz

To simulate the spectrum, we use Loretzian having 14Hz width at the peaks position. Indeed 14Hz is the best homogeneity of our set-up. The simulation is presented in

figure 5.7 and compared to the tuned coil signal. We can deduce that the measurements performed at 500 MHz and 13.30MHz are fitting.

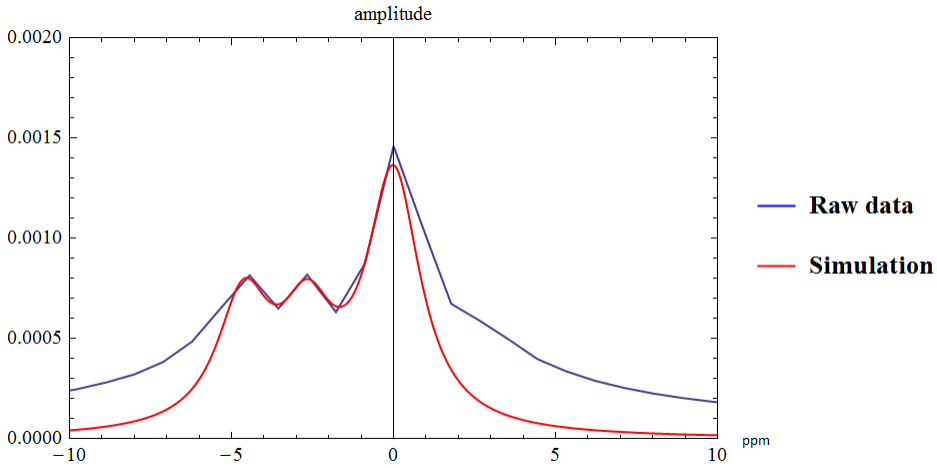

Figure 5.7: Raw data at 13.30MHz and simulation considering a band width of 14Hz.

We can then conclude that the NMR set-up is working, and enables us to perform spectroscopy. Nevertheless, we see that the resolution is not very good for ethanol. For this reason another series of experiments were performed at 26,30 MHz.

5.1.2 High field measurements

5.1.2.1 Water

The same experiments were lead at higher frequencies, to have a better peak separation for spectroscopy. For the reasons discussed in section 4.4, a field of 0.63T, corresponding to a frequency of 27.02MHz, was chosen. To work at this frequency, another coil had to be designed and tuned in frequency. Figure 5.8 shows the obtained spectrum of water after 100 acquisitions.

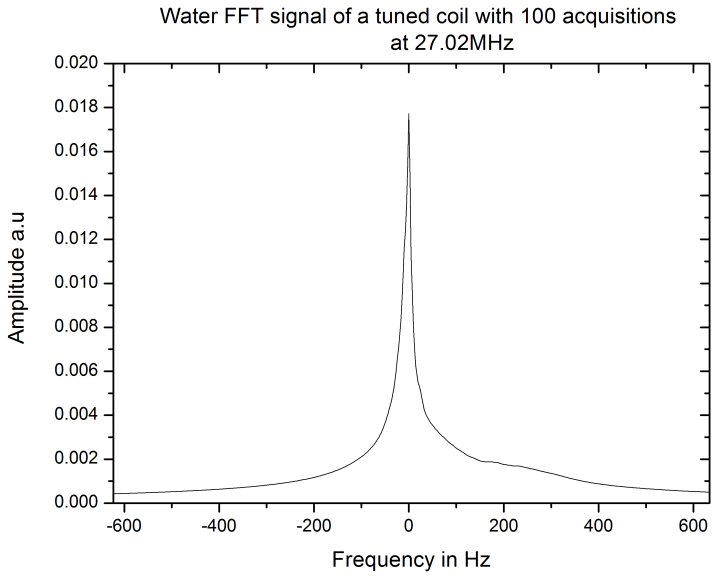

Figure 5.8: Water NMR signal obtained with the tuned coil at 27,02MHz.

We see with this figure that the set-up, including the emission and reception, is perfectly working. Moreover, with this water sample, we have a bandwidth of 21Hz. At this frequency, it represents an homogeneity of 0.78ppm, which is better than the value measured at 13.30MHz. It gives us the information that spectroscopy is also possible at this field. Nevertheless, at this frequency we didn't perform measurements on ethanol since before measuring ethanol with the GMR sensor we wanted to obtained results with water. But due to the reason explained in section 5.5 we didn't manage to do it.

5.1.2.2 Ethanol

We also did some measurements at 27.02MHz since this frequency corresponds to a magnetic field, were the sensor on glass is sensitive. Figure 5.9 shows the comparison between the tuned coil at 27.02MHz and the measurement done at 500MHz. We see that this set-up is also perfectly working. Moreover the result obtained at 27.02MHz perfectly fits with the one obtained at 500MHz. We can also see that we have a better resolution at 27.02MHz than at 13.30MHz. This is due to the fact that peaks are more distant thanks to chemical shift.

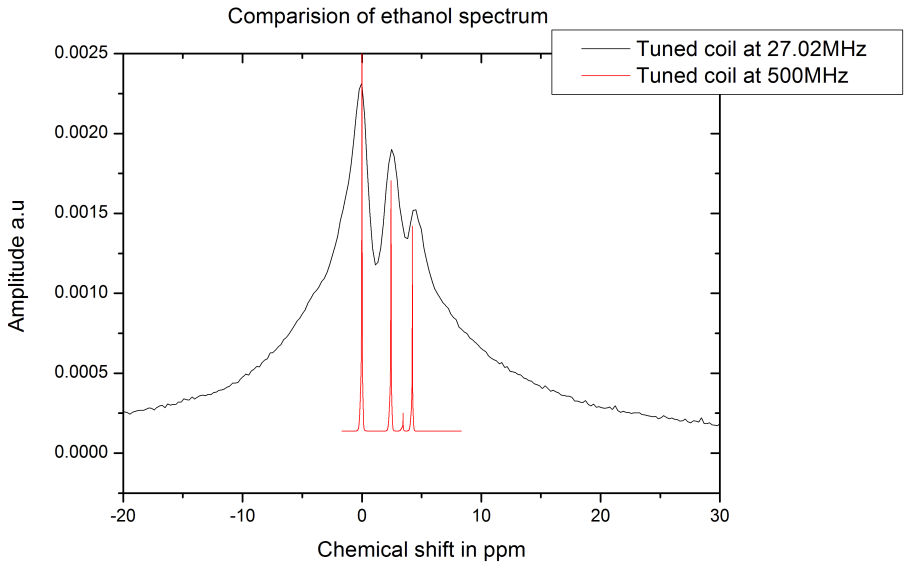

Figure 5.9: Ethanol NMR spectrum at 27.02 MHz and 500MHz

5.2 Results obtained with the GMR sensors

5.2.1 Direct inductive coupling detection with a magnetoresistive sensor

The first measurement which gave a result with the GMR sensor was in the configuration where the sensor was sensitive in the same direction of the detection coil, see figure 5.10. This measurement was performed on water at 13,30MHz.

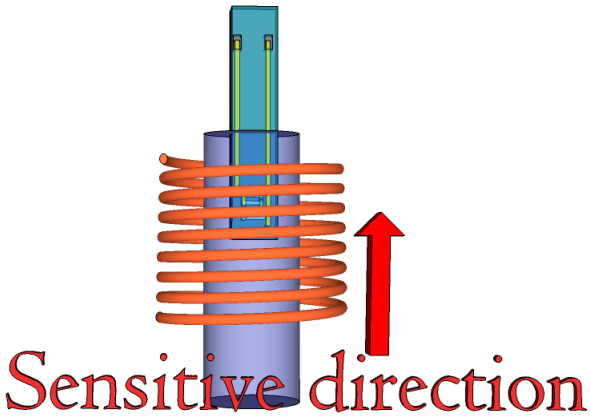

Figure 5.10: Scheme GMR sensitivity direction into the coil.

On the same graph presented on figure 5.11 we show the signal detected by the tuned coil and the GMR sensor for 100 acquisitions.

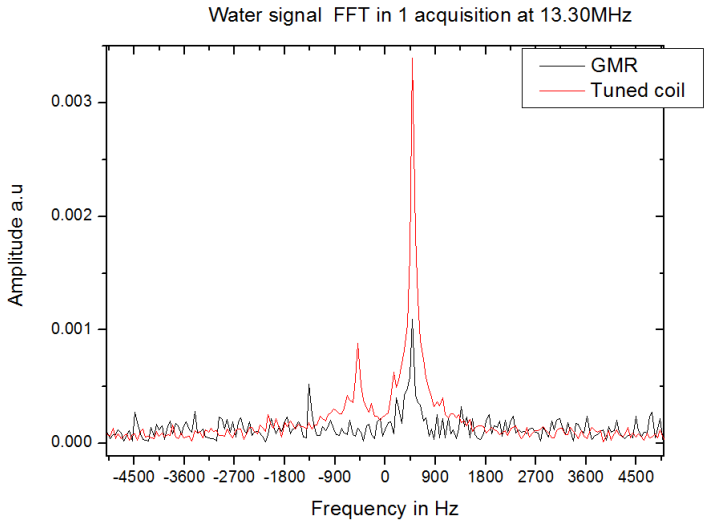

Figure 5.11: GMR and tuned coil detected signal at 13,30MHz in 100 acquisitions.

To validate this measurement, another measurement was performed when the sensor is in a saturated state (see figure 5.12).

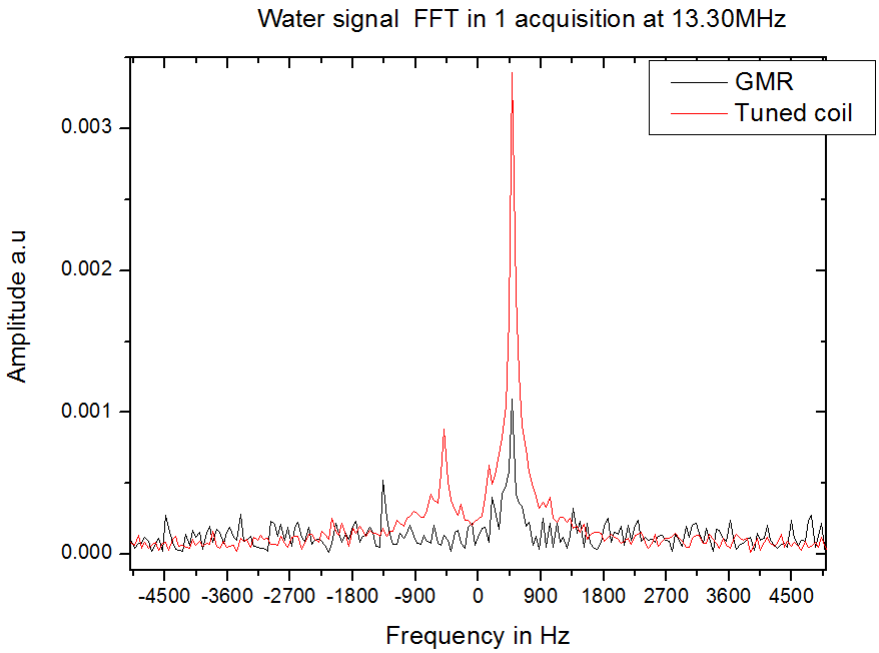

Figure 5.12: GMR detected signal while the sensor is in a saturated state. This signal is an inductive coupling between the tuned coil and the GMR sensor

In this configuration, the GMR sensor should not be able to detect any signal. Nevertheless a signal is measured (see figure 5.12), and could be explained by a direct inductive coupling between the coil and the sensor acquisition chain.

To decrease to the maximum this coupling, designing sensors where the sensitivity direction is perpendicular to the detection direction of the coil was undertaken. To change the direction of sensing two ways are possible. The first one is to design and process news sensors. The other possibility is to make a magnetic thermal annealing under field on sensors in order to switch the magnetization direction of the hard layer, leading to a switch in the sensitivity direction.

Magnetic thermal annealing To change the direction sensitivity of the sensor, we have to change the direction of the pinned layer of the spin valve. The pinned layer is pinned via direct coupling with an anti-ferromagnetic material. This effect is called exchange bias [66]. To change the direction of the pinned layer, the direction of the spin structure of the anti-ferromagnetic material has to be changed.

An annealing is then necessary. Indeed, beyond a certain temperature, called the Neel temperature, the thermal energy is sufficient enough to break the microscopic magnetic order of the material. The anti-ferromagnetic material becomes para-magnetic. Then the direction of the magnetic field orients the ferromagnetic layer magnetization. During the cooling down, the interfacial coupling will orient the anti-ferromagnetic spin

structure. This procedure allows to control the direction of the pinning.This is well illustrated figure 5.13.

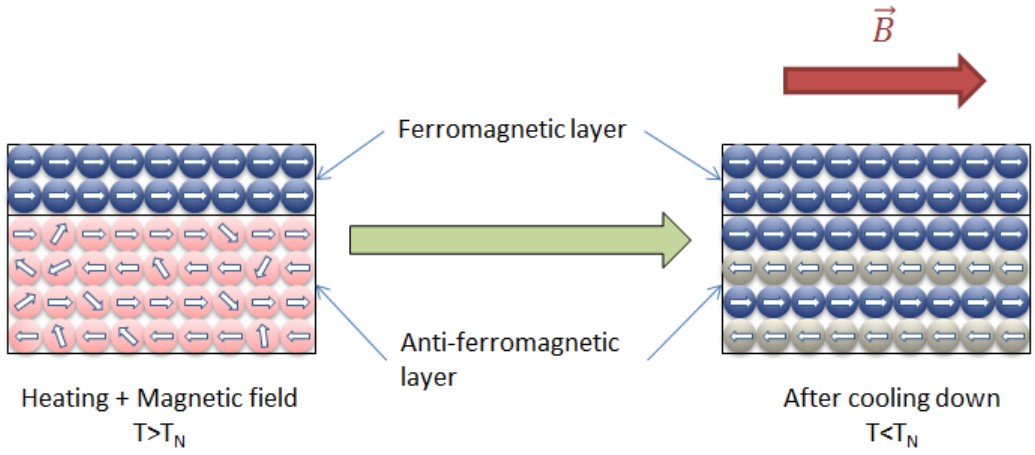

Figure 5.13: Magnetic thermal annealing principle.

Our set-up is a home made set-up composed of an electromagnet producing a field of 5000Gauss, large enough to orient the ferromagnetic layer, a vacuum oven which can reach a temperature of 350°C. The full set-up is presented figure 5.14. We see the electromagnet on the left with in the middle the space where the heating cane should be placed.

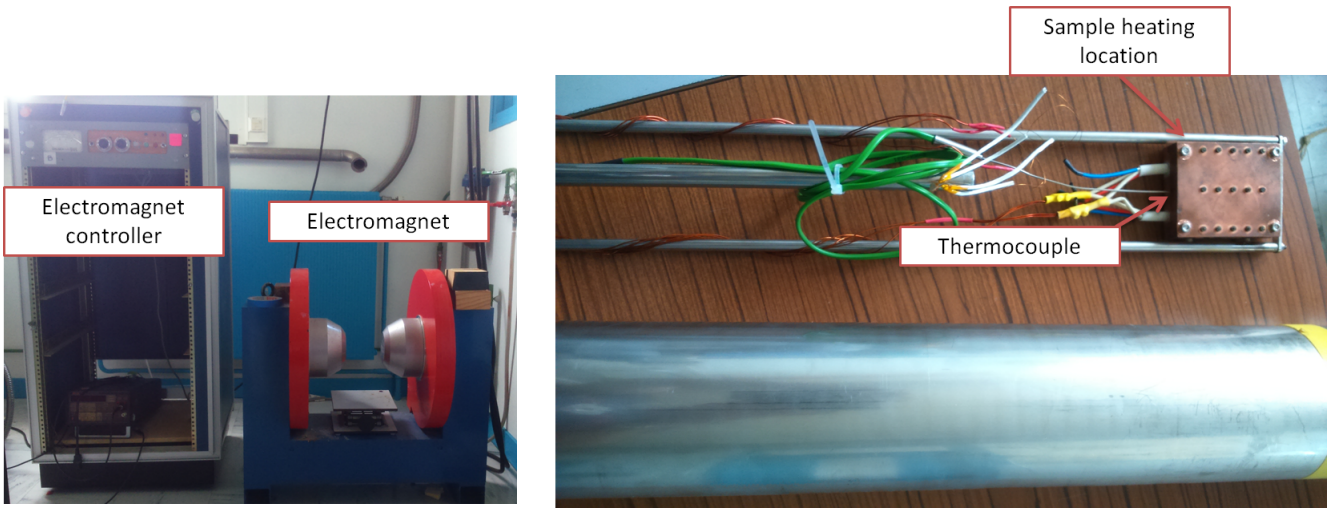

(a) (b)

Figure 5.14: Home-made magnetic thermal annealing set-up with the electromagnet (a) and the oven (b).

For our samples, where the anti-ferromagnetic layer used to block the pinned layer is composed of PtMn, we made a magnetic thermal of 30 minutes under a field of 5000Gauss and a temperature of 250°C. In figure 5.15 is presented the magnetoresistance of the sensor before the thermal annealing, while the annealing is not completed and when the annealing is completely done.

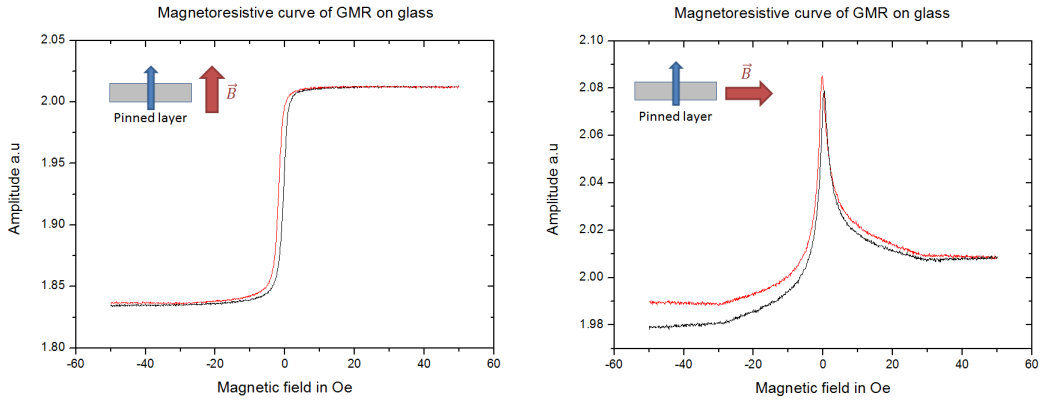

(a) (b)

Initial configuration

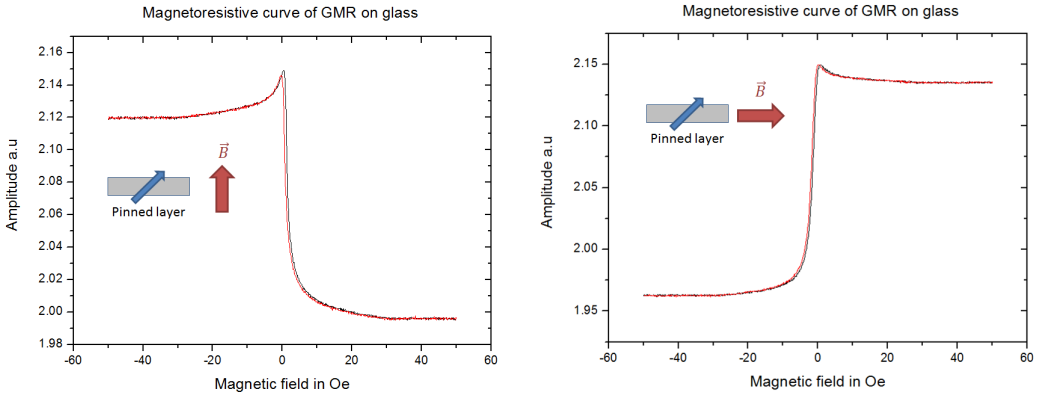

(c) (d)

Configuration where the sensor is half annealed

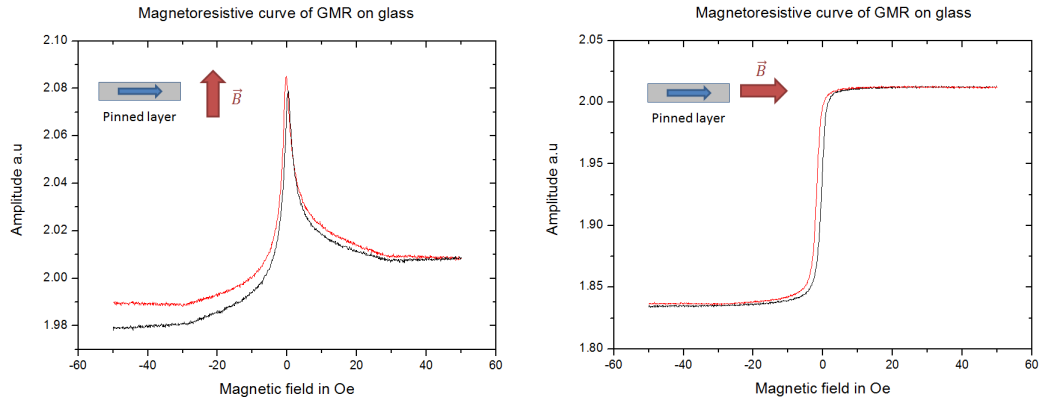

(e) (f)

Final configuration

Figure 5.15: Magnetoresistance of the sensor as function of the direction of the hard layer and as function of the direction of measurement. (a), (c) and (e) the field measurement is perpendicular to the direction of the yoke. (b), (d) and (f) the field measurement is parallel to the direction of the yoke. The hard layer is initially perpendicular to the yoke. An annealing at 250°C during 30min and under 5000Gauss orients the pinning of the block layer at 90°C, parallel to the GMR structure.

Detection of the signal in cross sensitivity direction Below, on figure 5.16, is presented results when the sensitivity direction of the GMR is perpendicular to the detection direction of the coil. We see that the direct coupled signal between the sensor and the coil is still present but reduced compared to the parallel configuration. For the rest of the work, even if the direct coupling signal is present in both configurations, we have chosen to work with this cross sensitivity direction configuration to minimize this inductive coupling.

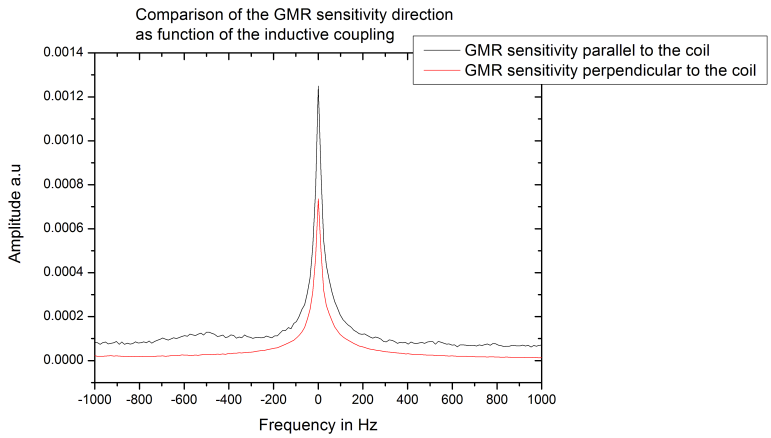

Figure 5.16: Inductive coupling detected when the GMR sensor is sensitive along the direction of detection of the tuned coil and when the GMR sensor is sensitive perpendicular to the direction of detection of the tuned coil.

5.2.2 Modulation and demodulation principle

To reduce the direct inductive coupling between the GMR sensor and the tuned coil, we decided to work in the cross anisotropy configuration, but also to use a modulation technique. Here I present the principle which consists to modulate the GMR supply.

Let's consider the GMR output voltage with the Ohm law:

$$V_{GMR} = \left[R_0 + \frac{dR}{dH} H \right] I \tag{5.1}$$

Where R_0 is the resistance of the sensor in its parallel configuration, $\frac{dR}{dH}$ is the sensitivity of the sensor and I the current supplying the GMR.

The modulation consists in fact to supply the GMR in AC so we can write:

$$I = I_0 cos(\omega_0 t + \varphi_0) \tag{5.2}$$

and to simplify the notation we write $\frac{dR}{dH} = R_1$

Moreover the detected signal is a damped sinusoid. But in first approximation we can write :

with $H = H_0 cos(\omega_H t + \varphi_H)$

We have :

$$V_{GMR} = [R_0 + R_1 H_0 cos(\omega_H t + \varphi_H)]\, I_0 cos(\omega_0 t + \varphi_0)$$

$$V_{GMR} = R_0 I_0 cos(\omega_0 t + \varphi_0) + R_1 H_0 I_0 cos(\omega_0 t + \varphi_0) cos(\omega_H t + \varphi_H)$$

$$V_{GMR} = R_0 I_0 cos(\omega_0 t + \varphi_0) + \frac{R_1 H_0 I_0}{2} \left[cos\left[(\omega_H - \omega_0)t + \varphi_H - \varphi_0\right] + cos((\omega_H + \omega_0)t + \varphi_H + \varphi_0)\right]$$

To demodulate the signal we have to multiply the output voltage by a sinusoid at the same frequency: $V_{Dem} = V_{GMR} \times cos(\omega_H t + \varphi_H)$

$$V_{Dem} = \left[R_0 I_0 cos(\omega_0 t + \varphi_0) + \frac{R_1 H_0 I_0}{2} \left[cos\left[(\omega_H - \omega_0)t + \varphi_H - \varphi_0\right] + cos\left[(\omega_H + \omega_0)t + \varphi_H + \varphi_0)\right]\right]\right] cos(\omega_H t + \varphi_H)$$

$$\begin{array}{c} V_{Dem} = \frac{R_0 I_0}{2} \left[cos\left[(\omega_H - \omega_0)t + \varphi_H - \varphi_0\right] + cos\left[(\omega_H + \omega_0)t + \varphi_H + \varphi_0\right]\right] + \\ \frac{R_1 H_0 I_0}{4} \left[cos\left(\omega_0 t + \varphi_0\right) + cos\left[(2\omega_H - \omega_0)t + 2\varphi_H - \varphi_0\right]\right] + \\ \frac{R_1 H_0 I_0}{4} \left[cos\left(\omega_0 t + \varphi_0\right) + cos\left[(2\omega_H + \omega_0)t + 2\varphi_H + \varphi_0\right]\right] \end{array}$$

$$\begin{array}{c} V_{Dem} = \\ \frac{R_0 I_0}{2} \left[cos\left[(\omega_H - \omega_0)t + \varphi_H - \varphi_0\right] + cos\left[(\omega_H + \omega_0)t + \varphi_H + \varphi_0\right]\right] + \frac{R_1 H_0 I_0}{2} cos\left(\omega_0 t + \varphi_0\right) + \\ \frac{R_1 H_0 I_0}{4} \left[cos\left[(2\omega_H - \omega_0)t + 2\varphi_H - \varphi_0\right] + cos\left[(2\omega_H + \omega_0)t + 2\varphi_H + \varphi_0\right]\right] \end{array}$$

A low-pass filter is then added. We can see that if we look for a signal at 13MHz and if we supply the GMR in AC at $\omega_0 = 300Hz$ with a low pass filter at 10kHz, we will have our modulated signal from either side of the coupled signal shifted by 300Hz. Moreover, to avoid any phase problem, each equipment is phase locked.

Figure 5.17 presents the overall diagram for the modulation principle and the obtained FFT.

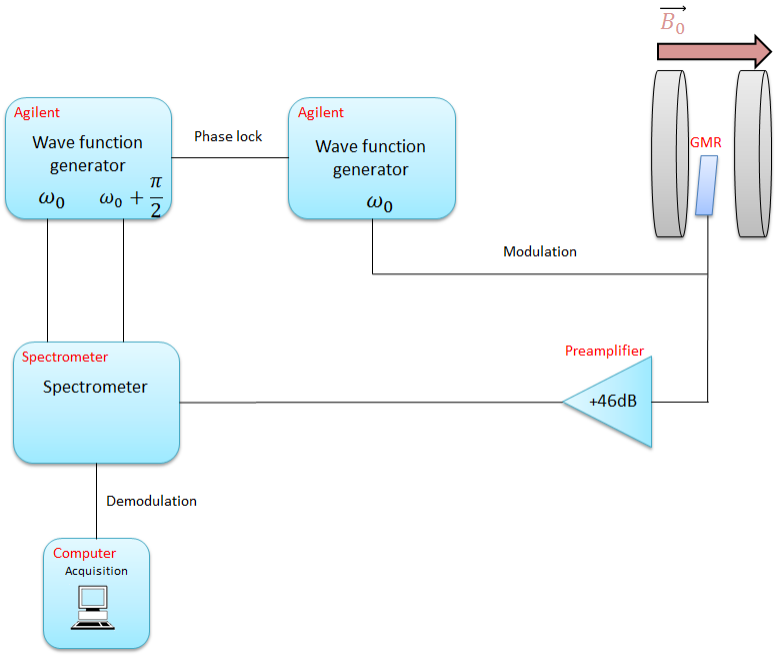

(a) Modulation-Demodulation block diagram

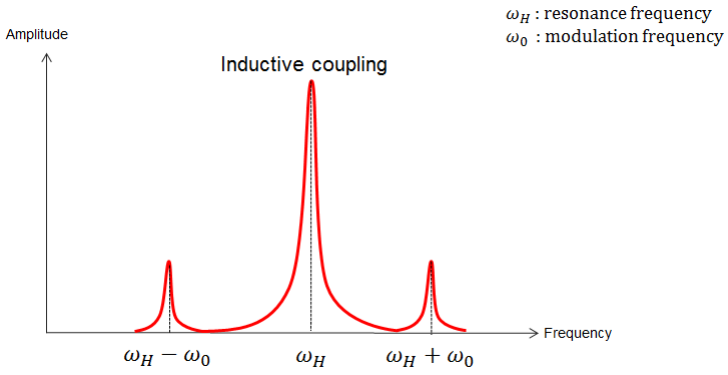

(b) FFT after demodulation

Figure 5.17: Modulation-Demodulation block diagram and the obtained FFT

5.2.3 Obtained results at 13,30 MHz with GMR sensors on Silicon

A first series of experimentation were led at 13,30MHz, which corresponds to a magnetic field of about 0.31T. This value was first chosen arbitrarily. But we then realized that at this field, placing the GMR in a sensitive way overlooked to the B_0 field can be done in an easy way. In this first measurement, GMR on silicon sensors were chosen.

5.2.3.1 Water

Figure 5.18 presents the result obtained with a GMR sensor placed into water. The sensor was AC supplied at 4kHz with a 6V input. The inductive coupling is well present. Moreover, the true signal detected by the sensor is well placed on either side of the central peak at the supplied frequency. Figure 5.18a and 5.18b are zooms on the true signal detected by the sensor which correspond to the modulated signals.

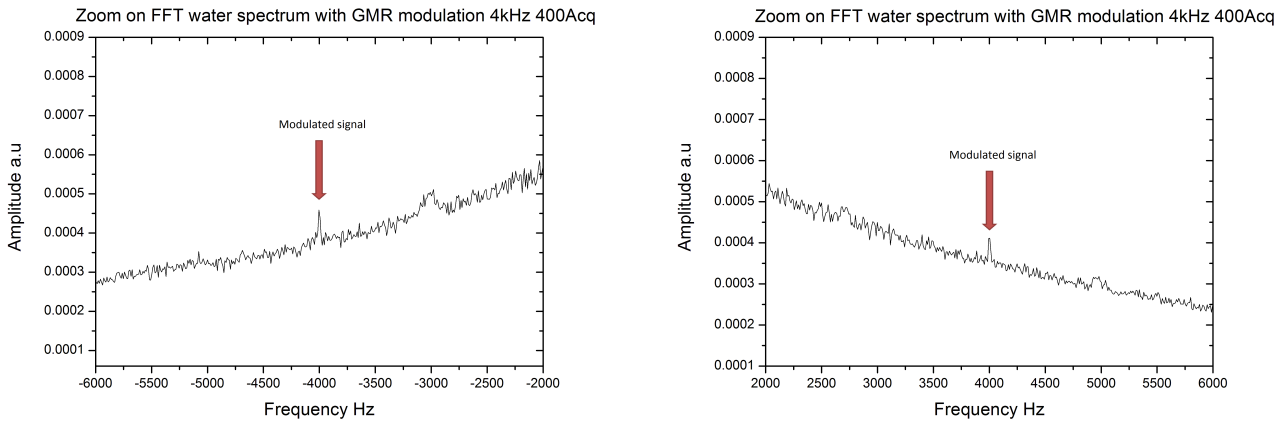

(a) (b)

Figure 5.18: Water NMR spectrum at 13.30Mhz with a modulation frequency of 4kHz and 400acquisitions. (a) is the modulated signal at -4kHz and (b) the modulated signal at +4kHz.

To confirm the first obtained results, we performed the same experiment with a modulation frequency of 3kHz (see figure 5.19). But in this case we increased the AC supply to 8V, which permits to have a better sensitivity and by the way a better signal-to-noise ratio for the same acquisition number.

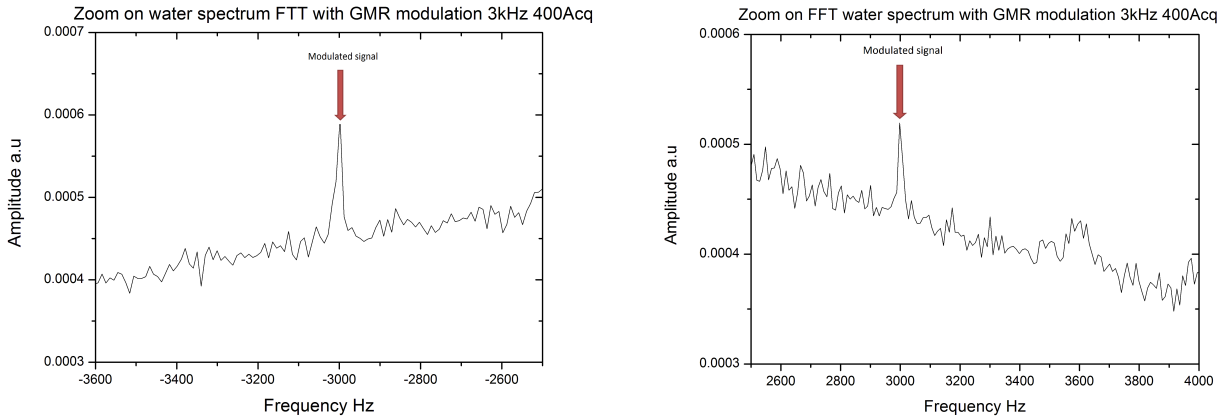

(a) (b)

Figure 5.19: Water NMR spectrum at 13.30Mhz with a modulation frequency of 3kHz and 400acquisitions. (a) is the modulated signal at -3kHz and (b) the modulated signal at +3kHz.

The major difference between the two obtained graphs lies in the fact that with the 3kHz modulation, the sensor was supplied with an input voltage of 8V while the 4kHz modulation has an input voltage of 6V. Moreover, the difference of amplitude, is not only due to the input voltage, but also to the position of the GMR in the field. I tried to be as precise as possible while I adjusted the position sensor but a margin of error still exists. Indeed the positioning of the sensor is manual and some elastic effects on the rotation system could occur. The convolution of theses two facts leads to this difference of amplitude.

Moreover this simple experiment also allows the validation of the retiming and the averaging of the FFT for each acquisition. We can also notice that the bandwidth of the signal detected by the GMR is of 15Hz, compared with the 14Hz of the tuned coil. We can conclude here that we do not notice any major gain in bandwidth with the GMR. This absence of gain in the bandwidth probably comes from the fact the retiming of the FFT is not perfectly done at the maximum of the peak. Nevertheless, it confirms that we can work with the modulation configuration.

5.2.3.2 Ethanol

Now that we demonstrated that NMR was possible with GMR sensors, and that the line width allows us to do spectroscopy, we tried the same experiments on ethanol. Figure 5.20 presents the obtained results. We see that the inductive coupling is still present. With 3000 acquisitions, we clearly see our three expected peaks. Here the sensor was supplied with an input voltage of 5V. To try to reduce this amount of acquisitions, we decided to increase the input voltage to 8V. Unfortunately, the sensor broke up due to

some oxidation of the magnetoresistive part. This is shown on figure 5.21 where we can see the magnetoresistive meander totally in black.

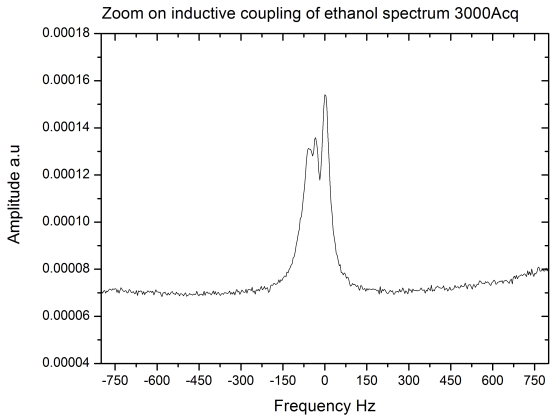

(a) Zoom on inductive coupling of ethanol NMR spectrum at 13.30MHz with 3000 acquisitions.

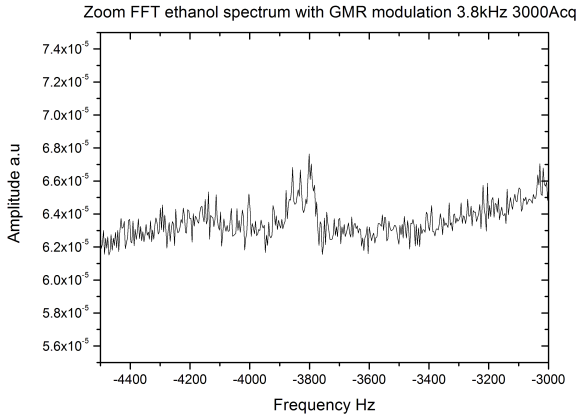

(b) Zoom on ethanol NMR spectrum. Here the modulated signal at -3.8kHz.

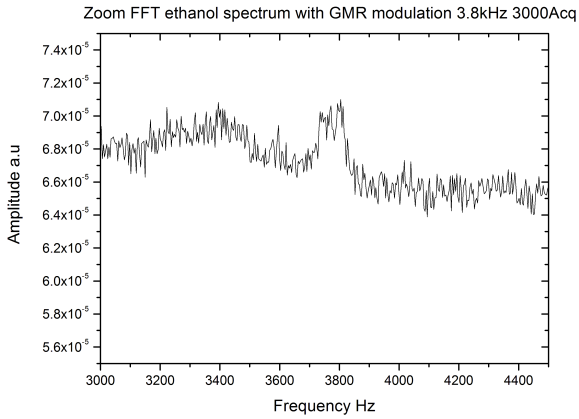

(c) Zoom on ethanol NMR spectrum. Here the modulated signal at +3.8kHz.

Figure 5.20: Ethanol spectrum at 13.30Mhz with a modulation frequency of 3.7kHz and 3000 acquisitions.

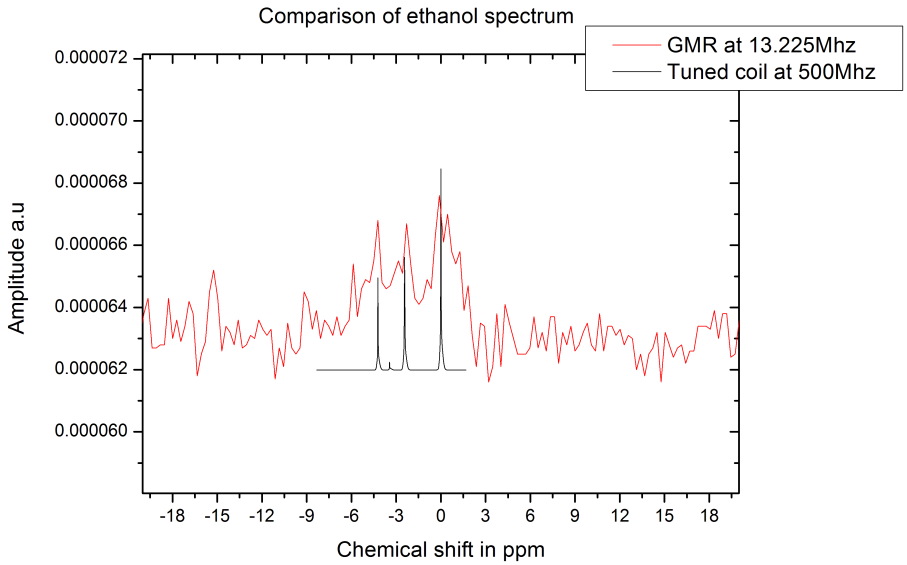

Figure 5.22: Comparison between spectra obtained with a tuned coil at 500MHz and the GMR sensor at 13,225MHz on an ethanol sample.

Figure 5.21: Broken sensor due to oxidation of the magnetoresistive part.

We also see on on figure 5.20 that the signal detected by the GMR does not present perfect peaks and appears as a large bandwidth. This is mainly due to the retiming of the FFT. Sometimes, due to some environmental noise, the maximum of the FFT signal is not a single point but more a set of points. So the retiming is sometimes shifted by a few hertz.Moreover, if we compare, between this spectrum and the spectrum obtained with the tuned coil at 500Mhz we obtain the graph presented in figure 5.22.

Another explanation for a large bandwidth is the fact that we are in the strong regime coupling. Indeed, between the two obtained graph at 13.30 MHz and 500MHz, we see some differences. We have a J-coupling of 7Hz for ethanol and the shift dur to chemical shift is of 2,5ppm which represent at 13.30MHz a shifting of 33Hz and at 500MHz a shifting of 1.25kHz. So we have the ratio $\frac{\triangle\nu}{J} = 4.7 < 10$ for the low field measurements and $\frac{\triangle\nu}{J} = 178.5 > 10$ for the high field measurements. We are then in the regime called the strong coupling regime for the first case and in the low coupling regime for the second case. This was explained in 2.3. Nevertheless here I present some simulations obtained considering this strong regime coupling.

This permits to clearly highlight the fact that the peaks detected by the GMR sensor fits with a theoretical NMR spectrum. But we can see that there is a larger bandwidth. If we make a simulation, taking into account a bandwidth of 0.98ppm on the 500MHz spectrum and if we plot it on the same graphic, we obtain the figure 5.23. Moreover with this simulation we can see that we have a better resolution with the GMR sensor than with the tuned coil at the same frequency. And this is particularly important since the considered working volume is of a few µm^{3}for the GMR sensor compared with the few cm^3 of the tuned coil.

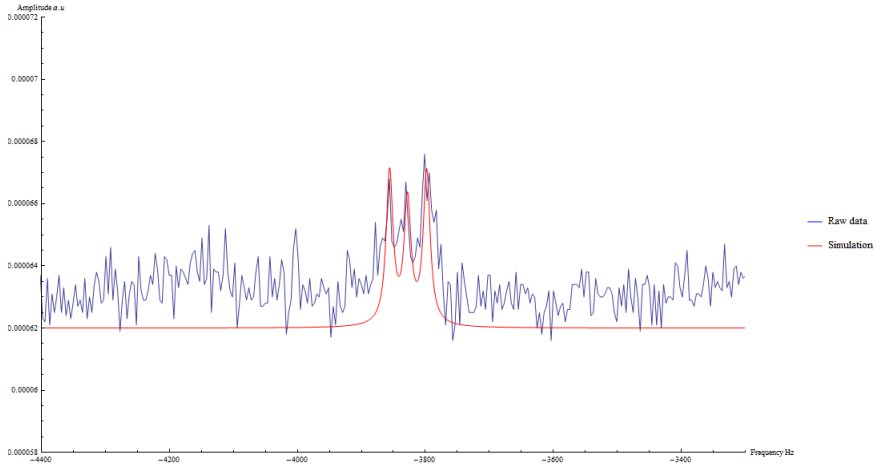

Figure 5.23: Raw data at 13.225MHz and simulation with a bandwidth of 13Hz.

Sensors on silicon enabled to highlight the fact that the set-up was functional and thus obtain results on simple sample such as water and ethanol. Taking into consideration a sensitivity of the sensor within the magnetic field (0.3T) of about 7%/mT, supplied with $5V_{pp}$, and a signal-to-noise of 4 with 3000 acquisitions, we can say that the detected signal is 10.5pT. This is in agreement with the estimated signal of 15pT. The difference of estimated signal and calculated signal can come from the fact that the sensor sensitivity is not 7%/mT but a little lower. Indeed, the placement of the GMR sensor within the magnetic field is manual and can be delicate.

5.2.3.3 Validation to a real biological sample: Glutamate

One of the objectives of the subject was to perform local NMR on biological tissues. For that we also performed an experiment on a glutamate solution. Glutamate is an important excitatory neurotransmitter that plays the principal role in neural activation. To be as close as possible to the reality, we decided to take a concentration of $6mM.L^{-1}$. To be able to compare with what can be done with a high resolution experiment, we also performed experiment at 500MHz. Figure 5.24 shows the obtained results with 400acquistions for the GMR sensor and the tuned coil at 500MHz.

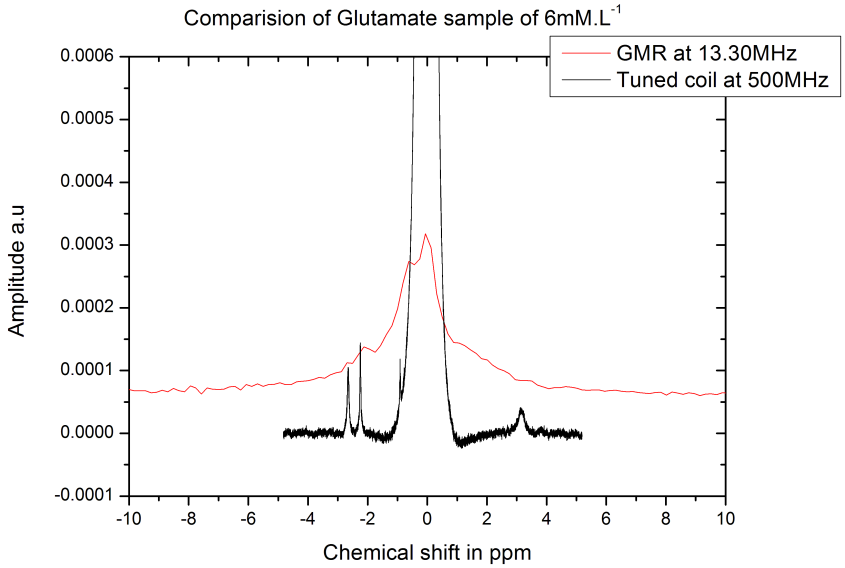

Figure 5.24: Comparison between spectra obtained with a tuned coil at 500Mhz and the GMR sensor at 13,30MHz on a Glutamate sample concentrated at $6mM.L^{-1}$.

We can see that we obtain a signal with the GMR sensor even if the resolution is not very good. This is due to the fact that the concentration in very low and we do not have enough homogeneity. So the water peak has too much bandwidth to let appear the glutamate signal. Nevertheless, we see that there is still a signal corresponding to the glutamate signal. With the GMR sensor we have a local information, and then it is more sensitive to a low concentration, and even if we do not have a good resolution we can however see the two different types of peaks. This may be explained by some deposition of glutamate molecules on the sensor surface.

5.2.4 Result obtained on ethanol at 12.33MHz with GMR sensors on alumina

Due to some coupling trough silicon at high frequencies, we decided to work with another substrate. We had two available choices in the lab, GMR deposited on glass and GMR deposited on alumina. Since, as seen in part 3.3.2.1, GMR on alumina had more sensitivity than GMR on glass, the alumina substrate sensor was chosen.

Figure 5.25 shows the results obtained with the alumina sensor. We see that we have a signal. But this one is not well defined. Nevertheless, we can plot with this graph, the graph obtained at high frequency to see that it fits. This is shown on figure 5.26.

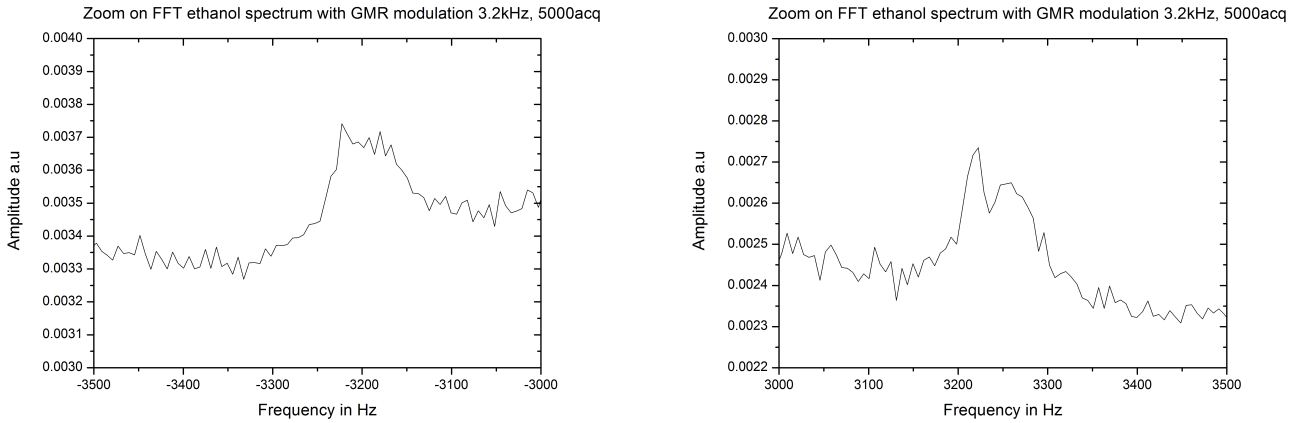

(a) (b)

Figure 5.25: Ethanol NMR spectrum at 12.33MHz with 5000 acquisitions. (a) a zoom of the modulated signal at -3.2kHz and (b) a zoom of the modulated signal at +3.2kHz.

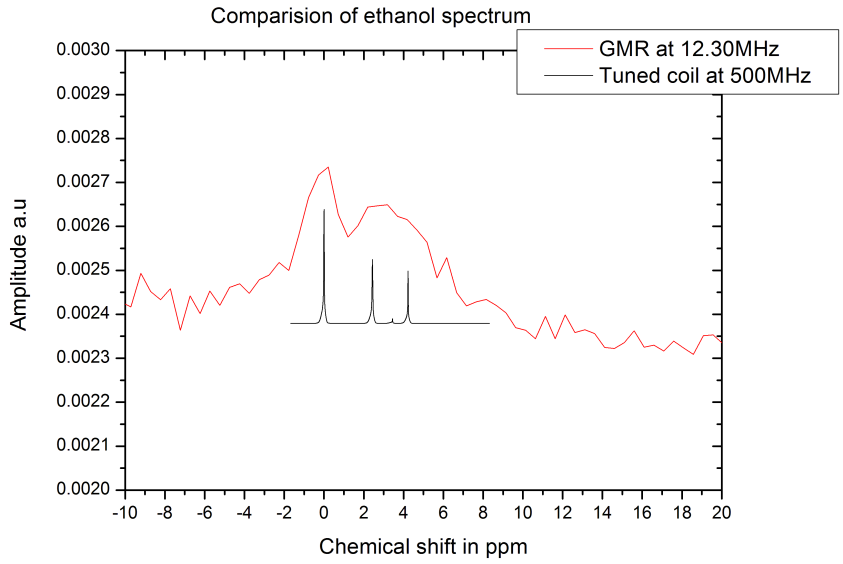

Figure 5.26: Comparison between spectra obtained with a tuned coil at 500Mhz and the GMR sensor at 12,30MHz on an ethanol sample.

To have a better resolution we could have done more acquisitions but this was not possible. Indeed as ethanol is a volatile sample, after a moment the sensor is no more in presence of liquid. Moreover after refilling the sample we realized that the sensor resistance had increased by 300Ohm, which means that it is about to break. Unfortunately no more wafer of GMR on alumina were available. Thus we could not fabricate other sensors.

But we can say that it is possible to have a signal with a GMR deposited on alumina.

5.2.5 Results obtained on water at 26.79MHz with GMR sensors on glass

A series of experiments were also lead at 0.62T with GMR on glass. Indeed, with the figure of merit seen in chapter 4, we realized that this B_0 magnetic field is best configuration to detect a NMR signal. For that we decided to work on water. The sensor was AC supply at 5kHz with a 6V input. Figure 5.27 presents the result obtained with a GMR on glass sensor placed in water.

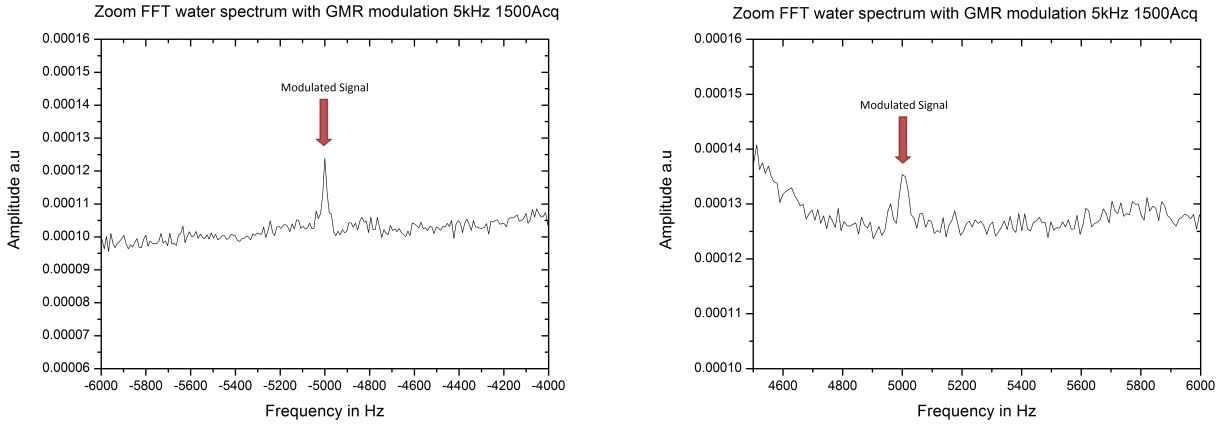

(a) (b)

Figure 5.27: Water NMR spectrum at 26.79Mhz with a modulation frequency of 5kHz and 1500acquisitions. (a) is the modulated signal at -5kHz and (b) the modulated signal at +5kHz.

We can notice on these graphs that the signal at +5kHz has a lower signal to noise ratio than the one presented at -5kHz. This is due to the fact that the noise level around +5kHz is higher than the noise lever at -5kHz. This probably comes from the presence of some environmental noises at this frequency.

Discussion and Conclusion

- As the silicon was the heart of the problem, the decision to work with sensors deposited on glass or alumina was taken. Indeed with these two substrates the observed direct coupling at high frequencies was not present. Moreover, we managed to have some results with sensors on alumina at 0.3T on glutamate sample and at 0.6T with sensors on glass on water samples.

- Due to magnetic field fluctuations, the resolution obtained with sensors cannot be better than the resolution of the tuned coil. Indeed, the way the "lock" works is not compatible with high resolution. Moreover, at high magnetic field the electromagnet is not homogeneous enough to go further in the analysis. Ideally, we should have access to conventional lock, as described in the first chapter, and also to increase the homogeneity of the magnetic field to be able to have a better resolution. Furthermore, theses two upgrades enables to work independently with the sensor and be able to work without the inductive coupling coming from the tuned coil.

- With the magnetoresistive sensor we are able to decrease the size to few micron in order to probe locally a NMR signal. In comparison to tuned coil, we can play on the sensor size to fit the sample of study.

- Another alternative to GMR devices, is TMR devices. In comparison to GMR, TMR have a higher magnetic noise at low frequency. For the NMR application this is not a problem since the working frequency is of a few MHz. Moreover, the sensitivity of TMR can be increased by a factor of 10, in comparison to GMR. As for the GMR devices, MTJ are untuned sensors and can adjust their sizes to the sample size. Currently we cannot work with theses sensors, since we cannot process them, but they can soon be processed in the laboratory.

- Local performance of GMR sensors was shown by estimating its resolution volume. Taking into account that this volume depends on the GMR surface, a resolution volume less than $50.10^3 \mu m3$ (0.05 nL) could be reached. Then, the feasibility of NMR acquisition on water solution was proved with a SNR of about 3 in 400 and 3000 acquisitions for water and ethanol respectively while maintaining acceptable resolution capacities of 1 ppm. Regarding inductive microprobe, *Mcdowell et al.* [67] that a SNR of $0.46/\sqrt{\text{Hz}}$ on a sample volume of 1.2 nL at 1 T using a solenoid microprobe was reached with one acquisition. However, knowing that SNR is proportional to filling factor and the number of dipoles on solution, this SNR will be at least 10^5 orders less for a volume of 0.05 nL at 0.3 T.

This final chapter showed that the last set-up that we built is perfectly working. There is still a problem of homogeneity and field stabilization which is due to the electromagnet. The results obtained with the GMR sensor is also quite concluding. With these measurements we realized that at high frequencies silicon substrate sensors are of no use and we should investigate other substrate. We performed measurements with alumina substrate which gave us a beginning of result. If we want to go more deeper in results we should have sensors on alumina or glass substrate whose sensitivities and magnetoresistance are comparable with silicon substrate sensors.

Conclusion and perspectives

This thesis demonstrated a new approach for NMR spectroscopy measurements. Starting from almost nothing we were able to achieve a full working set-up with the integration of our magnetoresistive sensor. The power of this thesis lies in the fact that the estimated probed volume is straddling between what can be done with current tuned coil which are of macrometric sized and NV center which probe at the nanoscale.

Before any measurement, simulations were done considering the simple experiment where the sensor is immersed into the sample. It gives us the order of magnitude of the expected signal which is of a few pT, which implies that with our magnetoresistive sensors, a high control of the sensitivity within the magnetic field is required. Other simulations were also done for the next challenging step, which consists in a sensor placed above a microchannel. With this simulation we also notice that the expected signal will be of the order of magnitude of few pT.

After the simulations we worked on the sensor design. To have the best sensitivity with a low noise the meander shape was chosen. Moreover with this configuration we can have different sizes which determine the probed volume. Moreover as the detected signal will be in the range of MHz frequencies, contacts where designed as strip-lines. Sensor were then processed with classical microfabrication techniques which include ionic etching, evaporation in Ti/Au to avoid oxidation and sputtering for the passivation layer. Sensors were finally cut into bar shape with a diamond saw.

Sensors are then characterized. The relevant informations were extracted such as percentage of magnetoresistance, sensitivity, noise and magnetoresistance in function of the frequencies. This makes us realize that from a certain frequency, with silicon substrate sensor, a direct coupling annihilates the magnetoresistive effect. So we had to probe other substrates and we characterized them in the same order of idea. Finally, the alumina substrate was chosen since its spin-valve had a better sensitivity than the other tested sensors.

To investigate NMR signals we first decided to work with a permanent magnet. Due to the lack of homogeneity and the weak magnetic field of this one, we decided to work

with a small electromagnet. This one also had some problem of homogeneity, but also of field stability due to the power supply. Finally, an old electromagnet with shim coils was chosen. The problem of field stability was still present but was partially solved by signal processing. The integration of the sensor and its precise position into the gap magnet was also built. From this point, we were able to perform some measurements. We obtained results at low field, 0.3T, with silicon substrate sensor on water, to demonstrate that the set-up is functional; On ethanol, to show that spectroscopy is possible; and on glutamate with a concentration of $6mM.L^{-1}$. We also had a result on ethanol with a sensor on alumina substrate and on water with a sensor on glass substrate.

Nevertheless, we have to take a step back. Indeed, theses results are only preliminary results. There is still some work to do to optimize and make the set-up reliable. There are some optimizations at short term and some others at long term.

In the short term we can first think of the fabrication of a microchannel over a magnetoresistive sensor. In this system a tuned coil will be placed close to the sensor, which will serve as a reference. This way the inductive coupling between the tuned coil and the sensor will be absent. This approach, which was not discussed during this thesis, will enable to work with small sample volumes.

We also have to improve the sensitivity of the sensor deposited on glass and alumina while this one is placed into the magnetic field. For this some new innovative stacks should be tested.

On the long term some decisions should be taken concerning the field stability, which is now the major problem. To solve this, there are two possibilities. The first one is to optimize the electromagnet with feedback loop, which will compensate the current fluctuations. The other solution should be to use a supraconductive magnet. Each solution permits to overcome the retiming of the FFT and then have better resolution on the GMR channel.

Finally the use of an other type of magnetoresistive sensors should be investigate. Indeed, magnetic tunneling junctions offers a sensitivity 10 times better than our present sensors. And this leads to a time saving of 100 to have the same signal-to-noise ratio. But to use MTJ, we should be able to process them, which is presently not the case in the lab.

Bibliography

[1] F. Mott, "The Electrical Conductivity of Transition metal", Proc. R. Soc. London, vol. 153, pp. 699 - 717, (1935)

[2] M. N. Baibich, J. M. Broto, A. Fert, F. N. Van Dau, F. Petroff, P. Eitenne, G. Creuzet, A. Friederich, J. Chazelas, "Giant Magnetoresistance of (001)Fe/(001)Cr Magnetic Superlattices", Phys. Rev. Lett., vol. 61, pp. 2472 - 2475 (1988)

[3] M. Jullière, "Tunneling between ferromagnetic films", Phys. Lett. A, vol. 54, pp. 225 - 226 (1975)

[4] W.Thomson, "On the Electro-Dynamic Qualities of Metals: Effects of Magnetization on the Electric Conductivity of Nickel and of Iron" Proc. Royal Soc. London, vol. 8, pp. 546 - 550

[5] Th. G. S. M. Rijks , R. Coehoorn , J. T. F. Daemen , and W. J. M. de Jonge, "Interplay between exchange biasing and interlayer exchange coupling in Ni80Fe20/Cu/Ni80Fe20/Fe50Mn50 layered systems", Journal of Applied Physics 76 , 1092 (1994)

[6] W. P. Pratt Jr. , S.F. Lee , Q. Yang , P. Holody , R. Loloee , P. A. Schroeder , and J. Bass, "Giant magnetoresistance with current perpendicular to the layer planes of Ag/Co and AgSn/Co multilayers", Journal of Applied Physics 73 , 5326 (1993)

[7] F. Bloch, W.W. Hansen, and M. Packard, "The Nuclear Induction Experiment," Phys. Rev. 70, 474 (1946).

[8] E. Hahn, "Spin echoes", Phys. Rev. 80, 580 (1950)

[9] G. Binasch; P. Grünberg; F. Saurenbach; W. Zinn . "Enhanced magnetoresistance in layered magnetic structures with anti-ferromagnetic interlayer exchange" Phys. Rev. B 39 (7): 4828–4830 (1989)

[10] J.B. Johson, Nature 119, 50, 1927; Phys. Rev. 32, 97–109 (1928)

[11] H. Nyquist, "Thermal Agitation of Electric Charge in Conductors", Phys. Rev., vol. 32, pp. 110 (1928)

[12] F. Hooge, "1/f noise", Physica B+C, vol. 83, no. 1, pp. 14 – 23 (1976)

[13] D. I. Hoult, R. E. Richard, "The signal-to-noise ratio of the nuclear magnetic resonance experiment," J. Magn. Reson. , vol. 24, pp. 71–85 (1976)

[14] T. L. Peck, R. L. Magin, P. C. Lauterbur, "Design and analysis of microcoils for NMR spectroscopy", J. Magn. Reson. , vol. 108B, pp. 114 - 124 (1995)

[15] C. N. Chen, D. I. Hoult, "Biomedical magnetic resonance technology", Medical science series (1989)

[16] X. Zhang, A.G. Webb, "Magnetic Resonance Microimaging and Numerical Simulations of Velocity Fields Inside Enlarged Flow Cells Used for Coupled NMR Microseparations", Anal. Chem., vol. 77, pp. 1338-1344 (2005)

[17] K.Kratt, V.Badilita, T. Burger, J. G. Korvink, U. Wallrabe, "A fully MEMS-compatible process for 3D high aspect ratio micro coils obtained with an automatic wire bonder", J. micromech. Microeng., vol.20 (2001)

[18] J.A.Roges,R.J. Jackman, G.M. Whitesides,D.L. Olson, J.D. Sweedler, "Using microcontact printing to fabricate microcoils on capillaries for high resolution proton nuclear magnetic resonance on nanoliter volume", Appl. Phys. Lett., vol. 70, pp. 2464-2466 (1997)

[19] J. Y. Park, J.U. Bu, "Surface Micromachined RF Inductors and Transformers for Advanced Telecommunication Applications", International Symposium on Microelectronics, pp. 744-748 (2002)

[20] M. Woytasik, J.P. Grandchamp, E. Dufour-Gergam, J-P. Gilles, S. Megherbu, E. Martincic, H. Matias, P. Crozat, "Two- and three-dimensional microcoil fabrication process for three-axis magnetic sensors on flexible substrates", Sensor. Actuat. A-Phys., vol. 132, pp. 2-7 (2006)

[21] L.O. Sillerud, A.F. McDowell, N.L. Adolphi, R.E. Serda, D.P. Adams, M.J. Vasile, T.M. Alam, "1 H NMR Detection of superparamagnetic nanoparticles at 1 T using a microcoil and novel tuning circuit", J. Magn. Reson., Vol. 181, pp. 181-190 (2006)

[22] M. Gel, S. Takeuchi, I. Shimoyama, "Fabrication method for out-of-plane, microcoil by surface micromachining", Sensor. Actuat., pp. 702-708 (2002)

[23] J. Zou, C. Liu, D. Trainor, J. Chen, J. Schutt-Ainé, P. Chapman, "Development of Three-Dimensional Inductors Using Plastic Deformation Magnetic Assembly (PDMA)", IEEE Transactions on Microwave Theory and Techniques, pp. 1067-1075 (2003)

[24] C. Chua, D. F ork, K. Van Schuylenberg, J.-P. Lu, "Out-of-Plane High- Q Inductors on Low-Resistance Silicon", Journal of Microelectromechanical Systems, pp. 989-995 (2003)

[25] J.E. Stocker, T.L. Peck, A.G. Webb, M. Feng, R.L. Magin, "Nanoliter volume, high-resolution NMR microspectroscopy using a 60-micron planar microcoil", IEEE T. Bio-Med. Eng., pp. 1122-1127 (1997)

[26] C. Massin, G. Boero, F. Vincent, J. Abenhaim, P.-A. Besse, R.S. Popovic, "High-Q factor RF planar microcoils for micro-scale NMR spectroscopy", Sensor. Actuat. A-Phys., vol. 97, pp. 280-288 (2002)

[27] K. Ehrmann, N. Saillen, F. Vincent, M. Stettler, M. Jordan, F. M. Wurm, P.-A. Besse, R.S. Popovic, "Microfabricated solenoids and Helmholtz coils for NMR spectroscopy of mammalian cells", Lab Chip, vol 7, pp. 373-380 (2005)

[28] L. Renaud, M. Armenean, L. Berry, P. Kleimann, P. Morin, M. Pitaval, J. O'Brien, M. Brunet, H. Saint-Jalmes, "Implantable planar RF microcoils for NMR microspectroscopy", Sensor. Actuat. A-Phys., vol. 99, pp.2464-2466 (2002)

[29] R. W. Wood, Philos. Mag. 44, 1109 (1922).

[30] W. Happer, "Optical pumping", Rev. Mod. Phys., vol 44, pp. 169 - 238 (1972)

[31] F. Bitter, "The oytical Detection of Radiofxetluency Resonance", Phys. Rev., vol 76, pp. 833 - 835 (1949)

[32] J. C. Allred, R. N. Lyman, T. W. Kornack, M. V. Romalis, "High-Sensitivity Atomic Magnetometer Unaffected by Spin-Exchange Relaxation", Phys. Rev. Lett., vol. 89 (2002)

[33] D. Peter, D. Schwindt, S. Knappe, V. Shah, L. Hollberg, J. Kitching, L. A. Liew, J. Morelan, "Chip-scale atomic magnetometer", Appl. Phys. Lett., vol. 85, pp. 6409 - 64011 (2004)

[34] M. P. Ledbetter, I. M. Savukov, D. Budker,V. Shah, S. Knappe, J. Kitching, D. J. Michalak, S. Xu, A. Pines, "Zero-field remote detection of NMR with a microfabricated atomic magnetometer", PNAS, vol. 105, pp. 2286 - 2290 (2008)

[35] I. M. Savukov, S. J. Seltzer, M. V. Romalis, K. L. Sauer, "Tunable Atomic Magnetometer for Detection of Radio-Frequency Magnetic Fields", Phys. Rev. Lett., vol. 95 (2005)

[36] I. M. Savukov, S. J. Seltzer, M. V. Romalis, "Detection of NMR signals with a radio-frequency atomic magnetometer", J. Magn. Reson., Vol. 185, pp. 214 - 220 (2007)

[37] P. Neumann, R. Kolesov, V. Jacques, J. Beck, J. Tisler, A. Batalov, L. Rogers, N. Manson, G. Balasubramanian, F. Jelezko, J. Wrachtrup, "Excited-state spectroscopy of single NV defects in diamond using optically detected magnetic resonance", New. J. Phys., vol. 11 (2009).

[38] T. Staudacher, F. Shi, S. Pezzagna, J. Meijer, J. Du, C. A. Meriles, F. Reinhard, J. Wrachtrup, "Nuclear Magnetic Resonance Spectroscopy on a $(5-Nanometer)^3$ Sample Volume", Science, vol. 339, pp. 561 - 563 (2013)

[39] S. Kotler, N. Akerman, Y. Glickman, A. Keselman, R. Ozeri, "Single-ion quantum lock-in amplifier", Nature, vol. 473, pp. 61 - 65 (2011)

[40] E. Stoner, E. Wohlfarth, "A Mechanism of Magnetic Hysteresis in Heterogenous Alloys", Phil. Trans. Roy. Soc., pp. 599 – 642 (1948)

[41] M. Pannetier,C. Fermon, G. Le Goff, J. Simola, E. Kerr, J. Coey, "Noise in small magnetic systems - Applications to very sensitive magnetoresistive sensors", J. Magn. Reson., Vol. 290, pp. 1158 - 1160 (2005)

[42] F. Romeo, D. Hoult, "Magnet field profiling: analysis and correcting coil design", Mag. Res. Med., vol. 1, pp. 44 – 65 (1984)

[43] D. Hoult, "The NMR Receiver: a descrption and analsis of design", Progress in NMR Specrroscopv, vol. 12, pp. 41 - 77 (1978)

[44] W.P. Pratt, S. F. Lee, J.M. Slaughter, R. Loloee, P. A. Schroeder, J. Bass, "Perpendicular Giant Magnetoresistances of Ag/Co Multilayers", Phys. Rev. Lett., vol. 66, pp. 3060 - 3063 (1991)

[45] M. Jullière, "Tunneling between ferromagnetic films" Phys. Lett. A., vol 54 (1975)

[46] S. P. Parkin, C. Kaiser, A. Panchula, P. M. Rice, B. Hughes, M. Samant, S. Yang, "Giant tunnelling magnetoresistance at room temperature with MgO (100) tunnel barriers", Nat. Mat., vol. 3, pp. 862 - 867 (2004)

[47] A. Overhauser, "Polarization of nuclei in metals". Phys. Rev., vol. 92, pp. 411 – 415 (1953)

[48] R. W. Adams, J. A. Aguilar, K. D. Atkinson, M. J. Cowley, P. I. P. Elliott, S. B. Duckett, G. G. R. Green, I. G. Khazal, J. Lopez-Serrano, D. C. Williamson, "Reversible Interactions with para-Hydrogen Enhance NMR Sensitivity by Polarization Transfer", Science, vol. 323, pp. 1708 (2009)

[49] S. C. Grant, D. L. Buckley, S. Gibbs, A. G. Webb, S. J. Blackband, "MR Microscopy of Multicomponent Diffusion in Single Neurons" Magn. Reson. Med., vol.44, pp. 19 (2001)

[50] I. Rabi, J.R Zacharias, S. Millman, P. Kusch, "A New Method of Measuring Nuclear Magnetic Moment", Physical Review, vol. 53, pp. 318 – 327 (1938)

[51] R. Wimberger-Friedl, T. Nellissen, W. Weekamp, J. Van Delft, W. Ansems, M. Prins, M. Megens, W. Dittmer, C. De Witz, B. Van Iersel, "Packaging of silicon sensors for microfluidic bio-analytical applications", J. Micromech. Microeng., vol. 19 (2009)

[52] S. Gangopadhyay, J. X. Shen, M. T. Kief, J. A. Barnard, M. R. Parked, "Giant Magnetoresistance in CoFe/Cu multilayers with different buffer and substrates", IEEE Trans. on Magn., vol. 31, pp. 3933 - 3935 (1995)

[53] A. Chalastaras, L. M. Malkinski, J. S. Jung, S. L. Oh, J. K. Lee, C. A. Ventrice, V. Golub, G. Taylor, "GMR Multilayers on a New Embossed Surface", IEEE Trans. on Magn., vol. 40, pp. 2257 - 2259 (2004)

[54] T. Uhrmann, L. Bär, T. Dimopoulos, N. Wiese,M. Rührig, A. Lechner, "Magnetostrictive GMR sensor on flexible polyimide substrates", J. of Magnetism. and Magnetic Materials, vol. 37, pp. 209 - 211 (2006)

[55] J. Jeener, J. Ampere, International Summer School, Basko Polje, Yugoslavia (1971)

[56] W. G. Proctor, F. C. Yu, "The Dependence of a Nuclear Magnetic Resonance Frequency upon Chemical Compound", Phys. Rev., vol. 77, pp. 716 (1950)

[57] W.C. Dickinson, "Dependence of the F^{19} Nuclear Resonance Position on Chemical Compound", Phys. Rev., vol. 77, pp. 736 (1950)

[58] J. T. Arnold, S. S. Dharmatti, M. E. Packard, "Chemical Effects on Nuclear Induction Signals from Organic Compounds", J. Chem. Phys., vol. 19, pp. 507 (1951)

[59] A. C. Wright, H. K. Song, F. W. Wehrli, "In Vivo MR Micro Imaging With Conventional Radiofrequency Coils Cooled to 77°K", Mag. Res. Med., vol. 43, pp 163 – 169 (2000)

[60] J. M. Pope, D. Jonas, R. R. Walker, "Applications of NMR micro-imaging to the study of water, lipid, and carbohydrate distribution in grape berries", Protoplasma, vol. 173, pp 177 - 186 (1993)

[61] W. Köckenberger, "Nuclear magnetic resonance micro-imaging in the investigation of plant cell metabolism", Journal of experimental botany, vol. 52, pp. 641 - 652 (2001)

[62] F. Bensminaa, P. Humbert, A. Dinia, D. Muller, V.S. Speriosu, B.A. Gurney, "Annealing effect on the magnetic properties of Ta 50 Å/Cu 50 Å/Co 75 Å/Cu 50 Å/Ta 50 Å sandwiches", J. of Magnetism. and Magnetic Materials, vol. 198 – 199, pp. 338 - 340 (1999)

[63] H.R. Liu, B.J. Qu, T.L. Ren, L.T. Liu, H.L. Xie, C.X. Li, W.J. Ku, "High-sensitivity GMR with low coercivity in top-IrMn spin-valves", J. of Magnetism. and Magnetic Materials,vol. 267, pp. 386 - 390 (2003)

[64] A. Abragam, "The Principles of Nuclear Magnetism", Oxford at the Clarendon Press (1961)

[65] J. C Ginefri, A. Rubin, M. Tatoulian, M. Woytasik, F. Boumezbeur, B. Djemaï, M. Poirier-Quinot, F. Lethimonnier, L. Darrasse, E. Dufour-Gergam, "Implanted, inductively-coupled, radiofrequency coils fabricated on flexible polymeric material: application to in vivo rat brain MRI at 7 T", J. of Magn. Res., vol. 224, pp. 61 - 70 (2012)

[66] J. Nogues, I.K. Schuller, "Exchange bias", J. Magn. Magn. Mater., vol. 192, pp. 203 - 225 (1999)

[67] A. McDowell, N. Adolphi, "Operating nanoliter scale NMR microcoils in a 1 teslafield", J. Mag. Res., vol. 188, pp. 74 - 82 (2007)

ÉCOLE DOCTORALE
Physique en Île-de-France (EDPIF)

Titre : Spectroscopie locale par résonance magnétique nucléaire à l'aide de capteur à magnétorésistance géante

Mots clés : Sonde locale, GMR, RMN, éthanol, Spectroscopie

Résumé :
La Spectroscopie par Résonance Magnétique Nucléaire (NMRS) est une technique largement connue pour l'analyse de molécules chimiques et biologiques. Cependant, en raison de la faible intensité des signaux de RMN, il est très difficile de travailler sur des volumes inférieurs à un mm^3. Cette limitation a conduit à la mise au point de capteurs miniaturisés tels que les microbobines, les centres NV et des magnétomètres atomiques.
Au cours de cette thèse nous avons développé une approche basée sur l'utilisation de capteurs à MagnétoRésistance Géante (capteurs GMR), capteurs magnétiques à large de la bande de fréquences, capable de détecter localement le signal RMN.
Les capteurs GMR réalisés sur différents substrats tels que le silicium, le verre et l'alumine, ainsi que la configuration du montage RMN ont été spécifiquement conçus pour d'une part, permettre une détectivité dans la gamme de $20pt/\sqrt{Hz}$ et d'autre part pouvoir supporter un champ magnétique externe jusqu'à 1 Tesla.
Je présenterai tout d'abord les résultats obtenus à 0.3T sur de l'eau, dans la configuration où la RMN locale est effectuée dans un grand volume (de l'ordre du un cm^3), afin de mettre en évidence le caractère fonctionnel du montage. Je présenterai ensuite les résultats obtenus sur des volumes bien plus faibles (de l'ordre de $20x20x20\mu m^3$) de liquides modèle pour la RMN, comme l'éthanol. Enfin je montrerai les premiers tests concluants effectués sur de l'eau en appliquant un champ magnétique externe de 0.6T.

Title : Local Nuclear Magnetic Resonance Spectroscopy with Giant Magnetoresistive Sensors

Keywords : Local probe, GMR, NMR, ethanol, Spectroscopy

Abstract:
Magnetic Resonance Spectroscopy (NMRS) is a widely known technique for chemical and biological molecule analysis. However due to the weakness of the NMR signals, it is very difficult to work on volumes lower than a mm^3. That limitation has led to the development of miniaturized sensors such as microcoils, NV centers and atomic magnetometers.
We will present our approach based on the use of Giant Magnetoresistive sensors (GMR) as wide band magnetic sensors to detect locally the NMR signal. GMR sensors and NMR set up have been specifically designed to have a detectivity in the range of 20pt/sqrt(Hz) and able to work with an external magnetic field up to 1T.
We will first present the results obtained at 0.3T on water, in the configuration where the local NMR is done on a high volume, highlighting the functionality of the set-up. Then we will show the results obtained also at 0.3T, of NMR spectroscopy of model liquids like Ethanol on a volume of the order of $20x20x20\mu m^3$. Finally, a result at a higher magnetic field, 0.6T, has also been obtained on water.

Université Paris-Saclay
Espace Technologique / Immeuble Discovery
Route de l'Orme aux Merisiers RD 128 / 91190 Saint-Aubin, France